Muon Studies of Unconventional Superconductors

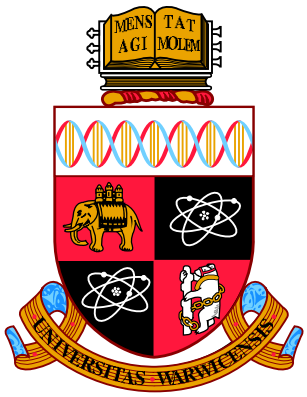

Joel Alexander Thomas Barker

Department of Physics
University of Warwick

This dissertation is submitted for the degree of
Doctor of Philosophy

April 2017

Table of contents

List of figures

List of tables

Acknowledgements

Special thanks are due to my supervisors Don Paul and Adrian Hillier, for their support, patience, and guidance throughout the course of this work. Aidy, thank you for teaching me to be a responsible scientist - working so closely with you at ISIS was one of the highlights of my Ph.D. Don, running experiments with you was always a pleasure, and one that I hope to repeat in the future.

I would also like to thank the other members of the Superconductivity and Magnetism group, in particular Martin Lees for his assistance in learning to use the characterization facilities, and also for his unwavering attention to detail; Oleg Petrenko for helping me learn the Laue system and for developing a healthy fear of photographic film; Tom Orton for his expertise and patience in the face of magnet quenches at 10.5 T; and Geetha Balakrishnan for her guidance in the face of all things crystal growth related. Special thanks are also due to Ravi Singh for his training and guidance at the start of my Ph.D, and who continues to be a source of inspiration and advice; Dean Keeble and David Walker for assistance with X-ray diffraction and the TOPAS software; and the countless other academics at Warwick who have helped me throughout my time there. I would also like to extend my thanks to the scientists at ISIS and the ILL who I have had the pleasure of working with and being taught by over the past four years.

This thesis would not have been possible without the love and support of Niina. I'd also like to thank my fellow students; in particular Mohammed Saghir and Robert Cook, who welcomed me graciously into P220 (the best office), Natalia Parzyk, and Michael Smidman. Special thanks go to Charlie Young, for his special brand of guidance and advice which convinced me to pursue a life in Physics all those years ago. Finally, I am also grateful to the members of my family who have offered their support and encouragement throughout my academic life. I couldn't have done it without you guys.

Declaration

This thesis is submitted to the University of Warwick in support of my application for the degree of Doctor of Philosophy. It has been composed by myself and has not been submitted in any previous application for any degree.

The polycrystalline samples of La_7Ir_3, Re_3Ta, $LuRuB_2$, and $YRuB_2$ were prepared by Dr. Ravi Singh during his time at Warwick. The single crystal of $Lu_3Os_4Ge_{13}$ was provided by Dr. Ravi Singh from his current position at IISER Bhophal.

Physical properties measurements were performed by myself under the supervision and guidance of Dr. Martin Lees. Muon spin rotation and relaxation experiments were carried out at the ISIS facility near Didcot, Oxfordshire, UK, with the assistant of intrument scientists. For all the experiments I was the leading member of the experimental team, and performed all of the data analysis under the guidance of my supervisors, Prof. Don Paul and Dr. Adrian Hillier.

No part of this thesis has been submitted for examination at any other institution. Parts of the work described in this thesis have been published in the following article:

- 'Unconventional Superconductivity in La_7Ir_3 Revealed by Muon Spin Relaxation: Introducing a New Family of Noncentrosymmetric Superconductor That Breaks Time-Reversal Symmetry', J. A. T. Barker, D. Singh, A. Thamizhavel, A. D. Hillier, M. R. Lees, G. Balakrishnan, D. McK. Paul, and R. P. Singh, *Physical Review Letters*, **115**, 267001 (2015)

Joel Alexander Thomas Barker
April 2017

Abstract

This thesis presents muon spin rotation and relaxation (μSR) studies of various superconducting materials. μSR studies have been complemented with laboratory measurements of heat capacity, resistivity, and magnetization. This work contributes to the body of work surrounding noncentrosymmetric superconductors (NCS) and unconventional superconductivity.

The intermetallic compound La_7Ir_3 is found to break time-reversal symmetry upon transitioning into the superconducting state, elucidated by muon spin relaxation. The pairing symmetry appears fully gapped, and is well described by an isotropic *s*-wave model. Further theoretical analysis of the point group symmetry could investigate the allowed superconducting states potentially existing here.

The physical properties of the NCS Re_3Ta are well described by the conventional BCS theory of superconductivity. μSR suggests unusual narrowing of the vortex lattice signal in a region close to T_c, interpreted as motional narrowing due to thermal motion of vortices. This is supported by irreversible magnetization in a sizable region in the phase diagram. Ginzburg number and quantum resistance calculations place Re_3Ta intermediate between the high-T_c and conventional low-T_c superconductors.

$LuRuB_2$ and $YRuB_2$, superconducting members of the ternary boride family of materials, are studied using μSR. Zero-field measurements detect spin fluctuations exhibiting critical slowing down as the temperature is lowered, suggesting that these materials lie near a quantum phase transition. These weak fluctuations coexist with the superconductivity, which is well described by an isotropic, *s*-wave model for the pairing symmetry.

The semi-metal $Lu_3Os_4Ge_{13}$ is investigated using transverse-field and zero-field μSR. The superfluid density is well described by a model containing two superconducting gaps, supporting previously reported heat capacity measurements. Zero-field measurements below T_c reveal a signal hinting at broken time-reversal symmetry, however, it does not coincide with the bulk superconducting transition. Further theoretical work could determine whether this is the first observation of a novel three-gap multiband superconducting ground state.

Chapter 1

Preface

Since its discovery in 1911, understanding the underlying Physics of superconductivity has been a major goal of condensed matter research [1]. The microscopic theory of Bardeen, Cooper, and Schrieffer (BCS), remains to this day a triumph of theoretical Physics [2]. However, there exist an alarming number of superconductors that are not well described by the conventional theory [3]. Condensed matter research has aimed to undercover the Physics of these 'unconventional' superconductors for some time, but despite ardent experimental and theoretical efforts, it still remains far from a solved problem. As an example of this, consider that the nature of the pairing mechanism in the high-temperature cuprate superconductors is still not fully understood, more than 25 years after their discovery [4]. An unconventional superconductor is defined as one in which the pairing symmetry of the superconducting electrons is different from that expected in the conventional BCS theory of superconductivity.

In this thesis, the technique of muon spin rotation and relaxation (μSR) lies at the core of the experimental data in every chapter. μSR is a powerful probe of local magnetism, and can be applied to a diverse array of different fields. The basis of the technique relies on our ability to implant 100% spin polarized muons into matter, and then to be able to observe the subsequent time evolution of the ensemble polarization. Recently, muons have been used to study Li diffusion in battery materials [5]; spin-liquid states in a quantum Kagome antiferromagnet [6]; magnetic properties of double perovskites [7]; and harnessed as a novel method of performing depth-sensitive composition analysis [8]. The μSR technique has also been applied extensively to studies of the vortex lattice in type-II superconductors. The crossover from a triangle to a square lattice has been observed in the candidate chiral p-wave superconductor Sr_2RuO_4 [9], and the technique is sensitive enough to measure vortex clustering at low temperatures. One field in which μSR excels

is the detection of time-reversal symmetry breaking, which is associated with the formation of superconducting states that feature triplet pairs of electrons [10–12]. The following provides an overview of the compounds studied in each experimental chapter using this technique.

1.1 Thesis overview

Chapter 2, Theoretical overview: A general background to the theory of superconductivity is presented, including details from the microscopic theory and the phenomenological Ginzburg-Landau theory. Results applicable to experimental data analysis are emphasized.

Chapter 3, Experimental techniques: The wide variety of experimental equipment that has been used to characterize the samples in this thesis is introduced, with pertinent results applicable to the analysis and interpretation of the raw data described. This chapter also describes the technique of muon spin spectroscopy in detail.

Chapter 4, Time-reversal symmetry breaking in La_7Ir_3: The first experimental chapter investigates the superconductivity in this noncentrosymmetric intermetallic compound, which appears to exhibit broken time reversal symmetry, and may therefore have an unconventional superconducting ground-state.

Chapter 5, Probing the noncentrosymmetric superconductor Re_3Ta: This alloy crystallizes in a noncentrosymmetric space group, and exhibits a high amount of disorder in its structure. This material appears to have a conventional superconducting ground state, however μSR observations suggest novel vortex dynamics, which are unusual for such low temperature superconductors.

Chapter 6, Superconductivity in $LuRuB_2$ and $YRuB_2$: The boride family of superconductors have provided a rich variety of interesting Physics, particularly in the fields of magnetism and superconductivity. This chapter presents a muon study of a pair of intermetallic ternary boride materials, and investigates the effect of 4f electrons on the superconductivity.

Chapter 7, Multiband superconductivity in $Lu_3Os_4Ge_{13}$: This material has been found to have an extraordinarily low carrier density, and laboratory measurements suggest that it has multiple superconducting gaps. Muon measurements are made in an attempt to better understand the superconductivity in this material.

Chapter 8, Summary and conclusions: A summary of the key findings, challenges, as well as suggestions for future research are presented.

Chapter 2

Theoretical Background

This section presents an overview of the main features of the theory of superconductivity, which form a key component of the analysis techniques used in this thesis. Necessary results from the phenomenological Ginzburg-Landau theory, and the microscopic theory of Bardeen, Cooper, and Schrieffer, are presented, and some calculations of the field distribution due to the vortex lattice are outlined. Throughout this section I make repeated use of information and equations detailed in Refs. [13–15].

2.1 Elementary superconductivity

A material is considered to be a superconductor if it exhibits the two distinctive experimental observations of 1) perfect conductivity, and 2) no magnetic induction, manifesting below a certain critical temperature, T_c. The first observation tells us that

$$\rho = 0 \quad \forall\, T < T_c, \tag{2.1}$$

where ρ is the electrical resistivity. The most convincing evidence for this comes from measurements of persistent currents in superconducting rings, as depicted in Fig. 2.1. Upon cooling such a ring below T_c under an applied magnetic field, supercurrents are induced, ensuring that the total flux enclosed by the ring is quantized in units of the magnetic flux quantum:

$$\Phi_0 = \frac{h}{2e} \approx 2.068 \times 10^{-15}\text{Wb}. \tag{2.2}$$

Because the resistivity is exactly zero, supercurrent continues to flow upon removal of the external magnetic field, such that the total flux trapped within the ring remains

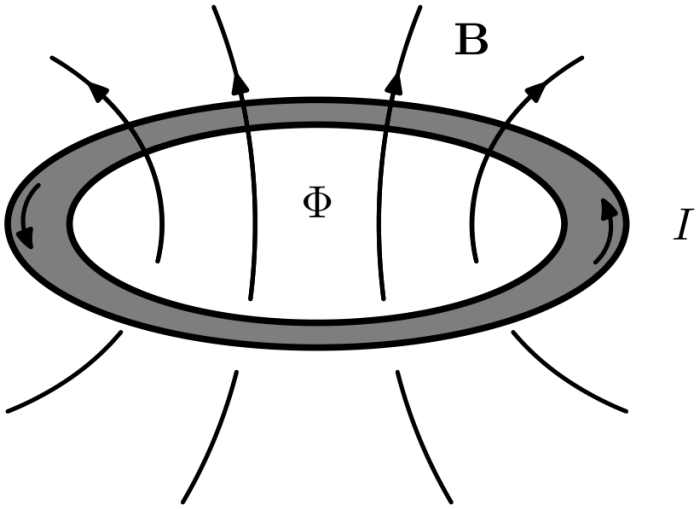

Fig. 2.1 Persistent current around a superconducting ring. The current maintains a constant magnetic flux, Φ, through the superconducting ring. Figure from Ref. [13].

constant. Experiments measuring the subsequent time evolution of the trapped field have found upper bounds on the lifetime of the supercurrent in excess of 100 000 years, supporting the view that the electrical resistance of a superconductor is exactly zero [16].[1]

Diamagnetism is the tendency of most materials to weakly oppose an applied magnetic field. A superconductor can be thought of as a perfect diamagnet, in that it completely expels an applied magnetic field from within its interior, such that the magnetic induction $\vec{B} = 0$ everywhere. From electrodynamics, we know that the magnetic induction is related to the applied field, $\vec{H}$, and the magnetization, $\vec{M}$, by the equation

$$\vec{B} = \mu_0(\vec{M} + \vec{H}),$$

where μ_0 is the permeability of free space. This implies that

$$\vec{M} = -\vec{H}, \tag{2.3}$$

within the superconductor, i.e. the superconductor acquires a magnetization of the direction and magnitude required to exactly cancel out any applied magnetic field. The magnetization is induced by the formation of swirling supercurrents on the

[1] Strictly speaking this is only true for a type-I material - in type-II superconductors, interactions between vortices and the crystal structure can lead to a dissipation of energy in the mixed state.

surface of the superconductor. This expulsion of magnetic flux is the *Meissner effect* [17], and is considered to be the true hallmark of superconductivity.

One of the first attempts at explaining the Meissner effect was the London theory, proposed in 1935, which considered the electrodynamics of a perfect conductor [18]. The main postulate of the model is that some fraction of the conduction electron number density, n, becomes superconducting at T_c, forming a superfluid with a density n_s. The supercurrent, $\vec{J}_s$ is related to the magnetic vector potential, $\vec{A}$, by the equation

$$\vec{J}_s(\vec{r}) = -\frac{1}{\mu_0 \lambda_L^2}\vec{A}(\vec{r}), \tag{2.4}$$

where the parameter

$$\lambda_L^2 = \frac{m_e}{\mu_0 n_s e^2} \tag{2.5}$$

is the *London penetration depth*. Equation (2.4) replaces Ohm's law for a superconductor, which is ill-defined in the case of perfect conductivity. The physical interpretation of λ_L is made clear by substituting Eq. (2.5) into Ampere's Law for the supercurrent, which yields

$$\vec{\nabla}^2\vec{B} = \frac{1}{\lambda_L^2}\vec{B}. \tag{2.6}$$

The solution of this equation in the case of a constant magnetic field applied to a superconducting slab is an exponential decay (see Fig. 2.2). The magnetic induction is screened within a length λ_L from the surface, approaching $\vec{B} = 0$ deep in the interior of the superconductor. Thus the Meissner effect emerges naturally from this theory. Higher superfluid densities, n_s, lead to more effective screening of the magnetic field, and therefore give rise to a smaller London penetration depth.

Even though superconductivity was discovered as early as 1911, it took some four and a half decades to construct a satisfactory microscopic description. The 1957 theory of superconductivity presented by Bardeen, Cooper, and Schrieffer (hereafter denoted BCS theory) remains the framework for modern microscopic theories [2]. The absence of resistivity below T_c arises as a result of the condensation of free electrons into a coherent state formed of bound electron pairs. Zero resistivity emerges as a consequence of this pairing, which can be elucidated by considering scattering in a normal metal. Scattering centres exist on the crystal lattice, where a typical length scale is of the order 10^{-10} m. In a metal, electron velocities are given by the Fermi velocity, v_F, which is typically of order $10^6\ \mathrm{m\,s^{-1}}$. Using De Broglie's

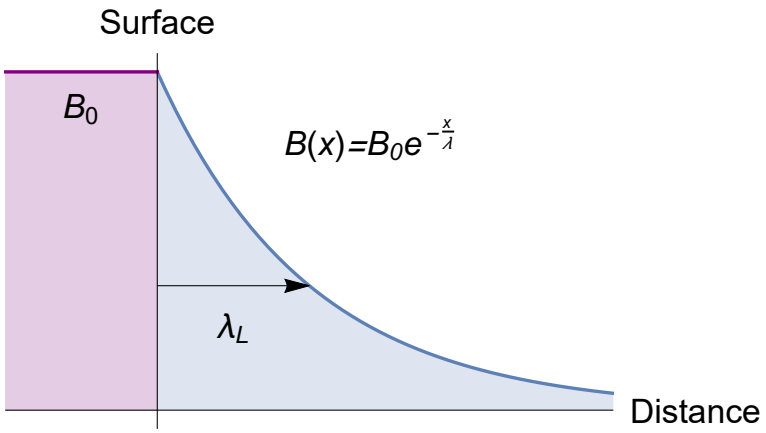

Fig. 2.2 The London description of the Meissner effect. The applied field $\vec{B}_0$ is screened out by surface currents over a characteristic length λ_{L}.

relation for an electron of momentum $p = m_{\mathrm{e}} v_{\mathrm{F}}$, we find

$$\lambda = \frac{h}{p} \approx 10^{-10}\ \mathrm{m},$$

which is the same length scale over which scatterers are distributed. Therefore, we expect a scattering interaction, which manifests as the phenomenon of resistance.

Under the conventional BCS theory, Cooper pairs are required to have zero total momentum. The electrons form a spin singlet, and possess equal and opposite linear momentum. Inserting $p = 0$ into the De Broglie relation results in a divergence of the wavelength. This is clearly unphysical, however it does hint at an important property of the superconducting state: the wavefunction of a superconductor is macroscopic, and describes all of the Cooper pairs as a coherent ensemble. Evidently, the De Broglie wavelength of a Cooper pair is orders of magnitude larger than the scattering centres in the metal. The coherent state of Cooper pairs is thus entirely unaffected by the scattering centres, allowing unimpeded current flow, and the observed electrical resistivity is zero as a result.

2.2 Ginzburg-Landau theory

The expulsion of magnetic flux from an ideal superconductor is independent of whether the magnetic field is applied above or below T_{c}.[2] This independence on the path chosen through the magnetic phase diagram indicates that superconductivity is

[2]Note that this is only strictly true if pinning effects are negligibly small. In real superconductors, particularly type-II materials, inhomogeneities and impurities in the sample can lead to pinning centres, which trap magnetic flux and lead to hysteretic behaviour.

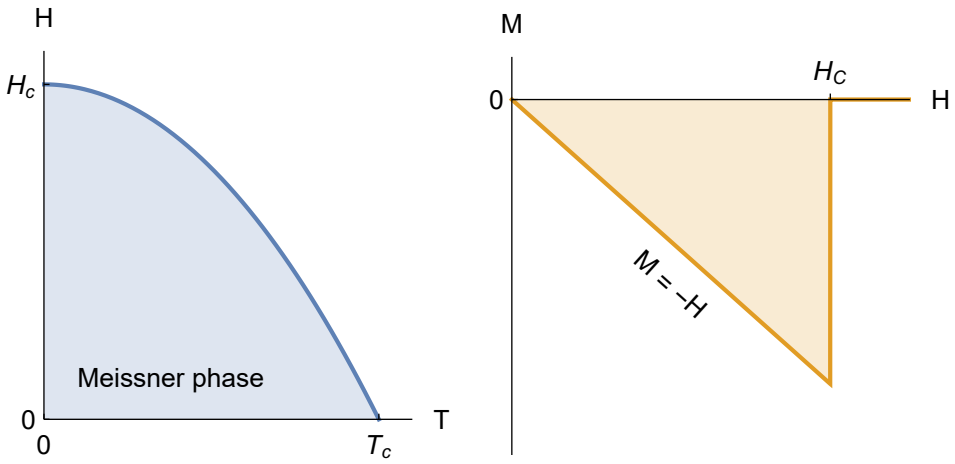

Fig. 2.3 The first column presents the H-T phase diagram for a type-I superconductor. The second column shows the associated dependence of the magnetization on the applied field. The total area under this curve is the condensation energy.

a thermodynamic state of matter, and as such can be described using the language of thermodynamic potentials. Working with the Gibbs free energy, $G(T,\vec{H})$, it can be shown that the difference between the free energies of the superconducting and normal states in zero field is

$$G_{\mathrm{s}}(T,0) - G_{\mathrm{n}}(T,0) = -\mu_0 \frac{H_{\mathrm{c}}^2}{2}, \tag{2.7}$$

which defines the *condensation energy* of the superconductor. It is a measure of the amount by which the total energy is lowered by transitioning to the superconducting state. The quantity H_{c} defines the *thermodynamic critical field*, and is the maximum strength of an applied field for which superconductivity remains energetically favourable. Note that baked into this interpretation is the assumption that Eq. (2.3) remains valid everywhere inside the superconductor. If this is the case, then we have a *type-I* superconductor. Most of the elemental pure metal superconductors are type-I, with Vanadium and Niobium being notable exceptions. The magnetic phase diagram of a type-I material is presented in Fig. 2.3, together with the expected dependence of the magnetization on the applied field.

Most superconductors that have been discovered are in fact able to maintain superconductivity in much higher magnetic fields. In this case we have a *type-II* superconductor, where above a certain threshold field, H_{c1}, the superconductor allows magnetic flux to partially penetrate its interior. This allows the superconductivity

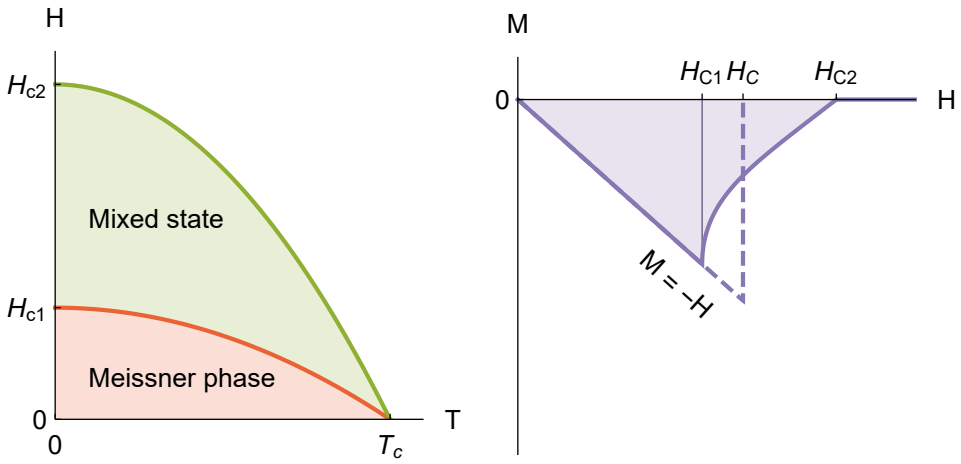

Fig. 2.4 The first column presents the H-T phase diagram for a type-II superconductor. The second column shows the associated dependence of the magnetization on the applied field. As before, the total area under the curve is the condensation energy.

to persist up to a much higher applied magnetic field strength, H_{c2}. Above H_{c2} the material returns to the normal state, and below H_{c1} the superconductor is fully in the Meissner state. The magnetic phase diagram is depicted in Fig. 2.4, where the region in which $H_{c1} < H < H_{c2}$ is called the *mixed state*. Intuitively, H_{c1} and H_{c2} are named the lower and upper critical fields, respectively. The thermodynamic critical field, H_c also exists for type-II superconductors, however, they do not exhibit any phase transition at this point. Rather, H_c provides a useful measure of the condensation energy.

In 1950, Ginzburg and Landau (henceforth referred to as GL) introduced their phenomenological theory of superconductivity [19, 20]. Whilst it was initially viewed with some scepticism, it can in fact be derived from the microscopic BCS theory in the appropriate limit [21]. GL theory has proven to be very powerful in describing the properties of unconventional superconductors, such as the high-T_c oxides, as well as superconductors in the dirty limit. The GL theory builds upon Landau's theory of second order phase transitions in magnetic materials, postulating the existence of a complex order parameter which governs the superconductivity:

$$\psi(\vec{r}) = |\psi(\vec{r})|e^{i\phi(\vec{r})}. \tag{2.8}$$

ψ is assumed to vanish above T_c, and spontaneously choose a non-zero value below T_c, in direct analogy to the magnetization in a magnetic material. The modulus of

the superconductor is directly proportional to the superfluid density, n_s, and the supercurrent is related to the gradient of the phase, $\vec{\nabla}\phi$, throughout the superconductor.

In the GL theory, it is postulated that the free energy density, f can be written in the form

$$f_s = f_n + \alpha|\psi|^2 + \frac{\beta}{2}|\psi|^4 + \frac{\hbar}{2m}(\vec{\nabla}\psi)^2 + \frac{1}{2}|\psi|^2 m\vec{v}_s^2 + \frac{\mu_0\vec{H}^2}{2}, \tag{2.9}$$

where $\vec{v}_s$ is the *superfluid velocity*, and is given by

$$\vec{v}_s = \frac{1}{m}(\hbar\vec{\nabla}\phi - 2e\vec{A}). \tag{2.10}$$

Here, $\vec{A}$ is the magnetic vector potential, which is related to the magnetic field $\vec{H}$ by the equation $\mu_0\vec{H} = \vec{\nabla}\times\vec{A}$. The parameters α and β must be determined experimentally, where the temperature dependence of α is assumed to follow $\alpha = a(T - T_c)$, as in the Landau theory. Evidently, if $\psi = 0$ then the only terms that survive are the free energy density of the normal state, f_n, and the energy density of the magnetic field, $\frac{\mu_0\vec{H}^2}{2}$. The superconducting properties are determined by minimising the free energy density with respect to changes in $\psi(\vec{r})$ and $A(\vec{r})$.

Two characteristic length scales emerge as a result of the GL theory. The first is the Ginzburg-landau coherence length, $\xi(T)$, which can be interpreted as the distance over which changes in ψ may occur. In general, this depends on the electrical mean free path, l_e, and the temperature independent BCS coherence length, defined by Eq. (2.30). The second is an effective penetration depth, $\lambda(T)$, which is proportional to the London penetration depth λ_L. Both of these quantities diverge as $T \to T_c$, however their ratio

$$\kappa = \frac{\lambda(T)}{\xi(T)} \tag{2.11}$$

is expected to be approximately temperature independent. Equation (2.11) specifies the *Ginzburg-Landau parameter*, which fully defines the properties of a superconductor in the GL theory.

Experimentally, one may determine ξ and λ by performing measurements of the critical fields. The upper critical field yields ξ directly by the equation

$$\mu_0 H_{c2} = \frac{\Phi_0}{2\pi\xi^2(T)}. \tag{2.12}$$

H_{c2} is readily measured via magnetization, resistivity, or heat capacity experiments in the laboratory. Section 2.6 provides more detail on measurements of the upper

critical field, and details the mechanisms by which magnetic field acts to destroy superconductivity. The lower critical field is related to the effective penetration depth by the equation

$$\mu_0 H_{c1} = \frac{\Phi_0}{4\pi\lambda^2(T)} \ln \kappa. \tag{2.13}$$

Measurements of H_{c1} are usually carried out by studying the low-induction magnetization behaviour of the superconductor. However, this relies on accurately determining the point at which flux first begins to penetrate the sample, which is difficult to determine accurately using this technique. It is better to directly measure λ using methods such as muon spin rotation in order to calculate the lower critical field (see Sec. 3.6 for details). The relationship between the two characteristic length scales and the thermodynamic critical field is given by the GL theory as

$$\mu_0 H_c = \frac{\Phi_0}{2\sqrt{2}\pi\lambda\xi}. \tag{2.14}$$

Combining Eqs. (2.12) and (2.14), one finds that the H_{c2} is related to H_c by

$$H_{c2} = \kappa\sqrt{2} H_c. \tag{2.15}$$

Clearly if $\kappa < 1/\sqrt{2}$, then $H_{c2} < H_c$. In this case, no superconductivity exists above the thermodynamic critical field, and below H_c the superconductor exhibits perfect flux expulsion. Therefore we have a *type-I superconductor*. However, if $\kappa > 1/\sqrt{2}$, then $H_{c2} > H_c$. Here, superconductivity exists above the thermodynamic critical field. This is achieved by transitioning into the mixed state, where partial penetration of magnetic flux occurs. This describes a *type-II superconductor*. The GL parameter thus allows us to classify superconductors as type-I or type-II, dependant only on the value of κ.

2.2.1 Properties of the mixed state

The nature of the mixed state was determined by Abrikosov in 1957 [22]. The key insight came through calculating the surface energy of interfaces between the normal and superconducting states in type-I and type-II superconductors. When κ is larger than $1/\sqrt{2}$, the surface energy changes from positive to negative. This means that it becomes energetically favourable to nucleate as many normal-superconducting interfaces as possible. In the regions of the material which become normal, the magnetic field is allowed to penetrate, which is why we say that the superconductor allows *partial penetration* of magnetic flux in the mixed state. However, the spatial

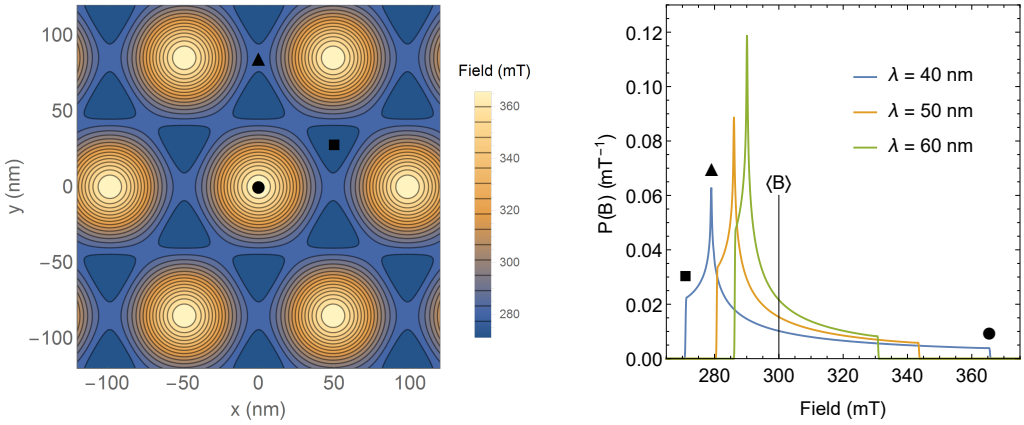

Fig. 2.5 Simulations of the vortex lattice performed using the London model with a Gaussian cut-off, described in Ref. [23]. A contour plot of the magnetic field profile of the ideal vortex lattice is presented in (a), with the associated histograms, $P(B)$, for a few different values of λ displayed in (b). The marked points ▲, ●, and ■ correspond to the peak field, maximum field, and minimum field, respectively. Simulation parameters: $\langle B \rangle = 300\,\mathrm{mT}$, $\xi = 20\,\mathrm{nm}$.

extent of the normal region is limited by the coherence length, as the superconducting wavefunction may not change significantly over distances smaller than ξ. Therefore, the area of the normal region is proportional to ξ^2. Furthermore, the normal region must be surrounded by a loop of supercurrent, such that the superconducting region is screened from the magnetic field contained within. The periodic boundary conditions on a ring of supercurrent require that the magnetic flux contained within the loop is an integer number of magnetic flux quanta, Φ_0. In the mixed state, the free energy is minimised when exactly one quantum of magnetic flux is contained within each normal core.

The picture we start to build up is of an array of magnetic flux filaments, each containing one flux quantum, penetrating the superconductor in the mixed state. Each normal core is surrounded by a vortex of swirling supercurrent, which screens the superconducting region from the magnetic field contained in the core. It must be the case that the number of vortices per unit area, n, is related to the total magnetic induction by the equation $n = B/\Phi_0$. There is a repulsive force between vortices, which means that at sufficiently high n the lowest energy configuration is a close packed triangular *vortex lattice*. If the applied field is below H_{c1}, the superconductor is in the Meissner state, as the free energy gain in allowing partial penetration of magnetic flux is not beneficial.

The magnetic field profile of a superconductor in the mixed state is displayed in Fig. 2.5(a). Note that the spatial length scale between vortices is several hundred

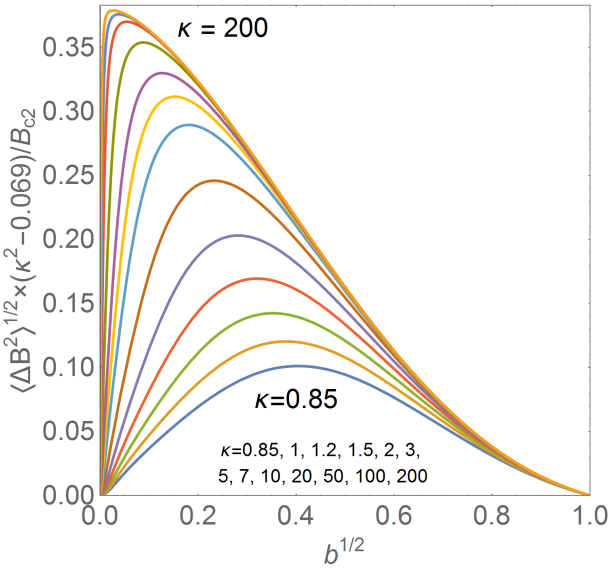

Fig. 2.6 Field dependence of the second moment of the magnetic field distribution of the ideal vortex lattice, $\langle \Delta B^2 \rangle$, for a variety of different values of κ. The data are plotted as a function of the square root of the reduced magnetic field $b^{1/2}$. Simulations were produced using the London model with a Gaussian cut-off following Ref. [24].

nanometres - orders of magnitude larger than the inter-atomic spacing. The probability distribution associated with this magnetic field profile is displayed in Fig. 2.5(b), and one can pick out several distinctive features. The peak in the field distribution (■) corresponds to the saddlepoint in the magnetic field profile. The maximum field (●) is found in the centre of the normal cores, and the minimum field (▲) is found at the position furthest away from all vortices.

We note from Fig. 2.5(b) that as the penetration depth increases, the field distribution becomes much narrower, and the value of the peak field moves closer to the average field, $\langle B \rangle$. In fact, the second moment of the field distribution, $\langle \Delta B^2 \rangle$, can be directly related to the magnetic penetration depth by the equation

$$\lambda^{-4} = C \langle \Delta B^2 \rangle, \tag{2.16}$$

where C is a parameter that generally depends on the reduced magnetic field, $b = \langle B \rangle / B_{c2}$ and the Ginzburg-Landau parameter, κ. The field dependence of $\langle \Delta B^2 \rangle$ is presented in Fig 2.6, from which some key features can be determined. Starting at $b = 0$, the second moment of the ideal vortex lattice increases from zero to a peak value, before decreasing to zero at $b = 1$. As κ increases, the peak moves closer to the point $b = 0$, and we see that for $\kappa > 50$ there is very little variation of $\langle \Delta B^2 \rangle$ in

the vicinity of the peak. In this regime, Eq. (2.16) becomes

$$\langle \Delta B^2 \rangle = 0.00371 \frac{\Phi_0^2}{\lambda^4}. \tag{2.17}$$

This approximation is only good in the vicinity of the peak value of the second moment, and we must exclude very small and very large reduced fields, b. In the limit of very small reduced fields ($b \ll 0.13/\kappa^2$), the second moment drops linearly to zero, and Eq. (2.16) is linear in b:

$$\langle \Delta B^2 \rangle = \frac{b\kappa^2}{8\pi^2} \frac{\Phi_0^2}{\lambda^4}. \tag{2.18}$$

It should be noted that this is only valid for $\kappa \geq 5$. Also for this κ regime, the field dependence over almost the entire reduced field range is well described by the approximation

$$\langle \Delta B^2 \rangle = 0.02958 \frac{(1-b)^2}{\kappa^4} \left[1 + 1.21(1-\sqrt{b})^3 \right]^2. \tag{2.19}$$

These approximations are useful when analysing muon spin spectroscopy experiments on type-II superconductors - this will be discussed in detail in Sec. 3.6.

2.3 The microscopic BCS theory

In Sec. 2.1, it was mentioned briefly that the superconducting state occurs when electrons form Cooper pairs below T_c. In this section we explore this idea in more detail, and highlight some important results that will be of use in the experimental chapters of this thesis.

BCS theory is built upon three major insights. The first is that the effective forces between electrons in condensed matter is not always repulsive as one might expect in the case of bare electrons. When screening effects are taken into account, the Coulomb potential decays exponentially with distance; much more rapidly than the $1/r$ potential that is valid in free space. The nature of the attractive component was hinted at by the *isotope effect*. Varying the isotope of elemental superconductors causes the transition temperature to change, with a functional form that depends roughly on a power of the atomic mass, M. Because changing the mass of the atoms in the crystal structure affects the electronic properties, it hints that phonons play a role in the superconductivity. In fact, the attractive interaction arises due to phonon emission and absorption between electrons, a phenomenon known as

electron-phonon coupling. In the BCS theory, the interaction potential, V_{eff}, is assumed to be independent of the wave-vector and frequency of the intermediary phonons, and can be written as

$$V_{\text{eff}}(\vec{q},\omega) = -V. \tag{2.20}$$

The second key insight underlying BCS theory came when Cooper showed that electrons at the Fermi surface are unstable in the presence of an arbitrarily small attractive interaction [25]. By considering two electrons with energies within $\hbar\omega_{\text{D}}$ of the Fermi energy, E_{F}, Cooper found that these electrons would form a bound state no matter how small the attractive interaction. The energy of the bound state is given by

$$E = -2\hbar\omega_{\text{D}} e^{-\frac{1}{\lambda_{\text{ep}}}}, \tag{2.21}$$

where the dimensionless *electron-phonon coupling parameter*, λ_{ep}, is defined by

$$\lambda_{\text{ep}} = N(E_{\text{F}})V, \tag{2.22}$$

and $N(E_{\text{F}})$ is the density of states at the Fermi level. For the elemental superconductors, λ_{ep} usually has a value of ~ 0.3. It is clear from Eq. (2.21) that this bound state will always exist no matter how small one makes λ_{ep}.

The final insight for BCS theory is the realization that as long as an attractive interaction exists at the Fermi level, essentially every electron on the Fermi surface will form a bound Cooper pair in order to minimise the total energy. In order to treat this mathematically, Schrieffer proposed a wavefunction that describes a coherent state of Cooper pairs. A pair creation operator can be defined in terms of the usual creation operators as

$$\hat{P}_{\text{k}}^{+} = c_{\text{k}\uparrow}^{+} c_{-\text{k}\downarrow}^{+}, \tag{2.23}$$

which has the effect of creating a spin singlet electron pair with zero total crystal momentum. Then the normalized BCS wavefunction is

$$|\Psi_{\text{BCS}}\rangle = \prod_{\text{k}} \left(u_{\text{k}}^{*} + v_{\text{k}}^{*}\hat{P}_{\text{k}}^{+}\right)|0\rangle, \tag{2.24}$$

where

$$|u_{\text{k}}|^2 + |v_{\text{k}}|^2 = 1. \tag{2.25}$$

Here, v_{k} is the probability amplitude that the $(\vec{k},-\vec{k})$ state is occupied, and u_{k} is the probability of the empty state. The wavefunction acts on the vacuum state, $|0\rangle$,

which in this case corresponds to the state at the Fermi level with no electrons. To find the ground state of the system, it is necessary to minimize the total energy with respect to the parameters v_k and u_k. At $T = 0$, it is found that a gap forms between the band of superconducting electrons and the Fermi level. The magnitude of this gap, $|\Delta|$, is the *BCS gap parameter*, and is related to the parameters of the theory by the simple equation

$$|\Delta| = V \sum_k u_k v_k. \tag{2.26}$$

Above $T = 0$, the effect of quasiparticle excitations must be accounted for, which reduce the magnitude of Δ. The temperature dependence of the BCS gap, $\Delta(T)$, is contained implicitly in the integral equation

$$\frac{1}{\lambda_{ep}} = \int_0^{\hbar\omega_D} d\varepsilon \frac{1}{\sqrt{\varepsilon^2 + |\Delta(T)|^2}} \tanh\left(\frac{\sqrt{\varepsilon^2 + |\Delta(T)|^2}}{2k_B T}\right). \tag{2.27}$$

Here we identify $\sqrt{\varepsilon^2 + |\Delta(T)|^2}$ as the excitation spectrum for quasiparticles excited above the BCS ground state, and the integration variable, ε, is the energy of the electrons measured with respect to the Fermi level. Solving the BCS gap equation in the limit as $T \to 0$ leads to the zero temperature value of the energy gap, given by

$$\frac{2\Delta_0}{k_B T_c} = 3.528. \tag{2.28}$$

Here $k_B = 8.617 \times 10^{-2}\,\mathrm{meV\,K^{-1}}$ is the Boltzmann constant, and $2\Delta_0$ can be interpreted as the energy required to break apart a Cooper pair. Also, at T_c, $\Delta \to 0$, and we can calculate the BCS equation for T_c:

$$k_B T_c = 1.13 \hbar\omega_D e^{-\frac{1}{\lambda_{ep}}}. \tag{2.29}$$

Note the similarities between this equation and Cooper's original expression for the energy of a Cooper pair, Eq. (2.21). The typical spacing of electrons in a Cooper pair is encoded in the BCS coherence length, ξ_0, which is related to the superconducting energy gap and the Fermi velocity v_F by the equation

$$\xi_0 = \frac{\hbar v_F}{\pi\Delta}. \tag{2.30}$$

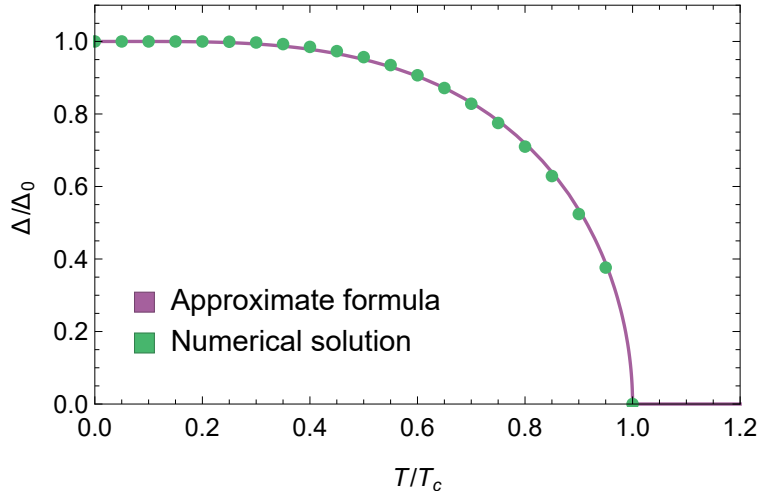

Fig. 2.7 Data points are the results of a numerical solution to Eq. (2.27). The solid line is the approximation to the BCS gap, given by Eq. (2.32)

The Fermi velocity on a spherical Fermi surface is related to the carrier density and the effective mass by the equation:

$$n = \frac{1}{3\pi^2}\left(\frac{m^* v_{\mathrm{F}}}{\hbar}\right)^3. \tag{2.31}$$

The BCS gap equation may be solved numerically in order to find $\Delta(T)$. Alternatively, an approximation for the temperature dependence is given by

$$\Delta(T) = \Delta_0 \tanh\left\{1.82\left[1.018\left(\frac{T_{\mathrm{c}}}{T}-1\right)\right]^{0.51}\right\}. \tag{2.32}$$

The results of both of these calculations are presented in Fig. 2.7. In calculations, the approximate form is used in order to improve computation time. As a final observation, we note that the superconducting gap $\Delta(T)$ fulfils many of the requirements placed on the superconducting wavefunction, $\psi(T)$, in GL theory. It was shown by Gor'kov in 1959 [21] that GL theory can in fact be derived from the BCS theory in an appropriate limit, therefore providing a microscopic explanation of ψ as describing the coherent state formed by superconducting Cooper pairs. Gor'kov also showed that ψ is directly proportional to Δ, and thus the interpretation of $|\psi|^2$ as the observable parameter, n_{s}, was verified.

2.4 Unconventional superconductivity

Built into BCS theory is the assumption that the superconducting gap, Δ_0, is isotropic around the Fermi surface. In the general case, the total wavefunction of the pair can be decomposed into a product of an orbital wavefunction and a spin component [26]:

$$|\Psi_{\vec{k}ss'}\rangle = \Phi(\vec{k})\chi(s,s'), \tag{2.33}$$

where the $\vec{k}$-dependence is contained in the orbital wavefunction, $\Phi(\vec{k})$, and the spin wavefunction $\chi(s,s')$ describes the spin state of each electron in the pair. The Pauli principle requires that the total wavefunction is completely antisymmetric under electron exchange, i.e. as $\vec{k} \to -\vec{k}$ and $s \to s'$. This antisymmetry can be carried by either the orbital or the spin part.

Consider $\Phi(\vec{k})$ - exchanging the electrons in the pair is the same as making the replacement $\vec{k} \to -\vec{k}$. Using operator language, we operate on $\Phi(\vec{k})$ with the parity operator, $\hat{P}$, and investigate the output:

$$\Phi(-\vec{k}) = \hat{P}\Phi(\vec{k}) = P\Phi(\vec{k}), \tag{2.34}$$

where $P = \pm 1$ are the eigenvalues of the parity operator. If $P = +1$ then the parity is *even*, and the resulting orbital wavefunction is *symmetric*. If $P = -1$ then the parity is *odd*, and the resulting orbital wavefunction is *antisymmetric*. In the case of even parity, the spin wavefunction must be antisymmetric, which corresponds to a spin-singlet wavefunction with total spin $S = 0$:

$$\chi(s,s') = \frac{1}{\sqrt{2}}\{|\uparrow\downarrow\rangle - |\downarrow\uparrow\rangle\}. \tag{2.35}$$

This wavefunction has the property that $\chi(s,s') = -\chi(s',s)$ as required. Finally, in the case of odd parity, the spin wavefunction must be symmetric, which corresponds to a spin-triplet wavefunction with total spin $S = 1$:

$$\chi(s,s') = \begin{cases} |\uparrow\uparrow\rangle \\ \frac{1}{\sqrt{2}}\{|\uparrow\downarrow\rangle + |\downarrow\uparrow\rangle\} \\ |\downarrow\downarrow\rangle \end{cases} \tag{2.36}$$

This wavefunction has the property that $\chi(s,s') = \chi(s',s)$ as required. If the Fermi surface has spherical symmetry, then parity is directly related to the orbital quantum number l: even parity has $l = 0,2,4,6,...$ and odd parity has $l = 1,3,5,....$ The BCS

Cooper pair is a bound state of spin-singlet electrons that have zero total angular momentum ($l = 0$). This even-parity singlet state constitutes *conventional* pairing, which is classified as an *s*-wave state in the language of atomic orbitals. Any other type of superconducting electron pairing is *unconventional*, and it is this pairing symmetry that is referenced when classifying superconductors as conventional or unconventional.

There are two key symmetries that must be considered when determining whether a Cooper pair may form in a particular superconducting system. The first is time-reversal symmetry, where the time reversal operator is defined by

$$\hat{T} : t \mapsto -t. \tag{2.37}$$

Observables may either be odd or even under the time-reversal operation - momentum and spin are both odd. The second important symmetry is inversion symmetry (denoted by the inversion operator:

$$\hat{I} : \begin{bmatrix} x \\ y \\ z \end{bmatrix} \mapsto \begin{bmatrix} -x \\ -y \\ -z \end{bmatrix}. \tag{2.38}$$

Once again, observables may be odd or even under inversion - in this case momentum is odd and spin is even.

In the case of even-parity spin-singlet pairing, it is necessary that the system is at least invariant under time-reversal. This is because the two particles $|\vec{k}\uparrow\rangle$ and $\hat{T}|\vec{k}\uparrow\rangle = |-\vec{k}\downarrow\rangle$ may be linearly combined to form a spin-singlet state (Eq. (2.35)). Furthermore, spin-triplet pairing requires inversion symmetry at the very least, as the two particles $|\vec{k}\uparrow\rangle$ and $\hat{I}|\vec{k}\uparrow\rangle = |-\vec{k}\uparrow\rangle$ may be combined to form a spin-triplet state with parallel spins. Including time-reversal symmetry allows all three spin-triplet configurations defined in Eq. (2.36) to be realised. The conditions of requiring time-reversal and inversion symmetry are known as Anderson's theorem [27, 28]. If either, or both, of these symmetries are absent, then there is consequences on the allowable pairing states.

The symmetry of the pair wavefunction is reflected in the structure of the gap parameter, $\Delta(\vec{k})$ (c.f. Eq. (2.26)). The BCS gap is independent of $\vec{k}$; however, in general the $\vec{k}$-dependence of the gap can be written

$$\Delta(\vec{k}) = \Delta_0(\vec{k}) + \vec{\sigma} \cdot \vec{d}(\vec{k}), \tag{2.39}$$

where $\Delta_0(\vec{k})$ is the scalar, singlet component, and $\vec{d}(\vec{k})$ is the vector, triplet component ($\vec{\sigma}$ is the vector of Pauli spin matrices). In the case of even-parity, $\vec{d}(\vec{k}) = 0$ and $\Delta_0(\vec{k})$ is symmetric, whereas in the case of odd-parity, $\Delta_0(\vec{k}) = 0$ and $\vec{d}(-\vec{k})$ is antisymmetric. The gap function is represented in spin space by the 2×2 matrix

$$\hat{\Delta}(\vec{k}) = i\Delta(\vec{k})\hat{\sigma}^y. \tag{2.40}$$

If this matrix has the property that $\hat{\Delta}\hat{\Delta}^\dagger \propto \hat{I}$ then it is called a *unitary* matrix. This means that the columns of the matrix are orthogonal, and form a basis for the column space of the matrix. However, if time-reversal and/or inversion symmetry is absent, then the matrices cease to have this property, in which case they are called *non-unitary*. In this case, the columns of the matrix are linearly dependent.

Systems in which the crystal structure lacks inversion symmetry are called as *noncentrosymmetric*. In these systems, parity is no longer a good quantum number - i.e. the Hamiltonian of the system does not commute with the parity operator. The previous discussion relied on the fact that the total pair wavefunction, $\Psi(\vec{k}, s, s')$, could be decomposed into an orbital and a spin-dependent component, each of which was either symmetric or antisymmetric. Losing inversion symmetry means that the orbital wavefunction, $\Phi(\vec{k})$, can no longer be completely symmetric or antisymmetric. Therefore the spin wavefunction $\chi(s, s')$ is also no longer purely spin-singlet or spin-triplet - it may exist as an *admixture* of these two components [29]. This possibility of the existence of mixed-parity superconducting ground states is one of the key results of the theory of noncentrosymmetric superconductivity.

Another effect of the loss of inversion symmetry is that it allows the existence of a Rashba-type antisymmetric spin-orbit coupling (ASOC). This type of interaction is quantified by a term in the Hamiltonian of the form

$$\alpha \vec{g}_{\vec{k}} \cdot \vec{S}, \tag{2.41}$$

where $\vec{S}$ is the spin vector, α is a constant that quantifies the strength of the coupling, and $g_{\vec{k}} = -g_{-\vec{k}}$ is an antisymmetric vector that characterizes the ASOC. This type of spin-orbit coupling leads to a splitting of the Fermi surface, similar to Zeeman splitting into spin-up and spin-down bands in the presence of an external magnetic field. The difference here is that the spin-quantization axis is $\vec{k}$-dependent. In general, losing inversion symmetry is detrimental to the formation of triplet pairing states, however, there are some directions in which the triplet state is topologically protected. This occurs whenever $\vec{d}(\vec{k})$ is parallel to $\vec{g}_{\vec{k}}$ [30].

A superconductor is said to be *fully gapped* if the gap function at no point on the Fermi surface is equal to zero. Superconductors in which the symmetry of the gap is not the same as in BCS theory are said to exhibit unconventional superconductivity. The structure of the superconducting gap is determined by the point group symmetry of the crystal structure of the superconducting material. This is because any transformations which leave the crystal structure invariant must also transform the superconducting gap identically. This requirement to obey the symmetries of the crystal structure can give rise to a k-dependent gap, in which Δ does not have the same magnitude in all directions. This can lead to anisotropy in observable parameters, such as the magnetic penetration depth and the critical fields. Positions on the Fermi surface where the gap has a zero value are called *nodes*, and we can distinguish between *point nodes* and *line nodes*. To account for this, an angular dependence can be included for Δ by the equation

$$\Delta_{\mathrm{k}} = \Delta(T)F(\theta,\phi). \tag{2.42}$$

Here $\Delta(T)$ is an angle-independent positive value that denotes the magnitude of the gap, and the function F gives the angular dependence of Δ_{k} on the Fermi surface. In cylindrical symmetry, $F = F(\phi)$, and for a spherical Fermi surface $F = F(\theta,\phi)$, where θ and ϕ are the polar and azimuthal angles, respectively.

The BCS theory is only exact in the weak coupling limit. Whilst there is no universally accepted cut-off, weak coupling is most commonly considered the case where $\lambda_{\mathrm{ep}} < 1$. If the coupling is stronger, then the effect of the electrons on the phonons must also be taken into account. For example, phonon frequencies are affected by the interaction with the electrons. In the strong coupling limit, McMillan has derived an approximate expression for the critical temperature which replaces Eq. (2.29) [31]:

$$k_{\mathrm{B}}T_{\mathrm{c}} = \frac{\hbar\omega_{\mathrm{D}}}{1.45}\exp\left(\frac{1.04(1+\lambda)}{\lambda-\mu^*(1+0.62\lambda)}\right), \tag{2.43}$$

where μ^* is the Coulomb pseudo-potential, which accounts for the screened Coulomb potential between the electrons, and typically has a value between 0.1 and 0.15. A useful reformulation of this equation allows one to estimate λ_{ep} from T_{c} and Θ_{D}:

$$\lambda_{\mathrm{ep}} = \frac{1.04+\mu^*\ln(\Theta_{\mathrm{D}}/1.45T_{\mathrm{c}})}{(1-0.62\mu^*)\ln(\Theta_{\mathrm{D}}/1.45T_{\mathrm{c}})-1.04}. \tag{2.44}$$

The parameters T_{c} and Θ_{D} are readily measured via heat capacity and magnetization measurements in the laboratory.

In order to quantify the resulting deviations in the observable parameters of the superconductor, the alpha model is used [32], such that the value of the zero temperature energy gap, Δ_0, becomes a variable that can be fitted to data. The temperature dependence of $\Delta(T)$ is still modelled by the expected BCS expression, meaning that the model is not self consistent. However, it does allow the magnitude of any deviation from the BCS theory to be quantified. In the alpha model, the BCS parameter, Eq. (2.28), is rewritten as

$$\frac{\Delta_0}{k_{\mathrm{B}}T_{\mathrm{c}}} = \alpha, \tag{2.45}$$

where the value $\alpha_{\mathrm{BCS}} = 1.764$ yields the BCS value in the weak coupling limit.

2.5 The clean and dirty limit

In many superconducting systems, most notably metallic alloys, a high level of intrinsic disorder exists in the structure. This can lead to very short values for the electronic mean free-path. Equation (2.30) defines the BCS coherence length, ξ_0, which is the spatial extent of a Cooper pair. It is expected that if the mean free path is much larger than ξ_0, then scattering effects will have a negligible effect on the superconductivity. We can define two regimes:

- If $\xi_0/l_{\mathrm{e}} \ll 1$, then this is called the *clean limit*.
- If $\xi_0/l_{\mathrm{e}} \gg 1$, then we are in the *dirty limit*.

The Ginzburg-Landau coherence length, $\xi(T)$, is the length scale over which the order parameter, ψ, may vary. In the clean limit, where quasiparticle scattering is assumed to be negligible, these parameters are related by the equation

$$\xi(T) = 0.74\xi_0 \left(\frac{T_{\mathrm{c}}}{T_{\mathrm{c}} - T}\right)^{1/2}. \tag{2.46}$$

However, in the dirty limit the GL coherence length is reduced, and is given by

$$\xi(T) = 0.85\sqrt{\xi_0 l_{\mathrm{e}}} \left(\frac{T_{\mathrm{c}}}{T_{\mathrm{c}} - T}\right)^{1/2}, \tag{2.47}$$

where there is now an explicit dependence on l_{e}. Introducing impurities is therefore expected to decrease the GL coherence length.

The magnetic penetration depth is also affected by the mean free path. In the clean limit, we have

$$\lambda(T) = \frac{\lambda_{\mathrm{L}}}{\sqrt{2}} \left(\frac{T_{\mathrm{c}}}{T_{\mathrm{c}} - T} \right)^{1/2}, \tag{2.48}$$

and in the dirty limit:

$$\lambda(T) = 0.64 \lambda_{\mathrm{L}} \sqrt{\frac{\xi_0}{l_{\mathrm{e}}}} \left(\frac{T_{\mathrm{c}}}{T_{\mathrm{c}} - T} \right)^{1/2}. \tag{2.49}$$

Therefore the effective penetration depth is increased in the presence of impurities. Scattering electrons can lead to quasiparticle excitations, lowering the superfluid density, which in turn leads to less effective screening of magnetic fields. The zero-temperature limit of the effective penetration depth in a dirty superconductor is given by the important equation [33]

$$\lambda(0) = \lambda_{\mathrm{L}}(0) \sqrt{1 + \frac{\xi_0}{l_{\mathrm{e}}}}. \tag{2.50}$$

Also of interest is the relationship between the Ginzburg-Landau coherence length and the BCS coherence length at low temperatures in the dirty limit. It is possible to express the ratio of these two parameters by the relation [33]

$$\frac{\xi(0)}{\xi_0} = \frac{\pi}{2\sqrt{3}} \left(1 + \frac{\xi_0}{l_{\mathrm{e}}} \right)^{-1/2}. \tag{2.51}$$

These considerations also lead to a difference in the definition of the GL parameter, κ. In the clean limit, κ is given by

$$\kappa = 0.96 \frac{\lambda_{\mathrm{L}}}{\xi_0}, \tag{2.52}$$

and in the dirty limit:

$$\kappa = 0.715 \frac{\lambda_{\mathrm{L}}}{l_{\mathrm{e}}}. \tag{2.53}$$

2.6 Pair-breaking mechanisms and the upper critical field

In general there are two ways in which a magnetic field suppresses superconductivity. The first mechanism arises as a result of geometrical considerations of the

vortex lattice. In the mixed state, magnetic flux penetrates the sample in filaments surrounded by vortices, each containing one quantum of magnetic flux. The number density of vortices per unit area, n, is related to the applied magnetic field, B, by the equation $n = B/\Phi_0$. Therefore as the magnetic field is increased, the inter-vortex spacing must decrease. The size of the normal core is given approximately by ξ, the coherence length, and thus we can see that if B continues to rise the normal cores will eventually begin to overlap. At this point, superconductivity is effectively 'squeezed out' of the system, giving rise to the *orbital critical field*, H_{c2}^{orb}:

$$\mu_0 H_{c2}^{orb} = \frac{\Phi_0}{2\pi\xi^2(T)}. \tag{2.54}$$

In single band superconductors, the maximum orbital critical field may be estimated from experimental measurements of the slope at T_c by the relation

$$\mu_0 H_{c2}^{orb}(0) = -AT_c \frac{dH_{c2}(T)}{dT}\Big|_{T_c}, \tag{2.55}$$

where $A = 0.73$ and 0.69 in the clean and dirty limits, respectively.

The second mechanism arises due to Zeeman splitting of spin-singlet Cooper pairs. Under the alpha model, the *Pauli limiting field*, H_P, is given by

$$\mu_0 H_P = 1.86 T_c \left(\frac{\alpha}{\alpha_{BCS}}\right), \tag{2.56}$$

where the condition is derived by equating the Zeeman energy with the superconducting condensation energy. The observed H_{c2} will generally feature some contribution from both of these limiting processes, and the relative magnitudes of the orbital and Pauli limiting effects are encoded in the Maki parameter:

$$\alpha_M = \sqrt{2}\frac{H_{c2}^{orb}(0)}{H_P(0)}. \tag{2.57}$$

In the limit where $H_P \gg H_{c2}^{orb}$, we have $\alpha_M = 0$, in which case the Pauli pair breaking effect is negligible and the superconductor is orbital limited. Superconductors that break the Pauli limit are of interest due to the possibility of unconventional spin states of the Cooper pairs.

The influence of orbital limiting, Pauli limiting, and spin-orbit scattering of quasiparticles on the measured upper critical field is modelled by the Werthamer, Helfand, and Hohenberg (WHH) theory for single-band, dirty limit superconductors.

The upper critical field is calculated implicitly by the equation

$$\ln\frac{1}{t} = \sum_{\nu=-\infty}^{\infty}\left\{\frac{1}{|2\nu+1|} - \left[|2\nu+1| + \frac{h}{t} + \frac{(\alpha_{\mathrm{M}}h/t)^2}{|2\nu+1|+(h+\lambda_{\mathrm{so}})/t}\right]^{-1}\right\}, \tag{2.58}$$

where λ_{so} is the spin-orbit scattering rate, $t = T/T_{\mathrm{c}}$, and

$$h = -\left(\frac{4}{\pi^2}\right)\frac{H_{\mathrm{c2}}(T)/T_{\mathrm{c}}}{dH_{\mathrm{c2}}(T)/dT|_{T_{\mathrm{c}}}}. \tag{2.59}$$

In order to determine the validity of analysing superconductors in the WHH formalism, it is necessary to compare the value of α_{M} calculated via Eq. (2.57) with the alternative equation provided by WHH:

$$\alpha_{\mathrm{M}} = -0.528\frac{dH_{\mathrm{c2}}}{dT}\Big|_{T_{\mathrm{c}}}. \tag{2.60}$$

Requiring agreement between the two values justifies usage of the WHH theory to analyse the superconducting properties of a given material.

2.7 Applications of the theory of superconductivity

In this section, the important ideas discussed in the previous sections will be summarized, and applied to the experiments one can perform in the laboratory to investigate superconductivity. In particular, it will be shown how to apply the alpha model to analyse the heat capacity, transport properties, magnetization, and the superfluid density of superconductors, as these results will be used extensively in the following chapters. The superconducting properties are intimately linked with those of the normal state - this is particularly clear when considering how often a term involving the Debye frequency appears in the BCS theory. Therefore, an outline of the normal state properties will also be given.

2.7.1 Heat capacity

The normal state heat capacity contains contributions from the electronic density of states, and the phonon modes in the crystal. At room temperature, the heat capacity is dominated by the phonon contributions, whilst at low temperatures the electronic contributions become dominant. The heat capacity in the normal state

can be calculated over the full temperature range using the following model which accounts for the electronic and phononic contributions:

$$C(T) = \gamma T + C_D(T) + C_E(T). \tag{2.61}$$

The first term accounts fully for the electronic contribution to the heat capacity, where the Sommerfeld constant, γ, is related to the density of states at the Fermi level by the equation

$$\gamma = \frac{\pi^2 k_B^2}{3} N(E_F). \tag{2.62}$$

The second term in Eq. (2.61) is the contribution from acoustic phonons, given by the Debye model

$$C_D(T) = 9 N_D k_B \left(\frac{T}{\Theta_D}\right)^3 \int_0^{\Theta_D/T} \frac{x^4 e^x}{(e^x - 1)^2} dx, \tag{2.63}$$

where Θ_D is the Debye temperature and N_D is the molar density of Debye oscillators. The final term of Eq. (2.61) accounts for optical phonon modes, which are described by the Einstein model:

$$C_E(T) = 3RN_E \left(\frac{\Theta_E}{T}\right)^2 \frac{\exp(\Theta_E/T)}{(\exp(\Theta_E/T) - 1)^2}, \tag{2.64}$$

where Θ_E is the Einstein temperature and N_E is the molar density of Einstein oscillators. At high temperatures, the total heat capacity is expected to approach the Dulong-Petit limit,

$$C_{DP} = 3pR, \tag{2.65}$$

where R is the gas constant and p is the number of atoms per formula unit cell. [34] The factor of 3 represents the vibrational degrees of freedom of the atoms in the crystal lattice.

In the superconducting state, the electronic contribution to the heat capacity is no longer linear in T. In the BCS theory, the Fermi surface is fully gapped, and therefore there are no states within $k_B T$ of the Fermi level when $T \ll T_c$. The heat capacity in this case has an exponential dependence of the form $C \propto \exp(-\Delta_0/k_B T_c)$, which is indicative of a mechanism with an activation energy of Δ_0. We can interpret this as the thermal excitation of quasiparticles. Unconventional superconductors may exhibit nodes in the gap function, and therefore we expect this to have the biggest observable effect at low temperatures [35].

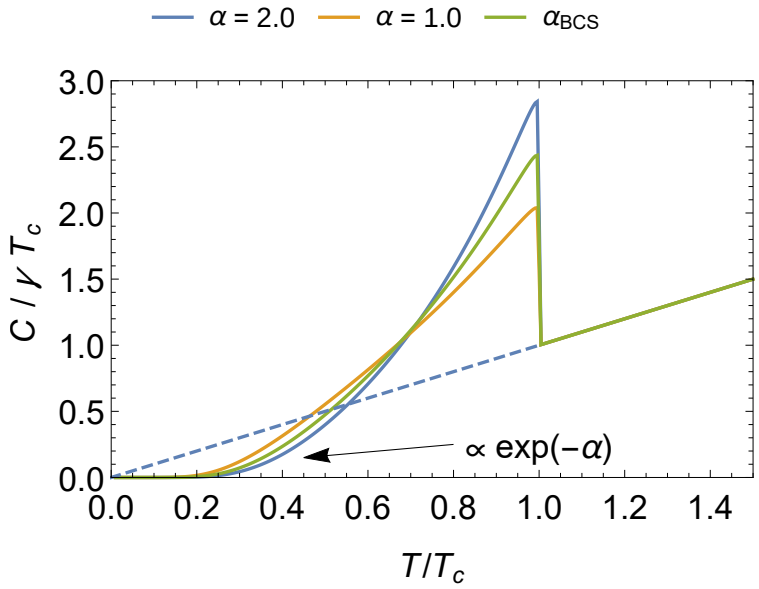

Fig. 2.8 Simulation of the heat capacity in the vicinity of T_c for the BCS value of $\alpha = \Delta_0/k_B T_c$, and two values above and below.

The heat capacity below T_c is calculated via the BCS expression for the normalized entropy [36]:

$$\frac{S}{\gamma T_c} = -\frac{6}{\pi^2}\frac{\Delta_0}{k_B T_c}\int_0^\infty d\varepsilon (f(E)\ln f(E) + (1-f)\ln(1-f)), \tag{2.66}$$

where the integral is over the energies of the normal electrons relative to the Fermi level, ε; $E = \sqrt{\varepsilon^2 + \Delta^2(T)}$ is the quasiparticle excitation spectrum, and the Fermi-Dirac distribution, $f(E)$, is given by

$$f(E) = \left[\exp\left(\frac{E}{k_B T}\right) + 1\right]^{-1}. \tag{2.67}$$

The heat capacity is then related to the first derivative of the normalized entropy by the relation

$$\frac{C_{sc}}{\gamma T_c} = T\frac{d(S/\gamma T_c)}{dT}. \tag{2.68}$$

In order to fit this expression to experimental data, the approximation for $\Delta(T)$ given in Eq. (2.32) is used, and the value of Δ_0 is allowed to vary from the BCS value, as in the alpha model (Eq. (2.45)). Simulated plots of the heat capacity for values of α, above, below, and equal to the BCS value of alpha are presented in Fig. 2.8. A discontinuity arises in the heat capacity at T_c, where the magnitude of the difference between the superconducting and normal values, ΔC, is equal to 1.426 in BCS theory.

This is extended by the α-model, where the magnitude of the discontinuity is given by

$$\frac{\Delta C}{\gamma T_c} = 1.426 \left(\frac{\alpha}{\alpha_{BCS}} \right)^2 . \tag{2.69}$$

The magnitude of the discontinuity is readily measured, and thus allows estimation of the degree of deviation from the conventional theory of superconductivity.

2.7.2 Superfluid density

We have seen that as T approaches T_c, the magnetic penetration depth, λ, diverges. It is beneficial for data analysis to work with the superfluid density, ρ_s, as this quantity is proportional to the inverse square of the penetration depth, and therefore approaches 0 as $T \to T_c$. For a constant Fermi velocity, the normalized superfluid density is given by the equation [37]

$$\rho_s \equiv \frac{\lambda^{-2}(T)}{\lambda^{-2}(0)} = \oint_{FS} dS \left[1 + 2 \int_{\Delta}^{\infty} dE \left(\frac{\partial f}{\partial E} \right) \frac{E}{\sqrt{E^2 - \Delta_k^2}} \right] . \tag{2.70}$$

This equation provides the link between the magnetic penetration depth and the microscopic theory of superconductivity. Note that we are averaging over the entire Fermi surface, which allows the penetration depth arising due to a k-dependent superconducting gap to be calculated. The appropriate surface element, dS, will depend on whether the FS has cylindrical or spherical symmetry.

In a fully gapped superconductor, the superfluid density is expected to plateau as the temperature is lowered. This is because when the thermal energy, $k_B T$, is much lower than the pair breaking energy, $2\Delta_0$, the superconducting electron density will not be affected by thermal fluctuations. In the presence of a node, arbitrarily small thermal fluctuations may cause quasiparticle excitation, leading to a depletion of n_s. The superfluid density at low temperature is in this case expected to vary linearly with T for line nodes, or as T^2 in the presence of point nodes. This is similar to the expected low temperature behaviour of the heat capacity.

In the dirty limit, an analytical expression for calculating the superfluid density is given by:

$$\rho_s = \frac{\Delta(T)}{\Delta(0)} \tanh \left(\frac{\Delta(T)}{2 k_B T} \right) , \tag{2.71}$$

where the approximate BCS formula for $\Delta(T)$, Eq. (2.32) is used.

2.7.3 Resistivity

The normal state resistivity is analysed in the framework of the Bloch-Grüneisen (BG) model, which describes the resistivity arising due to electrons scattering from longitudinal acoustic phonons. The temperature dependence of the resistivity, $\rho(T)$, is modelled as

$$\rho(T) = \rho_0 + \rho_{\mathrm{BG}}(T), \tag{2.72}$$

where

$$\rho_{\mathrm{BG}}(T) = 4r\left(\frac{T}{\Theta_{\mathrm{R}}}\right)^5 \int_0^{\Theta_{\mathrm{R}}/T} \frac{x^5}{(e^x-1)(1-e^{-x})}dx \tag{2.73}$$

is the BG resistivity [38]. The parameter, Θ_{R}, is related to the Debye temperature of the material, and r is a material dependent constant. The residual resistivity, ρ_0, is the value at which the low temperature resistivity levels off, and is related to the density of states and the mean free path by

$$\rho_0^{-1} = \frac{2}{3}N(E_{\mathrm{F}})e^2 v_{\mathrm{F}} l_{\mathrm{e}}. \tag{2.74}$$

Chapter 3

Experimental techniques

3.1 Sample preparation

Polycrystalline samples of Re_3Ta, La_7Ir_3, $LuRuB_2$, and $YRuB_2$ were produced using a tri-arc furnace. This consists of a trio of tungsten electrodes connected to a DC welding power supply and a water-cooled copper hearth. A high voltage was applied to the electrodes, and a current was stabilised by touching the tip of the electrodes to the base of the copper hearth. By pulling the electrodes away and positioning them above the sample, a stable arc of current is maintained. Stoichiometric quantities of the constituent elements were measured and arranged on the copper hearth, before the sample chamber was sealed and evacuated using a rotary pump. In order to reduce the effect of oxygen contamination, the chamber was flushed with Argon and re-evacuated at least 5 times before the electrodes were powered on. The melt was carried out under a continuous flow of Argon, and the sample was flipped and re-melted at least three times to improve the homogeneity of the final product. Generally this initial melt was followed by a longer period of annealing at high temperature. This was achieved by sealing the samples in quartz tubes that had been evacuated or left under a partial pressure of Argon, and then transferring the tubes to a box furnace.

3.2 Magnetization

3.2.1 SQUID Magnetometry

Measurements of magnetization as a function of temperature were performed using a Quantum Design Magnetic Property Measurement System (MPMS) [39]. A

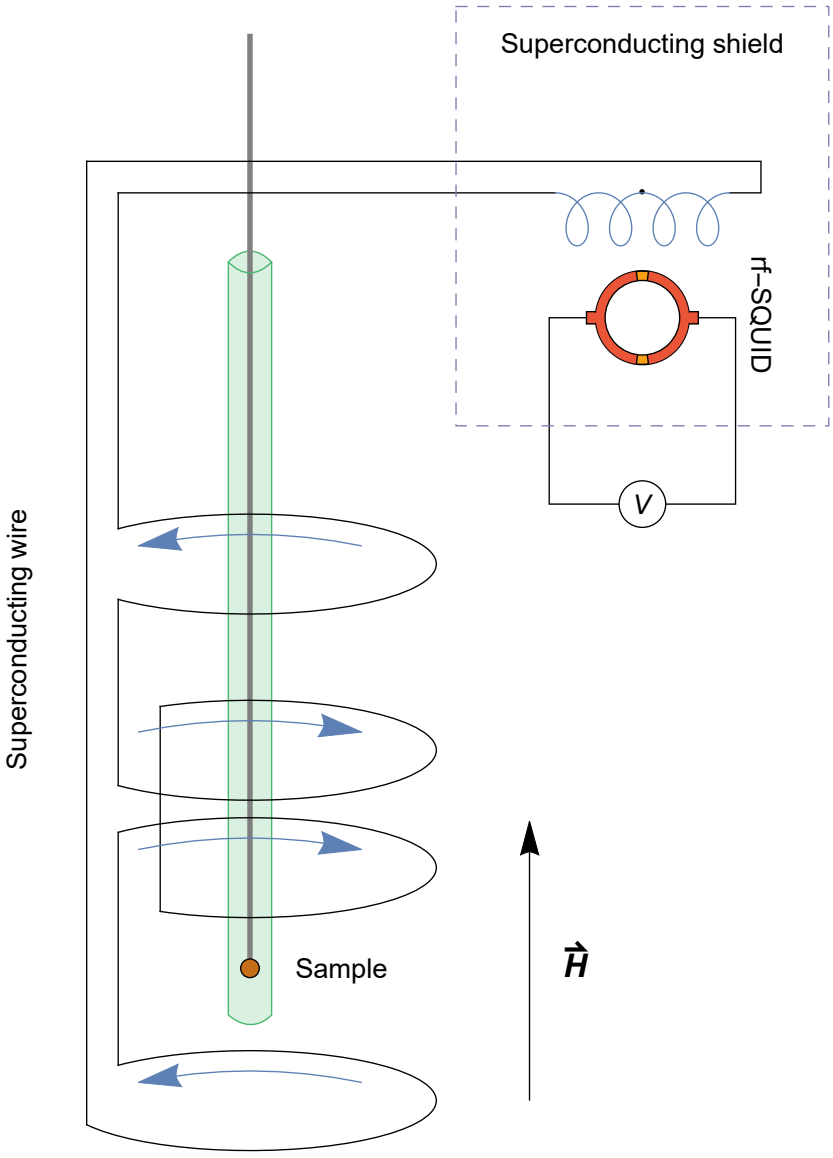

Fig. 3.1 Schematic diagram of the SQUID magnetometer used to make magnetization measurements. A magnetic field is applied along the axis of the pick-up coils. The SQUID is housed inside a superconducting shield, which protects it from external sources of magnetic field.

schematic diagram of the magnetometer is presented in Fig. 3.1. The MPMS consists of a sample probe immersed in a liquid helium bath, surrounded by a jacket of liquid nitrogen. Measurements between 1.8 K and 400 K are possible, and a magnetic induction of up to 5 T may be applied using the superconducting magnet. The key components are the superconducting detection coils through which the sample is moved, and the superconducting quantum interference device (SQUID) - a ring of superconducting material that contains two Josephson junctions. The detection coils are configured as a second-order gradiometer, which consists of an upper clockwise winding, two central anticlockwise windings, and a final lower clockwise winding. The SQUID provides an extremely sensitive way of measuring magnetic fields; however in this configuration the SQUID does not directly measure the magnetization of the sample, but instead behaves as a highly sensitive current to voltage converter.

To measure the magnetization of a sample, it must be mounted in a non-magnetic holder. The sample holder is attached to a sample transport rod, which allows the entire construction to be inserted into the sample space. The top end of the sample rod is attached to a stepper motor that drives the sample rod vertically through the detection coils in discrete steps. Discrete steps are possible because the components of the detection circuit are all made of superconducting materials - the induced current in the coils due to the motion of the magnetized sample does not decay as it would in a normal conductor. During a single measurement the sample is moved symmetrically about the centre of the pick-up coils, typically over a scan length of 4 cm divided into 32 points. The induced current in the detection coils couples inductively to the SQUID sensor, which is configured to work as a highly linear current to voltage converter. Thus the output voltage of the SQUID electronics is directly proportional to the magnetization of the sample. Calibration using a sample with known mass and magnetic susceptibility (typically Palladium) thus provides a highly accurate way of determining the magnetization of unknown samples.

A magnetized sample is expected to behave like an ideal magnetic dipole. In order for this to be true, the sample must be much smaller than the length of the detection coils. To find the magnitude of the dipole moment, γ, the experimental voltage response as a function of position is used to fit the equation

$$\begin{aligned} V(x) = \alpha + \beta x + \gamma(2[R^2 + (x+\delta)^2]^{-\frac{3}{2}} \\ -[R^2 + (x+\Omega+\delta)^2]^{-\frac{3}{2}} - [R^2 + (x-\Omega+\delta)^2]^{-\frac{3}{2}}), \end{aligned} \tag{3.1}$$

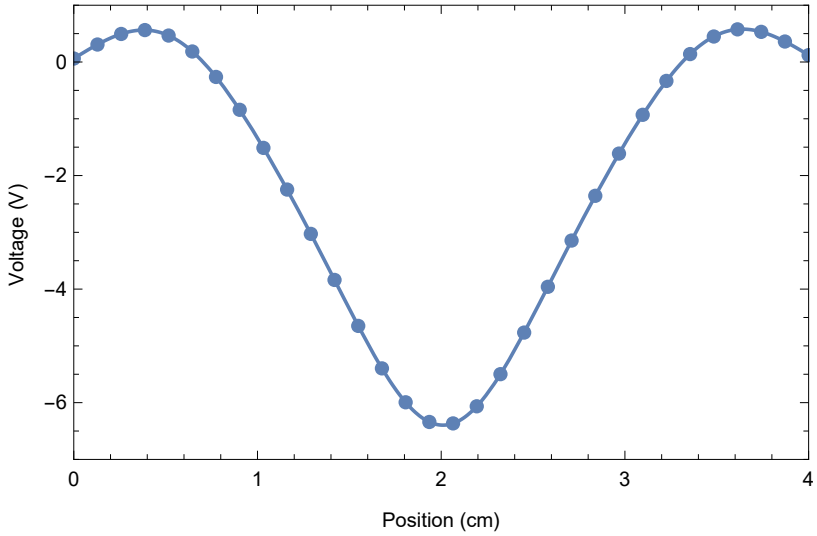

Fig. 3.2 Typical voltage response as a function of position for a diamagnetic sample.

where x is the vertical sample position, α is a constant voltage offset, β is a linear background term, and δ is a vertical offset. The two fixed constants R and Ω are the longitudinal coil radius (0.97 cm) and the longitudinal coil separation (1.519 cm), respectively. An example curve is shown in Fig. 3.2 with a plot of Eq. (3.1).

Magnetic units

The MPMS reports magnetization in electromagnetic units, emu, whereas the desired unit in SI is $\mathrm{A\,m^{-1}}$. The raw magnetization is first converted into CGS units by normalizing by the sample volume, where $[M_{\mathrm{CGS}}] = \mathrm{emu\ cm^{-3}}$. The sample volume may be estimated from the sample mass, and the calculated density based on the unit cell of the material. This is then converted into the SI system by the simple relation $M_{\mathrm{SI}} = 10^3\, M_{\mathrm{CGS}}$.

The dimensionless magnetic susceptibility, χ, is equal to the ratio of the magnetization and the applied field. The MPMS reports the applied magnetic field in CGS units of Gauss, which is converted to SI units by the relation $H_{\mathrm{SI}} = (10^3/4\pi)\, H_{\mathrm{CGS}}$. The effective magnetic susceptibility, $\chi_{\mathrm{eff}} = M_{\mathrm{SI}}/H_{\mathrm{SI}}$ is then expected to lie in the range [-1,1]. The effects of a finite demagnetization factor, D, may be accounted for by calculating the corrected value

$$\chi = \frac{\chi_{\mathrm{eff}}}{1 - D\chi_{\mathrm{eff}}}. \tag{3.2}$$

Setting $\chi = -1$ in Eq. (3.2) (as is expected in the Meissner phase of a superconductor), leads to an expression for D:

$$D = \frac{1 + \chi_{\text{eff}}}{\chi_{\text{eff}}}, \tag{3.3}$$

where χ_{eff} is the measured gradient of the initial magnetization against field.

3.2.2 Vibrating Sample Magnetometry

Measurements of magnetization as a function of field were performed using an Oxford Instruments Vibrating Sample Magnetometer (VSM). A drawback of SQUID magnetometry is that the sample must be moved through the pick-up coils after each temperature and field has been stabilized, such that the magnetization does not change appreciably over the course of the measurement. This can make measurements of magnetization as a function of field time-consuming, as the magnetic field must be stabilized at each value before measuring the magnetization. Use of a VSM overcomes this, by holding the sample in a fixed position between two pick-up coils. An oscillator is used to stimulate vertical motion of the sample through a small distance within the coils, with a typical frequency of 60 Hz. The change of flux due to the motion of the magnetized sample induces a voltage in the coils, which can be converted into a magnetization based on calibration measurements performed with a sample of known susceptibility and mass. The VSM used in this work can apply magnetic fields up to 12 T, and operates between temperatures of 300 K and 1.5 K with the aid of a Rootes pump.

3.3 Resistivity

Resistivity was measured using a Quantum Design Physical Properties Measurement System (PPMS), with the alternating-current transport (ACT) option installed. The system consists of a sample probe mounted in a large helium bath, surrounded by a nitrogen jacket. A temperature range between 1.8 K and 400 K was attainable, and a magnetic induction up to 9 T could also be applied.

The four-terminal method was used to make AC transport measurements. As depicted in Fig. 3.3, two outer wires are used to supply a current to a sample, and two separate inner wires are used to determine the potential difference across the sample. The advantage of this method is that the voltage leads draw very little current, which means that the resistance of the leads and the contacts can be ignored. This allows

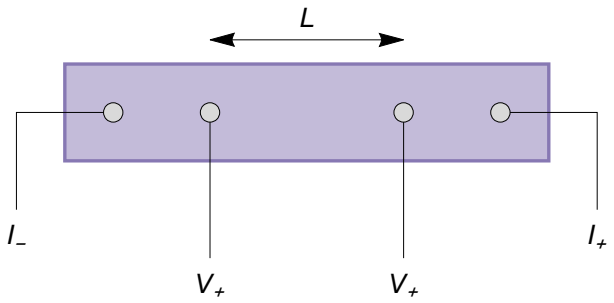

Fig. 3.3 Schematic diagram of a sample configured for a four-probe resistivity measurement, where L is the distance between the two voltage wires.

very accurate values for the voltage, V, developed across the sample in response to an input current, I, to be determined. The resistivity, ρ is then calculated using the equation

$$\rho = \frac{VA}{IL}. \tag{3.4}$$

Here, A is the cross-sectional area of the sample, and L is the separation of the voltage wire contacts. These values are measured using Vernier callipers before preparing the sample for ACT measurements.

Typically, samples were cut into bar shapes with a uniform cross-sectional area, and four silver wires 0.05 mm in diameter were attached using DuPont 4929N silver paste. The current leads generate an electric field over the length of the bar shaped sample, and so it is necessary to attach the voltage wires in line with the current wires to properly measure the associated potential difference. It is also important that the current and voltage wires all have distinct contact points, otherwise contact resistance is no longer negated and can affect the voltage measurement. The wired sample was then affixed to a sample puck using GE varnish, and the wires were soldered to the appropriate connectors. The puck was then installed in the sample chamber using a loading rod.

3.4 Heat capacity

Heat capacity measurements were performed using thermal-relaxation calorimetry using a Quantum Design PPMS. Temperatures as low as 0.4 K were attainable using a ^{3}He insert, and measurements were performed in a magnetic induction of up to 9 T. Samples were prepared with a polished face, which was then mounted on a sapphire sample stage (chosen for its high thermal conductivity) using Apiezon N

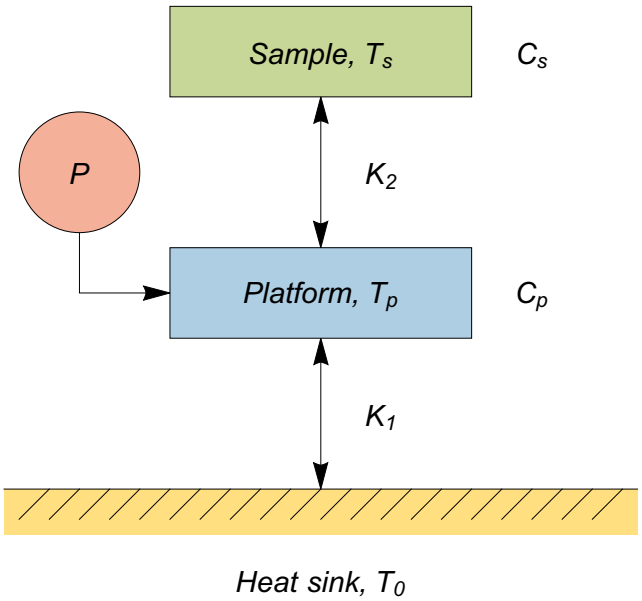

Fig. 3.4 Heat flow diagram of the heat capacity setup. The heater provides a power P to the sample platform, and the subsequent evolution of the platform temperature is monitored. Ideally, the sample has a strong thermal coupling to the platform, such that $T_p \approx T_s$.

or H grease to ensure good thermal contact. The sample stage has a heater and thermometer attached to the underside, and is suspended on the sample puck by wires attached to a copper heat-sink that is held at a constant temperature. As well as providing electrical connection for the puck components, the wires allow heat to conduct between the heat sink and the isolated sample stage.

The heat-flow diagram for the measurement is shown in Fig. 3.4. Here we denote the unknown heat capacity of the sample by C_s and the combined heat capacity of the sample mount, including the thermal grease, as an addenda heat capacity C_a. The thermal conductivity between sample and platform is K_2, and the thermal conductivity between platform and heat sink is K_1. Also, we denote the temperatures of the heat sink, platform, and sample as T_0, T_p, and T_s, respectively. If there is very good thermal conductivity between the sample and the platform (i.e. $K_2 \gg K_1$), then $T_\mathrm{p} \approx T_\mathrm{s}$, and the heat-balance equation for the system is [40]

$$P = (C_\mathrm{a} + C_\mathrm{s})\frac{dT_\mathrm{p}}{dt} + K_1(T_\mathrm{p} - T_0), \tag{3.5}$$

where P is the power of the heater. Upon applying a power to the heater, the platform heats up by an amount $\Delta T = P/K_1$. Turning off the heater then allows the sample and platform to cool to the heat sink temperature T_0, following a simple exponential

relaxation of the form

$$T_{\mathrm{p}}(t) = T_0 + \Delta T \exp(-t/\tau), \tag{3.6}$$

where the time constant is given by

$$\tau = (C_{\mathrm{a}} + C_{\mathrm{s}})/K_1. \tag{3.7}$$

A measurement proceeds by initially applying power to the heater. Measuring the subsequent thermal relaxation thus allows an exponential model to be fitted, and the parameter τ to be measured. Thus, the heat capacity of the sample and addenda can be determined using equation 3.7. Measurements of C_{a} are usually made before attaching the sample to the platform, and thus two full temperature sweeps are required in order to determine first the temperature dependence of C_{a}, and then C_{s}. Also, generally the coupling between the sample and the platform is not 100%, which leads to a breakdown of the assumption that $T_{\mathrm{p}} \approx T_{\mathrm{s}}$. In this situation, the decay profile of the temperature is the sum of two exponentials of the form Eq. 3.6, with two relaxation rates τ_1 and τ_2. It is common that one of the relaxation rates (generally taken as τ_2) is much faster than the other, and corresponds to thermal relaxation between the platform and the rest of the sample puck. The software uses the addenda measurements in order to first determine C_{a} and K_1, and can thus calculate the desired parameter C_{s} (see Ref. [41] for further details).

It is important to note that this method is most effective if the relative change in temperature $\Delta T/T$ is very small, such that the temperature dependence of the parameters C_{a} and C_{s} can be ignored over the time of the measurement. This means that measuring heat capacities close to critical points, such as near the superconducting transition, can be challenging, as the heat capacities tend to have a strong temperature dependence in the vicinity of the critical temperature.

3.5 Structural determination

The atoms in solid materials typically arrange themselves as ordered structures, which may have a variety of different symmetry properties. The classical model is that of a crystallographic lattice of points, of which to each a basis set of atoms is affixed. The entire crystal structure can be constructed by identifying the basic building block, called the *unit cell*, and determining the symmetry of the crystal lattice. Crystal structures have long range order, and are thus well suited to being studied using diffraction techniques.

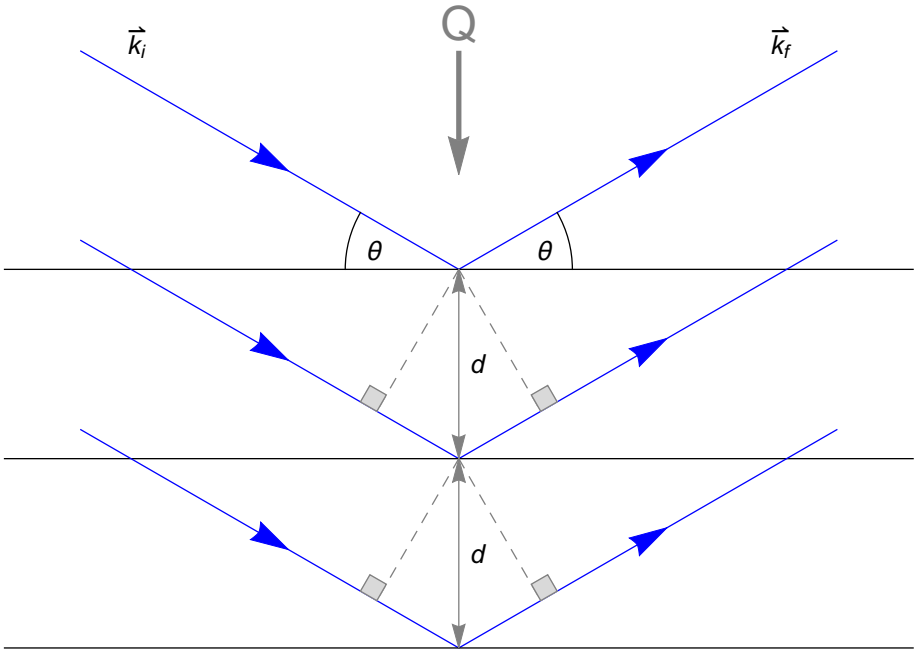

Fig. 3.5 Bragg's elementary derivation of the scattering law for reflections from uniformly spaced layers (Eq. 3.10).

The structural characteristics of samples were probed using X-ray powder diffraction (XRD). The scattering of X-rays or neutrons from uniformly spaced planes of atoms can be modelled as specular reflections from an array of equally spaced parallel lines. The geometric arrangement is shown in Fig. 3.5. It can be shown that if the inter-planar spacing is d and the scattering angle is 2θ, then the path distance, ΔL, for rays reflecting from adjacent planes is

$$\Delta L = 2d \sin\theta. \tag{3.8}$$

In order to observe a peak, we require that the outgoing waves all interfere constructively. This only occurs if the path difference is equal to an integer number n of whole wavelengths, λ, such that

$$\Delta L = n\lambda. \tag{3.9}$$

Combining Eqs. (3.8) and (3.9) leads to the Bragg diffraction condition:

$$n\lambda = 2d \sin\theta, \tag{3.10}$$

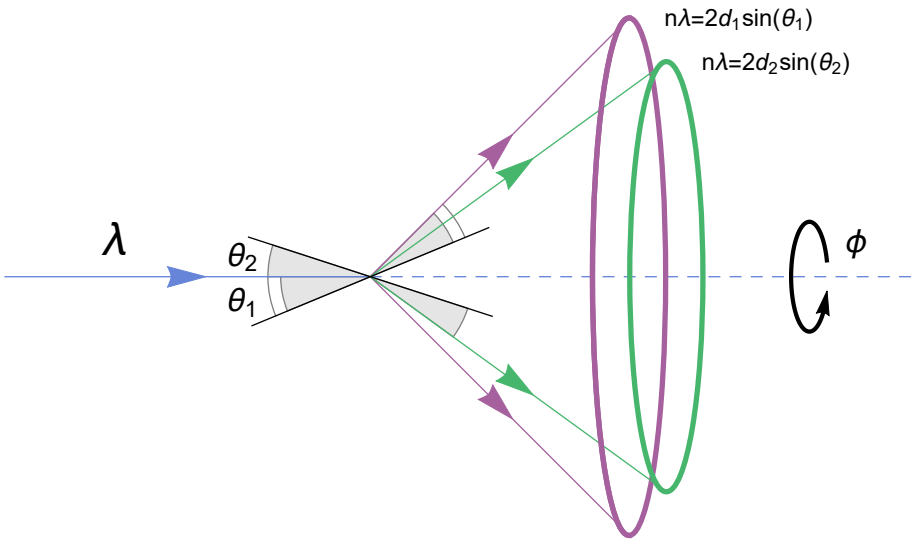

Fig. 3.6 Debye-Scherrer cones for two particular lattice spacings, d_1 and d_2, in a powdered sample.

which is the principle underlying all scattering techniques. It states that if we measure the scattering intensity over a range of scattering angles for radiation of a known wavelength, we can infer the inter-planar spacing in the atomic structure of a material.

The analysis above assumes a single perfectly ordered array of atomic planes, and leads to sharp points in space at the diffraction angles which satisfy Eq. (3.10). In general, growth of a perfect single crystal is one of the primary hurdles in condensed matter science, and thus it is fortuitous that the diffraction technique of structural analysis can be equally well applied to powdered samples. These samples consist of very many crystallites, typically a few microns in size, all of which are expected to be randomly oriented. If the crystallites are sufficiently randomly aligned, then illuminating the sample with radiation of wavelength λ will mean that, purely by chance, the diffraction condition will be met for a proportion of all the different d spacings present in the structure.

As an example, consider two inter-planar distances in an arbitrary crystal structure, say d_1 and d_2 (the situation is depicted in Fig. 3.6). For the first d-spacing d_1, a proportion of the crystallites will be correctly aligned with respect to the incident beam at an angle of θ_1, such that the diffraction condition is met and the scattered radiation interferes constructively. The same situation will occur for a different d-spacing, d_2 - crystallites aligned at the correct angle θ_2 satisfying the diffraction condition will scatter the radiation constructively. The scattering is azimuthally symmetric about the direction of the incident beam, that is, the diffraction condition is met by all planes which are angled azimuthally at $\theta_{1,2}$ with the incident beam.

This leads to conical trajectories of equal scattering known as a Debye-Scherrer cone.

In a typical powder-XRD instrument, the detectors are moved to different values of the scattering angle 2θ along a constant azimuthal angle ϕ. The Debye-Scherrer cones from each lattice spacing are therefore crossed by the detector as it moves between scattering angles, and the intensity of the scattered radiation is collected for a set duration at each position. This intensity as a function of scattering angle data can then be compared with the expected theoretical XRD spectra for a particular sample. All the samples produced in this work were polycrystalline in nature, and structural determination was carried out using a Panalytical X-Pert Pro diffractometer. Information about the expected unit cell symmetry was used, together with the TOPAS software, to refine the lattice parameters of the as-synthesized samples, and compared with published values in order to assess the sample quality [42]. X-ray diffraction was also used to check the phase purity of the samples, as anomalous peaks in the spectra can indicate the presence of an impurity.

3.6 Muon spin spectroscopy

As discussed in the previous chapter, the superconducting state is intimately linked with magnetic effects. For example, the strongest evidence of a superconducting transition is the observation of perfect diamagnetism as the superconductor expels magnetic field from its interior. This can be determined using a bulk magnetization measurement, such as the SQUID magnetometer introduced in Section 3.2. However, in the vortex state there exists a magnetic texturing, which is modulated over the range of a few hundred nanometres. Bulk techniques are ill-suited to working out the subtleties of this magnetic structure, and it is for this reason that we turn to a local probe of magnetism. Muon Spin Rotation and Relaxation (collectively μSR) involves implanting spin-polarized positive muons into materials, and observing the subsequent evolution of the spin vector.

The positive muon is a lepton, and has a mass roughly $1/9$ that of the proton. In fact, for the purposes of μSR, the positive muon is best thought of as behaving like a 'light proton'. Its positive charge means that upon implantation in a given sample, it may sit at interstitial positions in the crystal structure, in accordance with the electrostatics of the local atomic neighbourhood [1]. This leads to another useful

[1] Another possibility is the formation of an exotic bound state with an electron called 'Muonium'. The field of muon chemistry is devoted to investigating the interaction of Muonium with matter, however this aspect of μSR will not form the focus of this thesis.

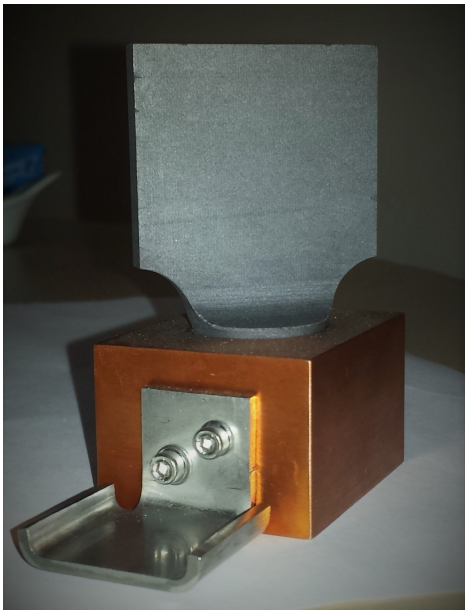

Fig. 3.7 One of the graphite muon targets used at ISIS.

property of the positive muon - its lifetime is independent of the material into which it is implanted, unlike the negative muon which typically is captured by the nuclei of the local atoms, and therefore has a material dependent lifetime [2]. Lastly, the positive muon is a fermion, which means that it has a half-integer spin, and thus is sensitive to magnetic fields. The spin vector precesses when placed in a magnetic field, with a gyromagnetic ratio $\gamma_\mu = 2\pi \cdot 135.5\,\mathrm{MHz\,T^{-1}}$. This means that if we can measure the precession rate of the spin vector, we can determine the perpendicular component of magnetic field experienced in the locality of the muon.

3.6.1 Muon production

The muons used in this work were produced at the ISIS Pulsed Neutron and Muon source in Didcot, Oxfordshire, and studied using instruments at the European Muon Facility. At ISIS, protons are accelerated using a synchrotron to energies of 800 MeV, corresponding to a speed of 0.86 c. The proton beam is separated into two bunches before being delivered to the muon and neutron targets. Each proton extraction delivers 4 μC of protons in two pulses each with a full width at half maxima (FWHM) of 70 ns. The synchrotron operates at a frequency of 50 Hz, meaning that an average current of 200 μA is delivered to the targets. The double pulses are distributed between target station 1 and 2 in the ratio 4:1.

[2]The material dependent lifetime has been harnessed recently as a method of depth sensitive compositional analysis, see for example Ref. [8]

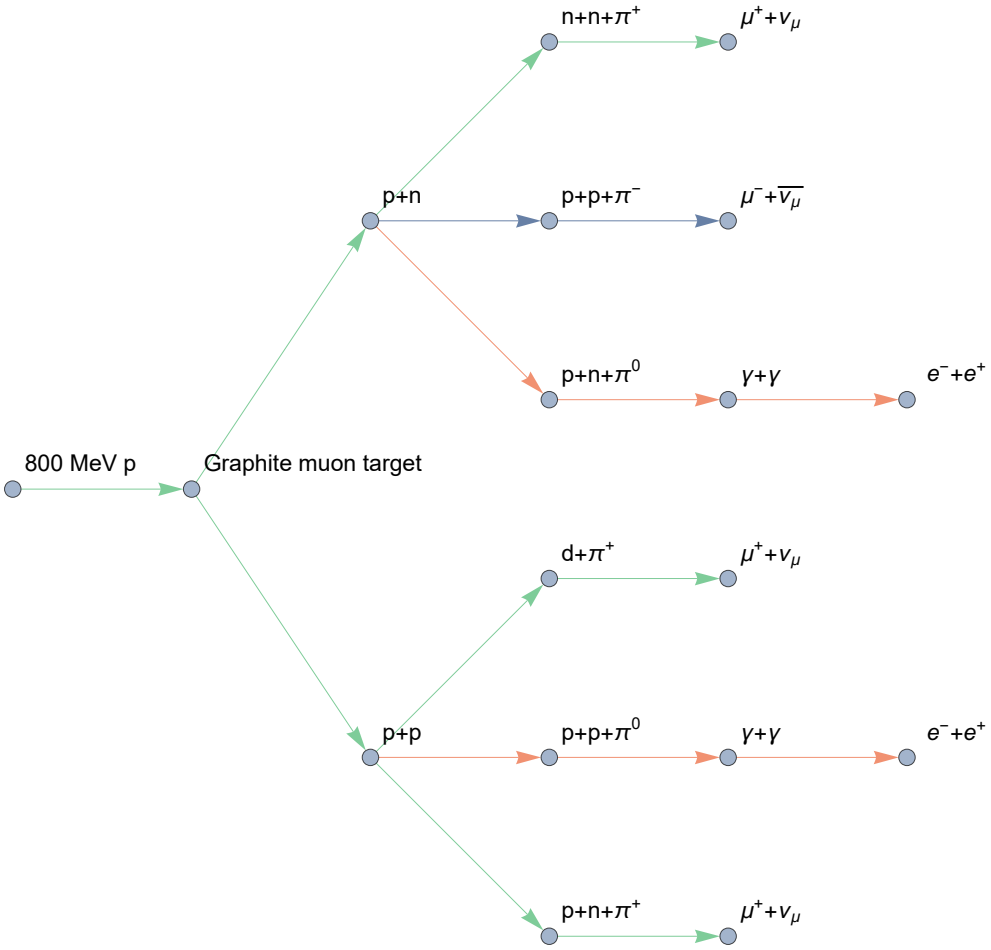

Fig. 3.8 Potential decay modes that occur when high energy protons strike the muon target. The green lines lead to μ^+ production, whereas the red lines lead to contaminant e^+ in the muon beam. The dark lines lead to the creation of μ^-, which are either captured by the carbon nuclei of the target, or directed out of the beam-line by magnets.

The muon target is located in target station 1, upstream of the main neutron target. The target is made of graphite (see Fig. 3.7), and absorbs about 5% of the proton current. The ensuing high energy interactions between the protons and the carbon nuclei result in a shower of pions - a few of the most common decay modes are shown in Fig. 3.8. Positive pions rapidly decay with an average lifetime of 26 ns into a muon and a neutrino:

$$\pi^+ \rightarrow \mu^+ + \nu_\mu. \tag{3.11}$$

As this is a two body decay, conservation of linear momentum requires that the muon and neutrino are emitted with equal and opposite momenta in the rest frame of the pion. Pions that stop at the surface of the graphite target decay into muons with an energy of 4.1 MeV. It is these surface muons that are used for the experiments at the European Muon Facility. The π^+ is a spin-zero boson, whereas the μ^+ and ν_μ are both spin-half fermions. Therefore the spin vectors of these decay particles must be anti-aligned in order to conserve angular momentum. Parity violation in the weak interaction requires that the spin vector of neutrinos is always anti-parallel to its momentum. Therefore the spin vector of the muons must also be anti-parallel to the momentum. As the pions decay isotropically in space, the surface muons emitted in any chosen direction must be 100% spin polarized. This remarkable fact is one of the key reasons why the μSR technique works.

3.6.2 Muon transport to the experiments

Surface muons from the target are directed to the μSR instruments through an array of deflectors using magnetic and electric fields. Quadrupole magnets are used in doublets or triplets to focus the beam in the x, y, and z directions, and dipole bending magnets select muons of the appropriate momentum bite. A further important step is stripping contaminant particles from the muon beam - typically these are present due to the decay of neutral pions into photons, and subsequent pair production of electrons and positrons. A cross-field electrostatic separator serves this purpose, by passing particles through a region with a vertical electric field, and a magnetic field perpendicular to the E-field and the beam direction. By balancing the voltage and magnetic field appropriately, contaminant positrons are vertically deflected from the beam, whilst the forces on muons with the appropriate momentum are balanced, and they are delivered to the experiment unheeded. The separator introduces a 7° rotation of the muon spin vector, however as this is applied coherently to all the muons in the pulse the overall spin polarization is maintained.

The muons arrive at the instruments as double pulses, each with a full width at half maxima (FWHM) of 80 ns, reflecting the pulsed nature of the proton current from which they were borne.[3] The European Muon Facility consists of three instruments - EMU, MuSR, and HiFi [43–45]. The double pulse of muons arriving from the target is distributed between these instruments using an electrostatic kicker, which consists of three electrodes: a grounded outer pair and a central anode [46]. Before the first pulse of muons arrives, the potential on the central anode is powered to 32 kV. This has the effect of deflecting the first pulse of muons equally to the left and right by an angle of approximately 4°. Each half of the deflected muon pulse arrives in separate septum magnets, which steer each pulse into the EMU and HiFi instruments. The second muon pulse arrives 330 ns after the first, in which time the central anode must power down from 32 kV to neutral. This ensures that the second pulse experiences no deflection, and the entire bunch of muons is delivered to the MuSR spectrometer.

3.6.3 Muon implantation

Muons striking matter lose kinetic energy through ionisation of atoms, scattering of electrons, and Muonium formation, ideally coming to rest at interstitial positions in the crystal structure. This thermalisation process occurs very rapidly, over a time-scale not exceeding a few nanoseconds, and does not involve magnetic interactions. This means that depolarization effects during the thermalisation process are insignificant, and the muons maintain 100% spin polarization. Once implanted, the local magnetic environment that each muon finds itself located in dictates the subsequent evolution of the spin vector. If the internal field profile is uniform, the muons will retain their polarization over the course of a measurement. The presence of a transverse magnetic field component will cause spin precession, at a frequency given by Eq. (3.14). If there is a significant site-to-site field variation, either temporal or spatial, then the muon ensemble will become depolarized. By monitoring this depolarization and the precession rate, a picture of the internal magnetic field profile in a sample may be constructed.

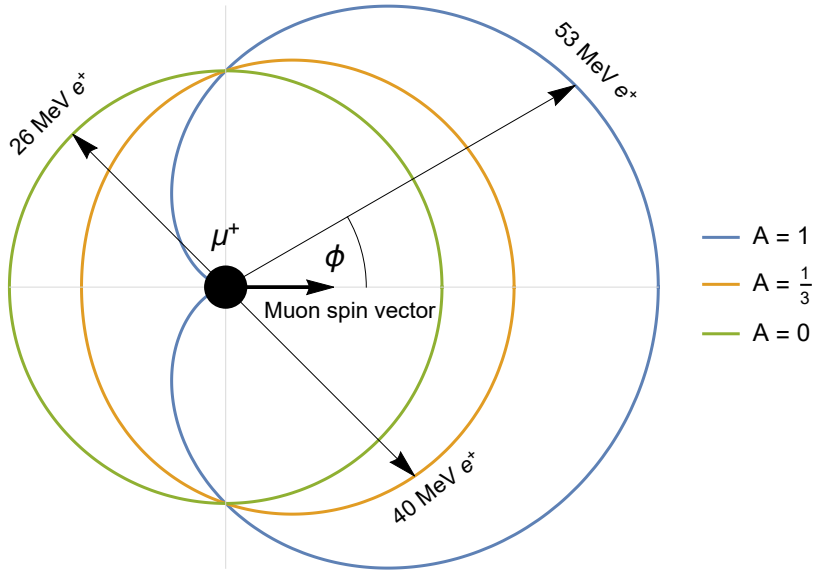

Fig. 3.9 Variation of the angular distribution function (Eq. (3.13)) for different asymmetry parameters, A, corresponding to positrons emitted with different energies.

3.6.4 Asymmetry of the muon decay

The positive muon decays into a positron and two neutrinos with a characteristic lifetime of $\tau_\mu = 2.2\,\mu s$:

$$\mu^+ \rightarrow e^+ + \nu_e + \bar{\nu}_\mu. \tag{3.12}$$

As this is a three body decay, there is a spectrum of different energies and momenta with which the decay positron can be emitted. The decay positron is emitted preferentially in the direction of the muon spin vector, with an angular distribution given by the probability function

$$P(\phi) \propto 1 + A\cos(\phi), \tag{3.13}$$

where ϕ is the angle between the muon spin vector and the direction of positron emission. The parameter A defines the asymmetry, and increases monotonically from zero as a function of energy of the emitted positron, with a maximum value of $A = 1$ for the highest energy positrons. Figure. 3.9 shows how the probability function changes as A is varied. If one integrates over all positron energies, the average value turns out to be $A = 1/3$. This baseline value can be increased by filtering out low energy positrons using degrader materials - however this comes at the expense of

[3] Note that this is longer than the proton pulse width of 70 ns. This is because the pulse shape is broadened due to the 26 ns decay lifetime of the pions in the muon target.

count rate. It is therefore possible to determine how the polarization of the muon ensemble evolves over time by counting the decay positrons, as long as the direction in which they are emitted is taken into account. The next section discusses the role of geometry on the type of μSR experiment that can be carried out.

3.6.5 Experimental geometries

In this section we will focus on the MuSR instrument, as this was the main instrument used for the experiments in this thesis. MuSR consists of 64 detectors arranged on two circular arrays, one of which is pictured in Fig. 3.10. The detector arrays are centred around a hollow sample space where the muon beam enters the instrument, into which a cryostat can be mounted. Each detector is formed of a plastic scintillator, light-guide, and photomultiplier tube (PMT). The plastic scintillators are arranged near to the sample space, and it is here that the decay positrons are detected. Scintillation events produce photons that enter the PMTs via the light-guides. These events are amplified in the PMTs producing voltage pulses, which are fed into discriminator electronics. The purpose of this step is to attempt to filter out incorrect detection events, i.e. the voltage must cross a certain expected threshold in order to be considered a positron detection from muon decay. The electronics are also synchronized to the ISIS proton pulse, ensuring that events collected between pulses are discarded.

In the MuSR instrument, muons arrive with their spin vector initially anti-parallel to the momentum vector. Directions are labelled as one would label the sides of a cube, with a 'beam's eye view' naming convention. We therefore are able to sort directions into three sets of opposing pairs: U (Up), D (Down), F (Forward), B (Backward), L (Left), and R (Right). The coordinate system and a schematic diagram of the relative directions is displayed in Fig. 3.11. Thus, the initial spin polarization vector points towards the B direction. These positions are important to consider for data analysis, as data from individual detectors is grouped into these directions and summed together in order to calculate the asymmetry spectrum (see Sec. 3.6.6 for details).

The primary magnet on MuSR is a water-cooled, conventional electromagnet, which is able to produce a magnetic induction of 0.25 T. MuSR is also fitted with an active zero-field system, which consists of three pairs of compensation coils aligned in the x, y, and z directions. The aim of these coils is to cancel out stray fields from other sources, such as the Earth and nearby instruments, in order to achieve a true zero-field at the sample position. This is especially important for measuring very

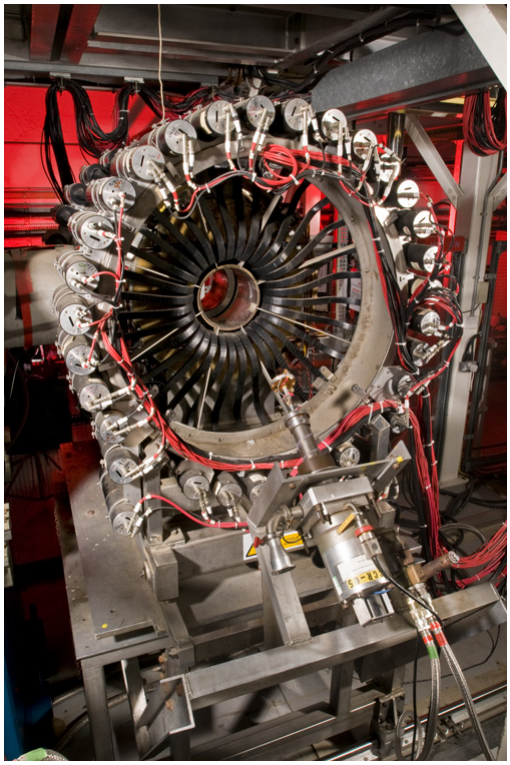

Fig. 3.10 One half of the MuSR instrument at ISIS. The sample space can be seen through the central hole, and a cryostat is craned in from above. The black spokes are the light-guides, leading from the plastic scintillation material close to the sample space to the PMTs arranged on the circular array.

weak magnetic effects, such as the presence of spin-triplet Cooper pairs. Using this system, MuSR is able to achieve a zero-field that is stable to within 1 µT. An advantage of the MuSR spectrometer is its ability to be rotated through 90°. This changes whether the primary magnetic field is applied parallel or perpendicular to the initial spin polarization direction. In zero field, this allows measurements to be made in both directions, which can help distinguish if small signals are intrinsic to the sample, or are caused by stray fields. Experiments are typically carried out in one of two geometries, which are discussed in the following sections.

Transverse field µSR

Muon spin *rotation* experiments align the magnetic field perpendicular to the initial spin polarization direction. A schematic diagram of the setup is displayed in Fig. 3.12 (a), with the appropriate detector groupings labelled. This transverse field (TF) causes

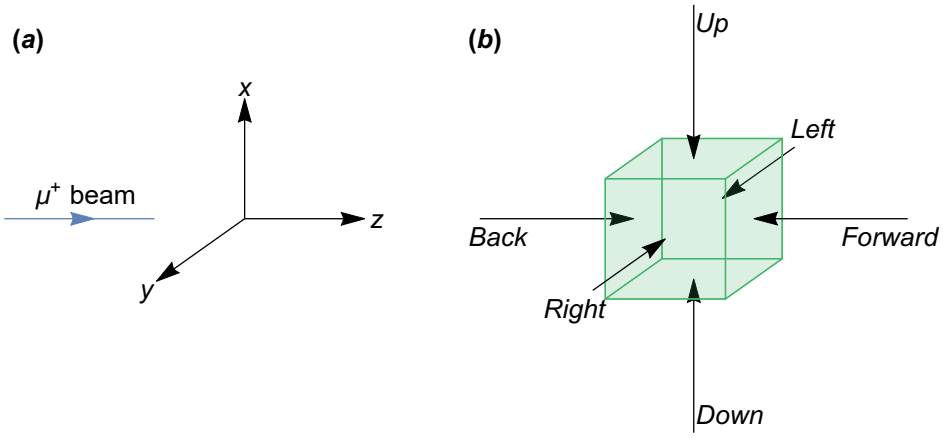

Fig. 3.11 Geometry for a typical μSR experiment: (a) Defining the coordinate system, where the initial muon beam points along the z axis, and the initial polarization direction is anti-parallel to z. (b) 'Beam's eye view' directional naming convention, used when grouping detectors for data analysis.

the muon spins to precess in the $x-z$ plane at the Larmor precession frequency,

$$\omega = \gamma_\mu |\vec{B}|, \tag{3.14}$$

where $\vec{B} = \mu_0 \vec{H}$ is the magnetic induction in Tesla. In this case, the polarization is monitored in the x and z directions, and the detectors are grouped in the Back, Forward, Up, and Down (BUFD) directions to reflect this.

Longitudinal and zero-field µSR

Rotating MuSR by 90° allows a longitudinal field (LF) μSR experiment to be carried out, in which the magnetic field is aligned anti-parallel to the direction of the initial spin polarization. Muon spin *relaxation* experiments (also commonly called zero-field (ZF) μSR) are conducted in the same geometry as LF-μSR, however no field is applied and the muon depolarization is due solely to the internal magnetism of the sample. For both of these situations, the polarization evolution only needs to be monitored along the same direction as the initial spin vector - therefore the detectors are grouped into the F and B directions as depicted in Fig. 3.12(b).

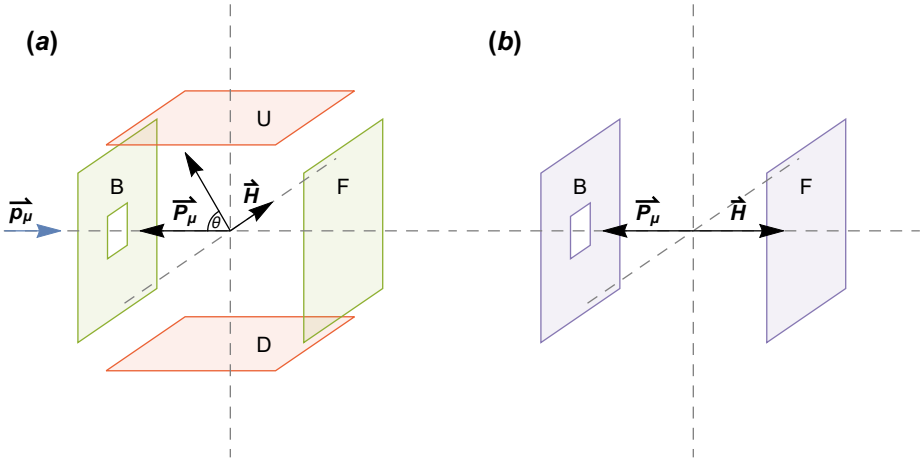

Fig. 3.12 Detector groupings for μSR experiments: (a) TF-μSR. The muon spin initially points towards the B detector, and a magnetic field is applied along the y axis. The spin vector precesses in the $x-z$ plane, and the detectors are grouped into the BUFD directions, where the BF pair monitors the spin polarization in the z direction, and the UD pair monitors the polarization in the x direction. (b) LF and ZF-μSR. The magnetic field direction is along the z axis, in which case no precession is expected. Only the z component of the spin polarization vector needs to be monitored due to symmetry, which requires only BF detector groupings. Note that ZF-μSRis the limiting case where $\vec{H} = 0$.

3.6.6 Measuring the asymmetry spectrum

The general procedure for extracting the time-differential asymmetry of the muon ensemble requires grouping detectors into the appropriate directions (BF for LF geometry; BFUD for TF geometry), summing the counting histograms from the detectors in each group, and then calculating the asymmetry between opposing detector groups. In the following example we will consider the B and F groups, however the mathematics is similar for the U and D directions.

As described previously, the direction of the initial spin polarization is always pointing towards the backwards direction. The number of counts $N_{B,F}$ detected in the B and F detectors will be given in general by

$$N_B = N_0 \exp\left(-\frac{t}{\tau_\mu}\right)(1 + A_0 G_z(t)) \tag{3.15a}$$

$$\alpha N_F = N_0 \exp\left(-\frac{t}{\tau_\mu}\right)(1 - A_0 G_z(t)) \tag{3.15b}$$

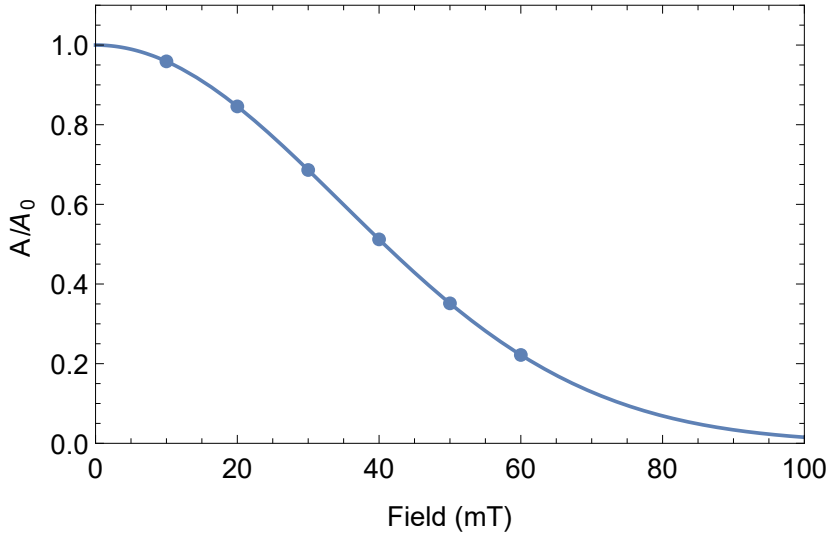

Fig. 3.13 Simulated decay of the maximum asymmetry as a function of applied transverse field for TF-μSR. The points highlight commonly used transverse fields on the MuSR instrument.

Here α measures the relative efficiencies of the F and B detectors, $A_0 = A(t=0)$ is the initial asymmetry (which can be assumed to be the same for each detector), N_0 is a normalization constant, and $G_z(t)$ is the (unknown) time evolution of the muon polarization along the z axis. It is the goal of any μSR experiment to determine the form of $G_z(t)$, as it is this function that contains information about the magnetic environment in the sample being studied. The exponential term simply describes the decay of muons into positrons with a lifetime of $\tau_\mu = 2.2\,\mu$s, and the final term in brackets comes from Eq. (3.13) with $\phi = 0$ and $\phi = \pi$ for the B and F detectors, respectively. The experimental asymmetry $A(t)$ is then calculated by combining Eqs. (3.15):

$$A(t) = A_0 G_z(t) = \frac{N_B(t) - \alpha N_F(t)}{N_B(t) + \alpha N_F(t)}. \tag{3.16}$$

The relative efficiency parameter, α, is generally sample position and environment dependent, and must be measured independently for each experiment by applying a weak transverse field - the correct value will cause the calculated asymmetry spectra to oscillate symmetrically about the time axis. Some simulated asymmetry spectra are presented in Sec. 3.6.8, as well as a discussion about the physical interpretation of the different functional forms of $G_z(t)$.

Transverse-field asymmetry spectra

A subtlety arises when analysing TF data that is not important in the LF geometry. As the muon spin precesses about the magnetic field vector, the oscillation detected in each individual detector will differ by some phase difference from all of the other detectors. Now, when it comes to grouping the detectors into U, D, B, and F groups, the histograms from each individual detector are summed. If the phase difference is not accounted for, then this process has the effect of reducing the total asymmetry of the signal, which is not desirable - we are effectively throwing away a portion of the data by naively summing the histograms.

One method of reducing this error is to make the detector groupings smaller. Rather than having 4 groups of 16 detectors each, it is possible to segment the detectors into 8 groups of 8 detectors, or 16 groups of 4 detectors. This reduces the phase problem, however, it does make data analysis much harder, as now 8 or 16 separate datasets must be simultaneously processed in order to find the polarization function $G_z(t)$.

In this thesis, a different method was adopted, which is discussed in detail in Ref. [47]. By considering the phases of each individual detector, the data from all of the histograms can be 'squashed' into two histograms with orthogonal phases. The phases are simply related to the position that each detector is located on the circular array. The time-series resulting from the two orthogonal histograms are then simultaneously fitted, in order to extract the polarization function $G_z(t)$. This method has the advantage of not throwing away any data, and therefore not artificially reducing the initial asymmetry.

At the time of these experiments, it was possible to apply a magnetic field of up to 0.25 T using the main MuSR electromagnet, however this is only feasible for experimental work in LF geometry. The maximum TF that may be applied is limited by the finite size of the muon pulse width. To see this, consider that the pulse has a FWHM of 80 ns. Muons at the forefront of the pulse will have entered the sample, thermalised, and settled at interstitial positions ready to sample the internal magnetic field before the muons at the back-end of the pulse have even entered the sample space. In the presence of a transverse magnetic field, the spins of these initial muons begin to precess immediately, which leads to some initial depolarization of the muon ensemble, and thus to a loss of initial asymmetry. Mathematically, this is a convolution of the ideal signal, Eq. (3.15) and the muon pulse shape. For a Gaussian pulse shape with a width $\tau \approx FWHM/2.35$, the decay of the asymmetry

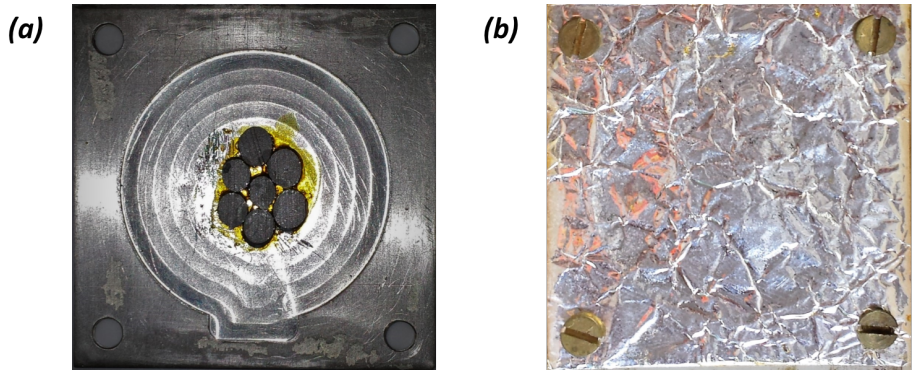

Fig. 3.14 (a) A sample of $Lu_3Os_4Ge_{13}$ mounted on a silver sample holder using GE varnish. (b) The sample is covered with a thin layer of silver foil, which improves thermal stability and acts as an additional heat shield.

as a function of applied field $B = \omega/\gamma_\mu$ is given by the equation

$$A/A_0 = e^{-\frac{1}{2}\gamma_\mu^2\tau^2B^2}, \tag{3.17}$$

which is plotted in Fig. 3.13 for the muon pulse width $FWHM = 80\,\text{ns}$.

3.6.7 Sample environment

Samples are mounted on high purity silver sample holders using GE varnish, as shown in Fig. 3.14. Silver is used as it has a very small nuclear moment, which results in a non-depolarizing background signal that may be easily accounted for during data processing.[4] The sample holder is typically mounted in one of a variety of different cryostats that are available on MuSR. Temperatures as low as 20 mK are attainable using dilution refrigerators, and a standard He^4 cryostat is available for work requiring temperatures no lower than 1.8 K. Commonly used in this thesis was a sorbtion cryostat, which operates effectively for temperatures in the range 350 mK to 50 K.

3.6.8 Polarization functions

Until now, the form of $G_z(t)$ has been largely ignored. We now consider the expected forms of this polarization function for a variety of common internal field distributions. In any system, the local field experienced by a muon originates from the combined

[4] In LF-μSR the silver adds a constant background term to the asymmetry spectra, whereas in TF-μSR muons stopped in silver contribute a non-decaying oscillation at a frequency corresponding to the applied field.

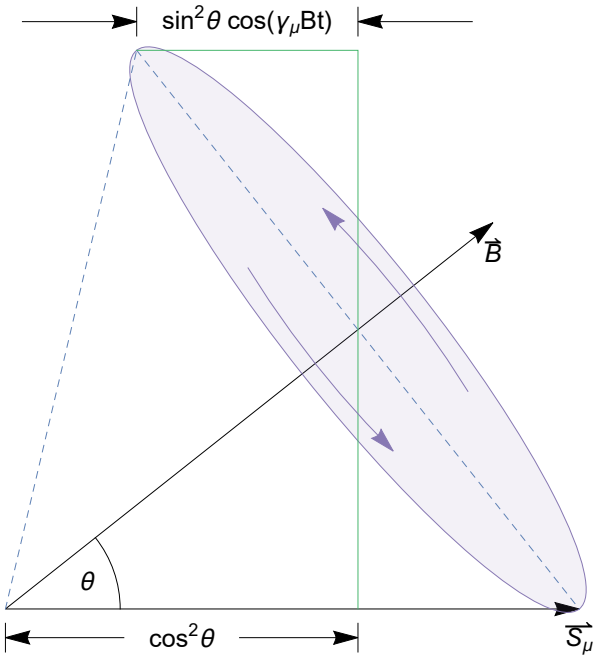

Fig. 3.15 Muon spin precession around the internal magnetic induction vector $\vec{B}$. The muon spin $\vec{S}_\mu$ is initially aligned along the z direction, and θ is the angle between $\vec{B}$ and $\vec{S}_\mu$. The projection of the spin vector on the z axis is thus formed of a time-independent part proportional to $\cos^2\theta$, and a time-dependent component proportional to $\sin^2\theta$. The time dependence comes from the precession of the spin vector about the magnetic field vector at the Larmor frequency, $\gamma_\mu B$.

dipolar interactions of nearby nuclear and electronic spins, and the external magnetic field. Many of the equations in this section are described in Ref. [48].

Randomly oriented static field, unique $|\vec{B}|$

We first consider a system where each muon experiences a unique magnitude of the local magnetic field, however each field vector is randomly oriented. The vectors are also constrained to be static with respect to the muon lifetime, which means that their fluctuation rate is much lower than the muon decay rate. Consider the evolution of the spin polarization $\vec{S}_\mu$ of a single muon in such a local field, $\vec{B}$, making an angle θ with the spin vector as depicted in Fig. 3.15. The spin vector is co-aligned with the z axis, and the muon spin precesses around $\vec{B}$ at the Larmor precession frequency. The z component of the muon spin as a function of time, $\sigma_z(t)$, is given by

$$\sigma_z(t) = \cos^2\theta + \sin^2\theta\cos(\gamma_\mu|\vec{B}|t). \tag{3.18}$$

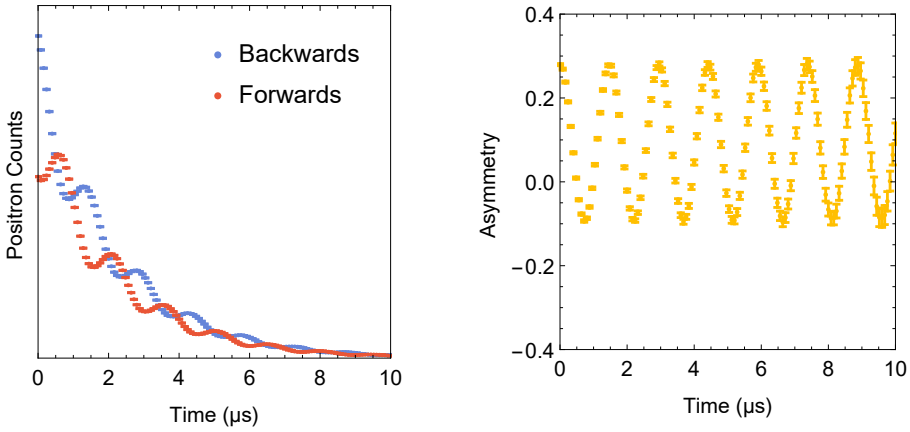

Fig. 3.16 Simulated positron counts and corresponding asymmetry spectra, where Eq. (3.19) is the polarization function. Simulation parameters: $N_0 = 10^6$, $A_0 = 0.28$, $\alpha = 1$, $B = 5\,\mathrm{mT}$.

.

The average value of the ensemble polarization is found by spatially averaging Eq. (3.18) over all solid angles, $d\Omega = \sin\theta d\theta d\phi$. Thus the precession function is given by

$$\begin{aligned} G_z(t) &= \frac{1}{4\pi}\int_0^{\pi}\int_0^{2\pi} \sigma_z(t)\sin\theta d\theta d\phi \\ &= \frac{1}{3} + \frac{2}{3}\cos(\gamma_\mu |\vec{B}|t). \end{aligned} \tag{3.19}$$

A simulated positron counting spectrum with the corresponding asymmetry spectrum are presented in Fig. 3.16. Notice that this polarization function is not symmetric about $A = 0$. This is due to the $1/3$ component in Eq. (3.19), which arises due to the component of the field vectors that are aligned with the initial muon spin polarization direction.

Randomly oriented static field, Gaussian distributed $\vec{B}$

The above argument works for a single magnitude of the magnetic field. However, in a system of randomly oriented nuclear spins, the resulting dipolar field is well modelled as a Gaussian distribution. We model the three components of the magnetic field vector $\vec{B} = (B_x, B_y, B_z)$ as Gaussian distributions, with mean zero and a standard

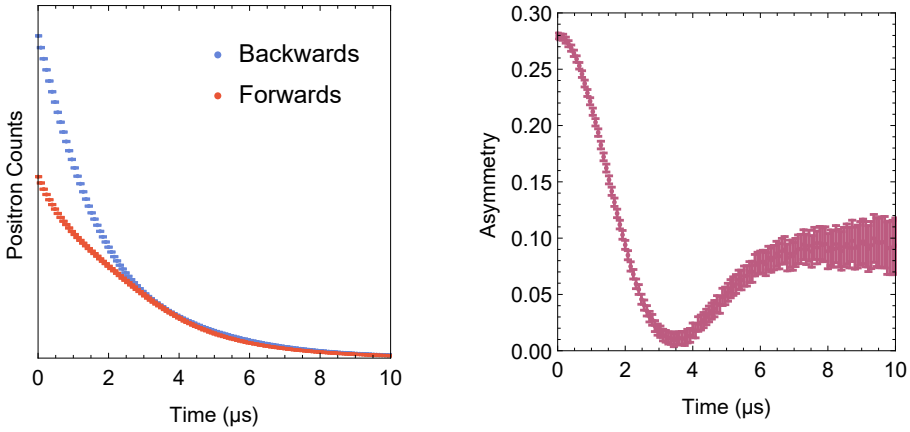

Fig. 3.17 Simulated positron counts and corresponding asymmetry spectra, where Eq. (3.25) is the polarization function. Simulation parameters: $N_0 = 10^6$, $A_0 = 0.28$, $\alpha = 1$, $\Delta = 0.5\,\mu s^{-1}$.

deviation Δ/γ_μ:

$$B_i \sim N\left(0, \frac{\Delta^2}{\gamma_\mu^2}\right). \tag{3.20}$$

The square of the B_i will thus be distributed according to a χ^2 distribution with 1 degree of freedom:

$$B_i^2 \sim \chi^2(1). \tag{3.21}$$

The sum of the B_i^2, which is equal to the magnitude of the vector squared, $|\vec{B}|^2$, is thus distributed according to a χ^2 distribution with three degrees of freedom:

$$|\vec{B}|^2 \sim \chi^2(3). \tag{3.22}$$

Therefore, the local magnetic field strength, $|\vec{B}|$ is distributed according to the χ distribution with three degrees of freedom. After normalizing to ensure the total area is equal to unity, we find that the probability distribution of $|\vec{B}|$ is given by

$$P^{\mathrm{G}}(|\vec{B}|) = \sqrt{\frac{2}{\pi}}\frac{\gamma_\mu^3}{\Delta^3}|\vec{B}|^2 \exp\left(-\frac{\gamma_\mu^2|\vec{B}|^2}{2\Delta^2}\right). \tag{3.23}$$

This distribution has a maximum when

$$|B|_{\max} = \sqrt{2}\frac{\Delta}{\gamma_\mu}, \tag{3.24}$$

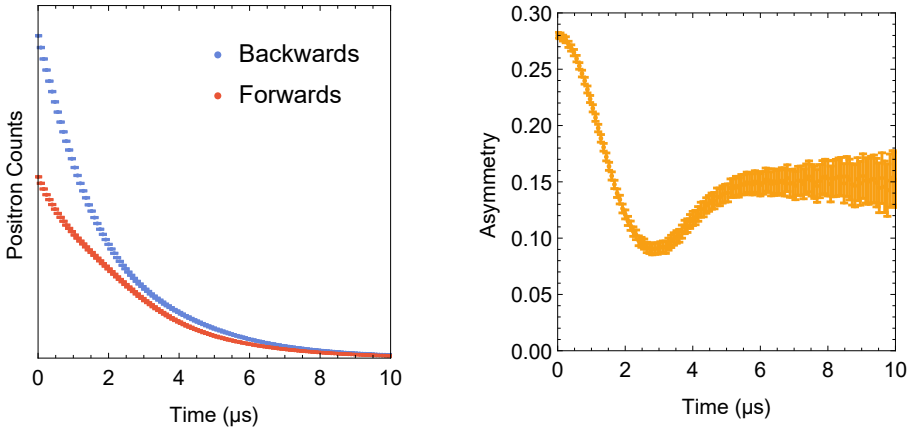

Fig. 3.18 Simulated positron counts and corresponding asymmetry spectra, where Eq. (3.26) is the polarization function. Simulation parameters: $N_0 = 10^6$, $A_0 = 0.28$, $\alpha = 1$, $\Delta = 0.5\,\mu s^{-1}$, $B_L = 0.83\,mT$.

showing that if we can measure Δ then we can estimate the magnitude of the local fields experienced by the muons. The corresponding polarization function for this distribution of magnetic fields is found by integrating the product of Eqs. (3.19) and (3.23) over all field magnitudes, $0 \leq |\vec{B}| \leq \infty$. These are standard integrals, and are readily evaluated to give the Gaussian Kubo-Toyabe polarization function:

$$G_z^{\mathrm{KT}}(t) = \frac{1}{3} + \frac{2}{3}(1-\Delta^2 t^2)\exp\left(-\frac{1}{2}\Delta^2 t^2\right). \tag{3.25}$$

Figure 3.17 was simulated using Eq. (3.25) as the polarization function, with a field width of $\Delta = 0.5\,\mu s^{-1}$. This asymmetry spectrum is characteristic of materials in which the primary contribution to the internal fields is from randomly oriented nuclear dipole moments.

Gaussian distributed $\vec{B}$ with applied longitudinal field

Applying a longitudinal field, B_L, shifts the direction of $\vec{B}$ towards the z axis. This has the effect of boosting the $1/3$ component, and reducing the $2/3$ time dependent component. The full expression for the polarization function is given by [49]

$$G_z^{\mathrm{LF}}(t) = 1 - \left(\frac{2\Delta^2}{\omega_L^2}\right)\left[1 - e^{\left(-\frac{1}{2}\Delta^2 t^2\right)}\cos(\omega_L t)\right] + \left(\frac{2\Delta^4}{\omega_L^3}\right)\int_0^t e^{\left(-\frac{1}{2}\Delta^2\tau^2\right)}\sin(\omega_L\tau)d\tau), \tag{3.26}$$

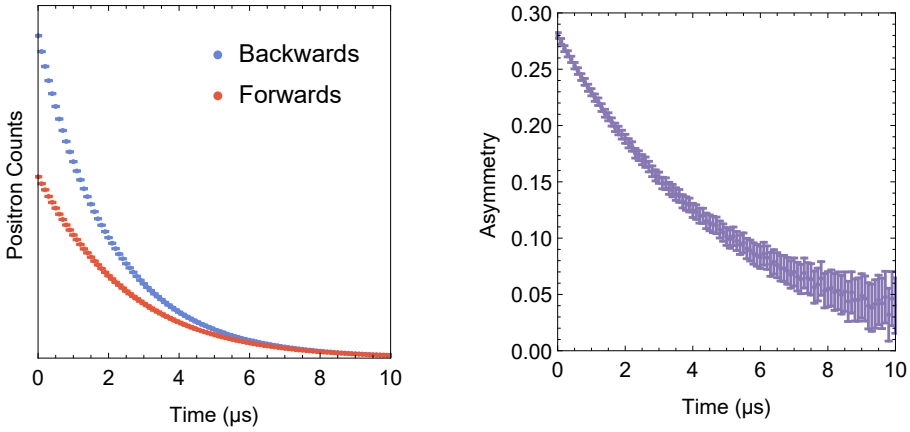

Fig. 3.19 Simulated positron counts and corresponding asymmetry spectra, where Eq. (3.27) is the polarization function. Simulation parameters: $N_0 = 10^6$, $A_0 = 0.28$, $\alpha = 1$, $\Lambda = 0.2\,\mu s^{-1}$.

where $\omega_L = \gamma_\mu B_L$. As the applied field is increased, the '1/3 tail' of the Kubo-Toyabe function becomes more dominant - notice that if $\omega_L \gg \Delta$, the second and third terms of this equation become vanishingly small, and the depolarization function is approximately constant. This suppression of the relaxation component of the depolarization is referred to as 'decoupling', and allows one to estimate the strength of the local fields by varying the applied field B_L. In fact, when $B_L = |B|_{\max}$ (as given by Eq. (3.24)), the '1/3 tail' is expected to have been boosted to a factor of approximately 1/2. Experimentally, this provides an independent method of estimating Δ. The simulation in Fig. 3.18 has been calculated with $\Delta = 0.5\,\mu s^{-1}$ and $B_L = \sqrt{2}\Delta/\gamma_\mu = 0.83$ mT - notice that the asymmetry tail recovers to a value of approximately one-half the initial asymmetry.

Fluctuating spins

If the spins giving rise to the dipolar field are fluctuating on a time scale similar or smaller than that of the muon lifetime, then the muons will experience a time-varying local magnetic field. In the fast fluctuation (FF) limit, where the fluctuation rate ν is much larger than the field width Δ, the fluctuations have the effect of averaging out the local field experienced by the muon ensemble. This 'motional narrowing' of the local field leads to a slower overall relaxation of the spin polarization, which can be modelled by an exponential function:

$$G_z^{\mathrm{FF}}(t) = \exp(-\Lambda t), \tag{3.27}$$

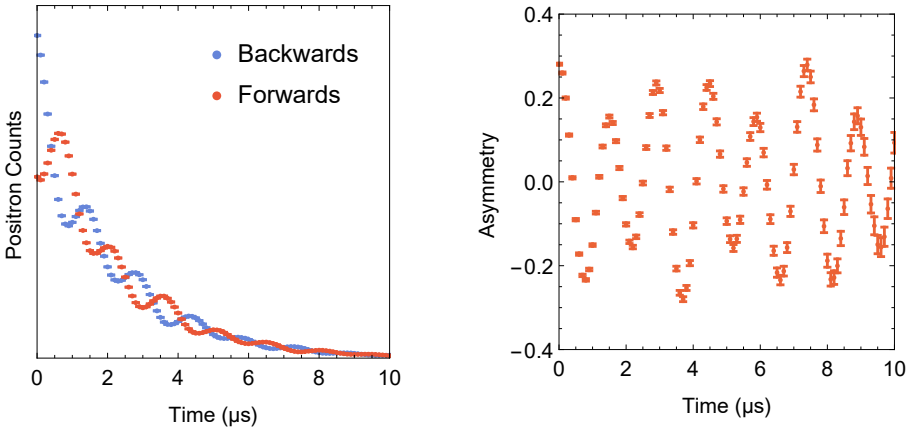

Fig. 3.20 Simulated positron counts and corresponding asymmetry spectra, where Eq. (3.28) is the polarization function. Here there are two unique frequencies, corresponding to two unique fields experienced by implanted muons. Simulation parameters: $N_0 = 10^6$, $A_0 = 0.28$, $\alpha = 1$, $w_1 = 0.75$, $B_1 = 5\,\mathrm{mT}$, $w_2 = 0.25$, $B_2 = 3\,\mathrm{mT}$.

.

where the decay rate $\Lambda = 2\Delta^2/\nu$. Fields originating from electronic moments tend to fluctuate in the fast fluctuation limit, as opposed to nuclear dipole fields, which are static with respect to the muon lifetime. Figure 3.19 was simulated using Eq. (3.27) as the polarization function, with a decay rate $\Lambda = 0.2\,\mu\mathrm{s}^{-1}$.

Short-range magnetic order

Compounds which order magnetically tend to exhibit a distinct magnetic field distribution over the unit cell, the strength and direction of which is dependent on the details of the alignment and interaction type of neighbouring atomic spins. Muons implanted in such a material will precess at one, or several, distinct frequencies, corresponding to the magnitude of the magnetic field at each possible muon implantation position. Thus the polarization function will consist of a sum of n oscillatory functions,

$$G_z^{\mathrm{osc}} = \sum_{i=1}^{n} w_i \cos(\gamma_\mu B_i t), \tag{3.28}$$

where w_i is the spectral weight of the i'th oscillation, and B_i is the field magnitude at each muon implantation position. Figure. 3.20 has been simulated assuming two unique implantation positions, experiencing local fields of 5 mT and 3 mT.

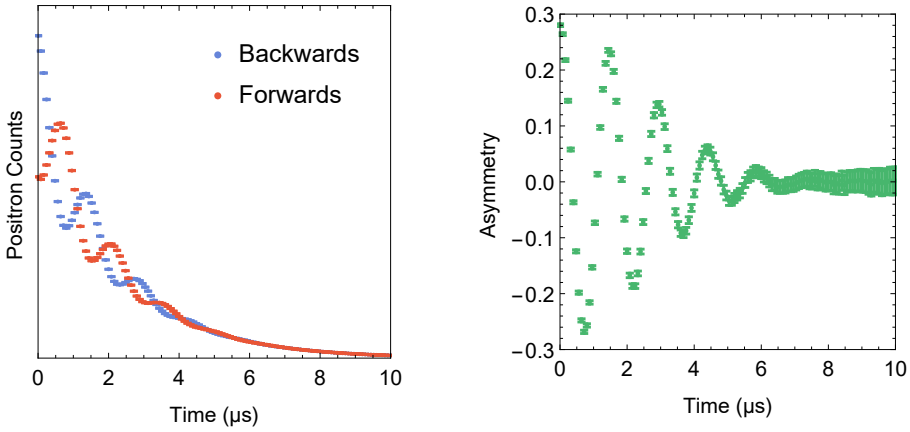

Fig. 3.21 Simulated positron counts and corresponding asymmetry spectra, where Eq. (3.29) is the polarization function. Simulation parameters: $N_0 = 10^6$, $A_0 = 0.28$, $\alpha = 1$, $B = 5\,\mathrm{mT}$, $\sigma = 0.4\,\mu\mathrm{s}$.

.

Long-range magnetic order

The flux line lattice formed by a superconductor in the mixed state gives rise to a distinctive field distribution, the shape of which depends in general on the Ginzburg-Landau parameter κ and the strength of the applied magnetic field. The muons implanted in the sample effectively randomly sample this field distribution, as the length scale of the magnetic unit cell tends to be several hundred nanometres. In principle, the depolarization of the muon ensemble can be used to calculate the exact form of the internal field structure. However, due to effects such as polycrystalline averaging, vortex disorder, and the intrinsic instrument response, the ideal structure is broadened to look like an asymmetric Gaussian distribution. In general, the polarization time spectra can be modelled as the sum of n Gaussian damped oscillatory functions [23]:

$$G_z^{\mathrm{GD}} = \sum_{i=1}^{n} w_i \cos(\gamma_\mu B_i t) \exp\left(-\frac{1}{2}\sigma_i^2 t^2\right), \tag{3.29}$$

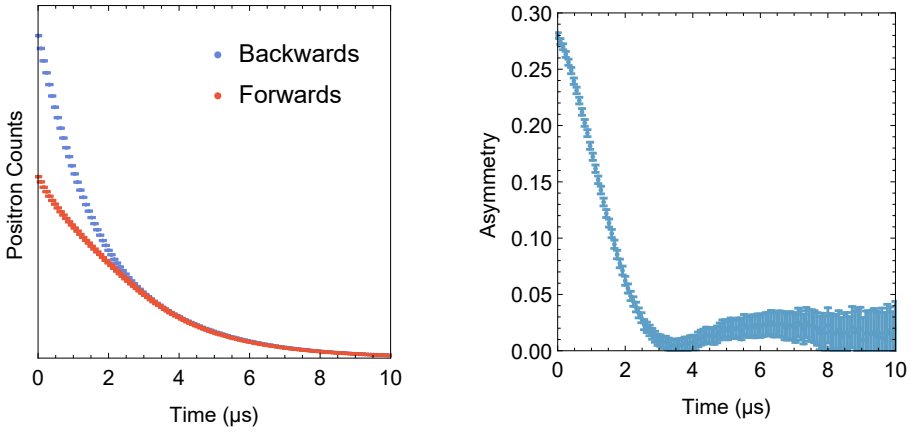

Fig. 3.22 Simulated positron counts and corresponding asymmetry spectra, where Eq. (3.31) is the polarization function. Simulation parameters: $N_0 = 10^6$, $A_0 = 0.28$, $\alpha = 1$, $\Delta = 0.5\,\mu s^{-1}$, $\Lambda = 0.2\,\mu s^{-1}$.

where σ_i/γ_μ is the width of the i'th Gaussian field distribution centred on B_i. From this we are able to calculate the first and second moments of this distribution:

$$\langle B \rangle = \frac{1}{w_T} \sum_{i=1}^{n} w_i B_i, \tag{3.30a}$$

$$\langle \Delta B^2 \rangle = \frac{1}{w_T} \sum_{i=1}^{n} w_i \left[\frac{\sigma_i^2}{\gamma_\mu^2} + (B_i - \langle B \rangle)^2 \right], \tag{3.30b}$$

where $w_T = \sum w_i$. A simulated spectrum with one oscillating component is presented in Fig. 3.21.

Composite polarization functions

It is very often the case that the local magnetic environment contains contributions from multiple sources of depolarization or precession. A composite polarization function may be constructed by multiplying together each of the polarization functions introduced previously. For example, in magnetic materials, the oscillations are often exponentially damped due to the presence of fast magnetic fluctuations. In this case, a trial depolarization function can be constructed by multiplying Eqs. (3.28) and (3.27).

A very commonly observed depolarization behaviour is an exponentially damped Gaussian Kubo-Toyabe function:

$$\begin{aligned} G_z^{\exp-\mathrm{KT}}(t) &= G_z^{\mathrm{FF}}(t)G_z^{\mathrm{KT}}(t) \\ &= e^{-\Lambda t}\left[\frac{1}{3}+\frac{2}{3}(1-\Delta^2t^2)\exp\left(-\frac{1}{2}\Delta^2t^2\right)\right]. \end{aligned} \tag{3.31}$$

One physical interpretation of this is the coexistence of spin fluctuations, and a static Gaussian nuclear dipole field. Figure 3.22 has been simulated using $\Lambda = 0.2\,\mu\mathrm{s}^{-1}$ and $\Delta = 0.5\,\mu\mathrm{s}^{-1}$. Comparing this with Figs. 3.17 and 3.19, it is clear that Λ has the biggest effect on the tail of the polarization function, whereas Δ has the largest effect on the initial slope of the depolarization.

The role of Fourier transforms

The link between the time domain and the frequency domain can be made clearer by considering Fourier transformations. A Dirac-delta function in frequency space corresponds to a pure oscillatory signal in the time domain. In the language of muons, the frequency distribution is directly proportional to the field distribution, $P(B)$, as the constant of proportionality is the gyromagnetic ratio γ_μ. A broad peak in the frequency domain corresponds to a damped oscillation in the time spectra, and so a broader field distribution will be observed as a faster depolarization rate in μSR spectra.

Chapter 4

Time-reversal symmetry breaking in La_7Ir_3

4.1 Introduction

As discussed in Sec. 2.4, materials in which the crystal structure maintains inversion symmetry, parity is a good quantum number. In these centrosymmetric materials, electron pairing states are expected to be purely singlet or triplet, with no mixing expected. Systems lacking a centre of inversion symmetry exhibit a non-uniform lattice potential, and give rise to an antisymmetric spin-orbit coupling. The effect of this ASOC is to split the Fermi surface into separate $\vec{k}$-dependent bands, each of which may have their own energy gap [50]. Cooper pairs are formed of electrons that belong to different parts of this split Fermi surface - a completely different situation from the conventional case, which leads to rich and interesting new physics. Another effect of ASOC is the presence of spin fluctuations, which tend to mix spin-singlet and spin-triplet superconducting channels [51]. This mixed-parity state means that NCS superconductors might be expected to exhibit broken time-reversal symmetry, and non-trivial line nodes in the order parameter [52].

Whilst non-centrosymmetric superconductors have been known about for a relatively long time [53], it took the discovery of heavy fermion superconductivity in $CePt_3Si$ [54] to catalyse a new era of theoretical and experimental interest in the field. The discovery was quickly followed by pressure induced superconductivity in $CeRhSi_3$ [55], $CeIrSi_3$ [56] and $CeCoGe_3$ [57], all of which exhibit antiferromagnetism at ambient pressure. The strong electron correlations present in these systems tend to complicate the study of the effect of non-centrosymmetry on the superconductivity. Recently, focus has switched to looking at non-centrosymmetric compounds

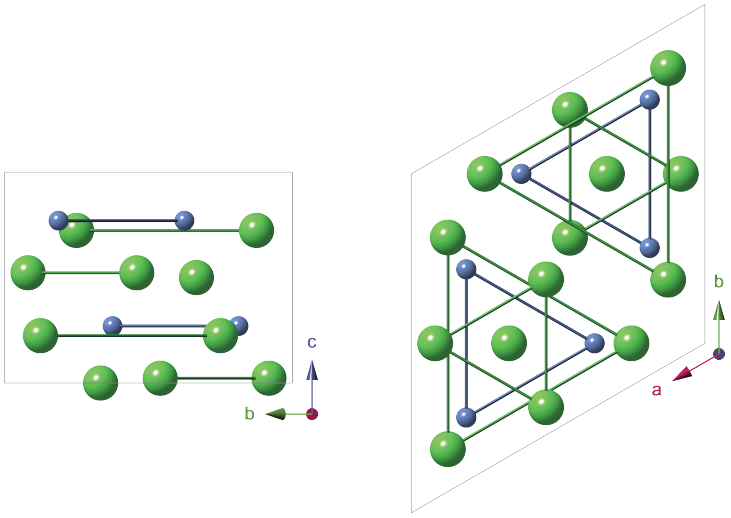

Fig. 4.1 Crystal structure of La_7Ir_3. La atoms are the large green spheres, whereas the Ir atoms are smaller, in blue. The *a*, *b* and *c* crystallographic axes are also labelled.

formed of the transition metal elements, as the complicating heavy fermion behaviour due to the presence of *f*-electrons is avoided. Unconventional superconductivity has been reported in $LaNiC_2$ [12], however this behaviour is relatively rare, as a large part of this family seems to exhibit conventional spin-singlet superconductivity - for example, $CaPtSi_3$, $CaIrSi_3$ [58]. Of particular interest in these systems is the effect of adjusting the spin-orbit coupling by doping of atoms of differing masses. A recent study found that $LaPdSi_3$ is changed from a type-I to a type-II superconductor by exchanging Pd for Pt, with both materials exhibiting a fully gapped order parameter [59]. These results are not incompatible with the theoretical expectations of NCS superconductors - they merely suggest that the triplet channel in these materials is severely suppressed by impurity scattering.

La_7Ir_3 is a member of a large family of binary 7 : 3 compounds, in which many members exhibit magnetism or superconductivity. The prototypical structure is given by Th_7Fe_3, which crystallizes in the $P6_3mc$ space group (see Fig. 4.1). Superconductivity has been reported in La_7Ir_3 with a transition temperature of $T_c = 2.24$ K, although the significance of the lack of inversion symmetry was not noted by the original authors [60, 61]. The superconducting properties of the related compounds La_7T_3 (T = Pd, Rh, Ru) were investigated in Ref. [62]. The superconductivity in these materials appears to be weakly coupled, especially in the Ru compound.

In this chapter, the superconductivity of La_7Ir_3 has been characterized using magnetization, heat capacity, and μSR measurements. Zero-field μSR reveals the

presence of spontaneous static or quasi-static magnetic fields below the superconducting transition temperature T_c= 2.25 K - a clear indication that the superconducting state breaks time-reversal symmetry. Furthermore, TF-μSR rotation measurements suggest that the superconducting gap is isotropic, and that the pairing symmetry of the superconducting electrons is predominantly *s*-wave. The results indicate that the superconductivity in La_7Ir_3 may be unconventional, and paves the way for further studies of this family of materials.

4.2 Sample synthesis

A polycrystalline sample of La_7Ir_3 was prepared by arc-melting stoichiometric quantities of La (99.9%, Alfa-Aesar) and Ir (99.99%, Alfa-Aesar) using a tri-arc furnace. After the initial melt, the sample was turned and remelted several times to ensure homogeneity of the constituent elements. The sample was then sealed in an evacuated quartz tube, and annealed for 5 days at 800 °C. The final material was very brittle, and crushed easily into a powder for the characterization and μSR experiments. The material is air sensitive, rapidly developing a dark blue surface discolouration if exposed to atmosphere. The sample was stored in a glove-box under an Argon atmosphere, and all preparatory work (e.g. powdering for XRD and μSR experiments) took place in an inert atmosphere.

4.3 Crystallography

Powder X-ray diffraction measurements were performed using a Panalytical X-Pert Pro diffractometer, with the resulting data presented in Fig. 4.2. The total count time was limited to less than an hour due to the air sensitivity of the sample. The crystal structure was Rietveld refined using the TOPAS software [63], and is described well by a model with only a single phase of the expected Th_7Fe_3 non-centrosymmetric structure. The refined lattice parameters are $a = 10.2376(3)$ Å and $c = 6.4692(3)$ Å, with the full results given in Tab. 4.1. This is in good agreement with previously reported values [60]. No impurity phases were detected in the sample to within the sensitivity of the measurement.

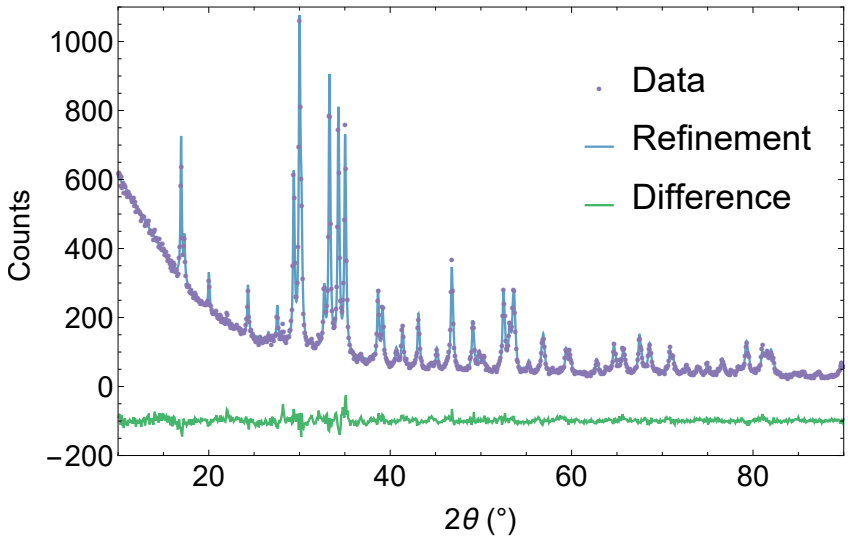

Fig. 4.2 Room-temperature XRD spectra of the La_7Ir_3 sample. The lower plot is the difference between the data and the refined spectrum.

4.4 Magnetization

Low temperature magnetization measurements were performed using a Quantum Design 5 T MPMS, as described in Sec. 3.2.1. A small piece of polycrystalline sample of roughly tetrahedral shape was used, with a mass of 39.6 mg. Fig 4.3 shows the low-temperature magnetic susceptibility $\chi(T)$. The sample was initially cooled to 1.8 K in zero field, at which point a field of 1 mT was applied. Data were collected as the sample was warmed to 5 K, and subsequently as the sample was cooled again under the applied field. A clear superconducting transition is visible at $T_c = 2.25$ K, at which point the magnetization of the sample drops sharply. The data have been corrected with a demagnetization factor $D = 1/3$, yielding a value of χ that is close to -1 at the lowest temperatures measured, indicating bulk superconductivity in this sample.

The field dependent magnetization was measured using an Oxford Instruments Vibrating Sample Magnetometer. Figure 4.4 displays low-induction magnetization against field data after correcting for demagnetization. Below H_{c1}, the sample is a perfect diamagnet, and the magnetic response is linear with gradient $M/H = -1$. Above H_{c1}, flux begins to penetrate the sample, and the magnetization response begins to deviate from linearity. The data suggest values of $\mu_0 H_{c1}(1.8\text{ K}) = 0.90(5)$ mT and $\mu_0 H_{c1}(1.5\text{ K}) = 1.40(5)$ mT.

Figure 4.5 presents a high-induction magnetization hysteresis loop, collected at a temperature of 1.5 K. The upper critical field is taken as the point where

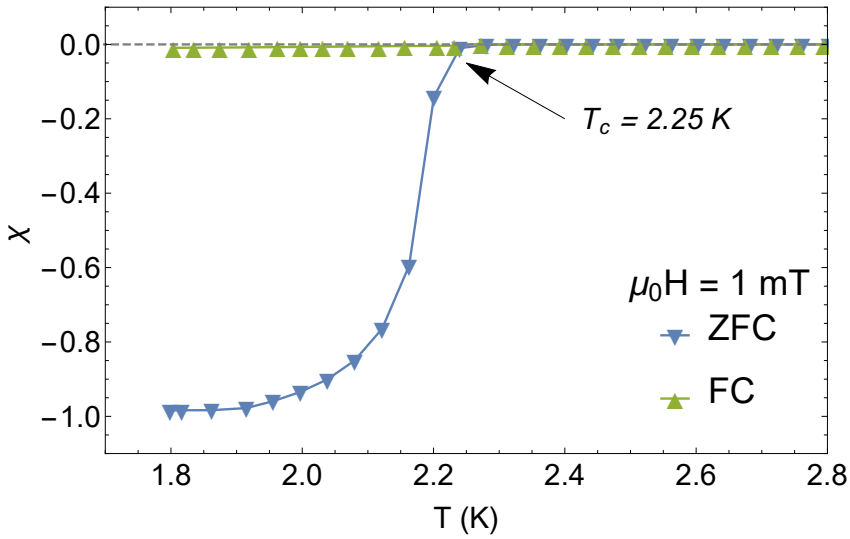

Fig. 4.3 Temperature dependence of the magnetic susceptibility, collected in zero-field cooled (ZFC) and field cooled (FC) regimes under an applied field of 1 mT.

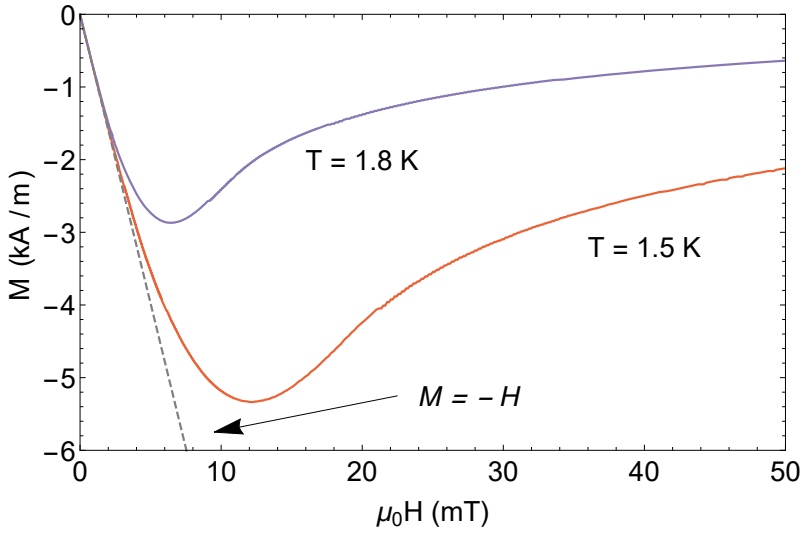

Fig. 4.4 Field dependence of the magnetization at 1.5 K and 1.8 K after cooling in zero field. The applied field H has been corrected for demagnetization effects.

Table 4.1 Crystallographic parameters obtained from the structural Rietveld refinement of the room-temperature powder XRD data of La_7Ir_3. The goodness of fit is 1.183.

Structure		Th_7Fe_3		
Space-group		$P\,6_3\,m\,c$ (No. 186)		
Lattice parameters				
	a (Å)	10.2376(4)		
	c (Å)	6.4692(3)		
	V_{cell} (Å^3)	587.19(5)		
Atom	Wyckoff Position	x	y	z
La1	2a	1/3	2/3	0
La2	6c	0.125(1)	0.875(2)	0.224(1)
La3	6c	0.541(2)	0.459(1)	0.023(3)
Ir1	6c	0.812(2)	0.188(1)	0.270(1)

the magnetic behaviour becomes irreversible, giving $\mu_0 H_{c2}(1.5\text{ K}) = 0.42\,\text{T}$ and $\mu_0 H_{c2}(1.8\text{ K}) = 0.23\,\text{T}$, above which point the sample returns to the normal state. Solving Eqs. (2.12) and (2.13) simultaneously, we find estimates of $\lambda(1.5\text{ K}) = 600\,\text{nm}$ and $\xi(1.5\text{ K}) = 28.0\,\text{nm}$. Therefore we can classify La_7Ir_3 as a type-II superconductor, as $\kappa = 21.4 \gg 1/\sqrt{2}$.

Table 4.2 Summary of the superconducting properties of La_7Ir_3 determined from magnetization measurements.

T (K)	H_{c1} (mT)	H_{c2} (mT)	$\xi(T)$ (nm)	$\lambda(T)$ (nm)	$\kappa(T)$
1.5	1.4(1)	420(5)	28.0(2)	600(20)	21.4(9)
1.8	0.9(1)	227(5)	38.1(4)	740(50)	19(1)

Following Ref. [33], the high field data collected in the normal state at $T = 5\,\text{K}$ have been fitted to the following model:

$$M(H) = M_s + \chi H, \tag{4.1}$$

where M_s is the saturation magnetization, and χ is the intrinsic magnetization. This yields $M_s = 78.1(3)\,\text{A m}^{-1}$ and $\chi = 3.885(8) \times 10^{-5}$. The diamagnetic contribution to the susceptibility from the atoms is found to be $\chi_{\text{core}} = -1.00 \times 10^{-5}$ using the values published in Ref. [64].

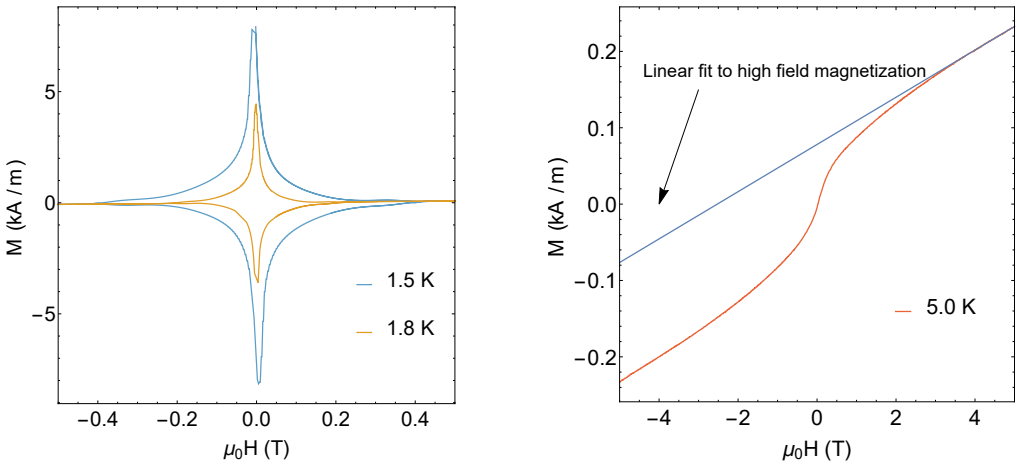

Fig. 4.5 (a) Field dependence of magnetization collected at two temperatures below T_c. The upper critical field is the field where the two curves become irreversible, i.e. the point at which the magnetization loop closes. (b) Field dependence of magnetization in the normal state, just above T_c. A linear fit was applied to the high-field magnetization data in order to estimate the magnetic susceptibility, and the saturation magnetization.

4.5 Heat Capacity

Zero-field heat capacity data collected in the temperature range $1.8\,\mathrm{K} \leq T \leq 300\,\mathrm{K}$ are displayed in Fig. 4.6. There is a discontinuity at $T_C = 2.25\,\mathrm{K}$, indicating the transition to bulk superconductivity. The discontinuity is slightly rounded from the ideal peak, however does rise sharply at T_c. The heat capacity in the normal state has been used to fit the Debye-Einstein model of Eqs. (2.61)-(2.64), with the results presented in the upper half of Tab. 4.3. At high temperatures, the total heat capacity approaches the Dulong-Petit limit of $3pR = 249\,\mathrm{J\,mol^{-1}\,K^{-1}}$, where $p = 10$ is the number of atoms per formula unit [34]. The magnitude of the heat capacity discontinuity yields an estimate of $\alpha_{\mathrm{HC}} = 1.51(5)$ using Eq. (2.69), which is smaller than the BCS value of $\alpha_{\mathrm{BCS}} = 1.764$.

4.6 Muon spin rotation and relaxation

4.6.1 Transverse field

Transverse field μSR (TF-μSR) was performed in the field range $10 \leq \mu_0 H \leq 50$ mT. The field was applied above T_c before cooling through the superconducting transition to a temperature of 100 mK, in order to stabilize a well-ordered flux line lattice

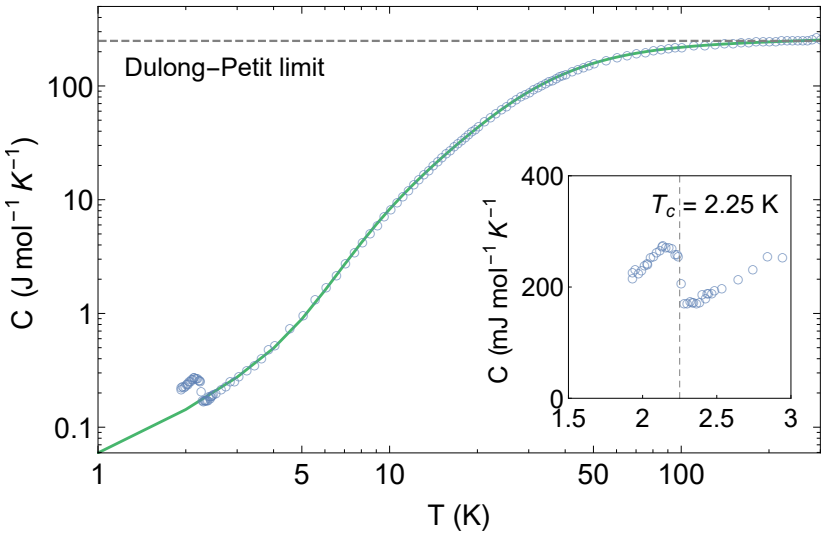

Fig. 4.6 Temperature dependence of the heat capacity in zero-field plotted on a log-log scale, with a fit to Eq. (2.61). Inset: close up of the superconducting transition with the position of T_c marked.

Table 4.3 Summary of the superconducting and normal state properties of La_7Ir_3 determined from heat capacity measurements. Reported values for La_7Rh_3 from Ref. [62] are also presented for comparison.

Property	La_7Ir_3 (present work)	La_7Rh_3 [62]
Normal state		
γ (mJ mol^{-1} K^{-2})	47(1)	48
Θ_D (K)	158.8(8)	160
Θ_E (K)	46.9(5)	-
N_D/N_E	13.4(6)	-
Superconducting state		
T_c (K)	2.25(1)	2.6
ΔC (mJ mol^{-1} K^{-1})	110(7)	-
$\Delta C/\gamma T_c$	1.04(7)	1.4
α_{HC}	1.51(5)	1.75
λ_{ep}	0.61(3)	0.64

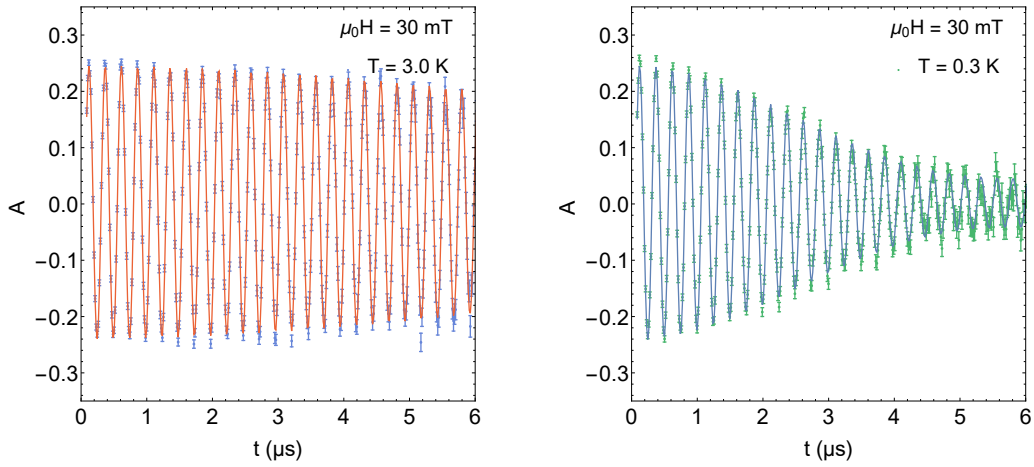

(a) (b)

Fig. 4.7 Representative TF-μSR signals collected (a) above and (b) below T_c in an applied magnetic field of 30 mT.

in the mixed state of the superconductor. Asymmetry signals collected above and below T_c are shown in Fig. 4.7. The time evolution of the asymmetry is described by a sinusoidal function damped with Gaussian relaxation, plus a non-decaying oscillation that originates from muons stopping in the silver:

$$G_{\mathrm{TF}}(t) = A_1 \exp\left(-\frac{\sigma^2 t^2}{2}\right)\cos(\gamma_\mu B_1 t + \phi) + A_2 \cos(\gamma_\mu B_2 t + \phi). \tag{4.2}$$

Here, A_1 and A_2 are the sample and background asymmetries, B_1 and B_2 are the average fields in the superconductor and silver, ϕ is a shared phase offset, and $\gamma_\mu/2\pi = 135.5$ MHz T^{-1} is the muon gyromagnetic ratio. The depolarization rate, σ, is related to the variance of the magnetic field distribution in the superconductor. The σ values, determined by fitting the data to Eq. (4.2), are displayed in Fig. 4.8(a). The field distribution of the flux line lattice is broadened by the presence of randomly oriented nuclear magnetic moments in the sample. The depolarization due to this nuclear dipolar field σ_{N} is assumed to be temperature independent, and adds in quadrature to the contribution from the flux line lattice σ_{FLL}:

$$\sigma^2 = \sigma_{\mathrm{FLL}}^2 + \sigma_{\mathrm{N}}^2. \tag{4.3}$$

A background term was included to account for the nuclear contribution in our analysis, with the approximately field independent value $\sigma_{\mathrm{N}} = 0.116 \pm 0.003\ \mu\mathrm{s}^{-1}$.

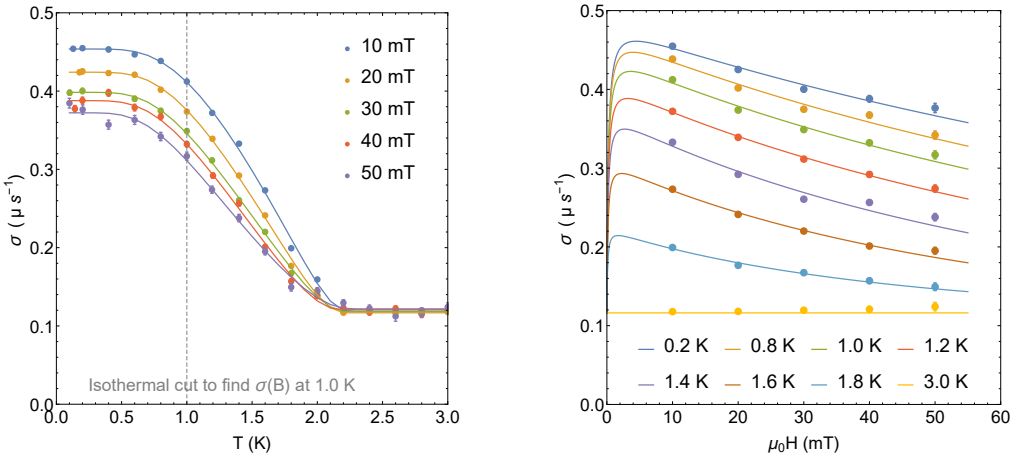

Fig. 4.8 (a) Temperature dependence of the TF-μSR depolarization rate, σ, collected in a range of fields between 10 mT and 50 mT. The lines are fits to Eq. (2.71), and are intended as guides to the eye. (b) Field dependence of σ, generated by transposing the dataset displayed in (a). The solid lines are calculations of the field dependence of σ as described in Sec. 2.2.1.

The initial fitting procedure yielded $\sigma(T)$ for a number of different applied fields. This dataset was subsequently transposed, in order to show the field dependence of σ for each temperature. The result of this process is presented in Fig. 4.8(b). The field dependence is calculated using the equations described in Sec. 2.2.1, and the results of fitting the parameters $\lambda(T)$ and $H_{c2}(T)$ to the data are given by the solid lines in the figure. The full temperature dependence of the inverse-squared penetration depth extracted in this manner is displayed in Fig. 4.9, with fits to isotropic *s*-wave gaps in the clean and dirty limits. The full list of fitted parameters in the clean and dirty limits are presented in Tab. 4.4. The resultant values for the energy gaps are $\Delta_0|_{\text{clean}} = 0.369(3)$ meV and $\Delta_0|_{\text{dirty}} = 0.305(9)$ meV, with corresponding values of $\alpha|_{\text{clean}} = 1.96(2)$ and $\alpha|_{\text{dirty}} = 1.57(5)$. Within error, the dirty limit value is in agreement with the estimate from the heat capacity of $\alpha_{\text{HC}} = 1.51(5)$. The value of α in this limit is slightly smaller than $\alpha_{\text{BCS}} = 1.764$. The absolute value of the magnetic penetration depth at $T = 0$ is given by both models as $\lambda(0) = 482(2)$ nm.

4.6.2 Longitudinal and zero-field

We now consider the results from the zero-field (ZF) and longitudinal-field (LF) experiments. Figure 4.10 shows the relaxation spectra collected above and below the superconducting transition temperature in ZF. There is a clear change in the relaxation behaviour on either side of the transition. The increased relaxation below

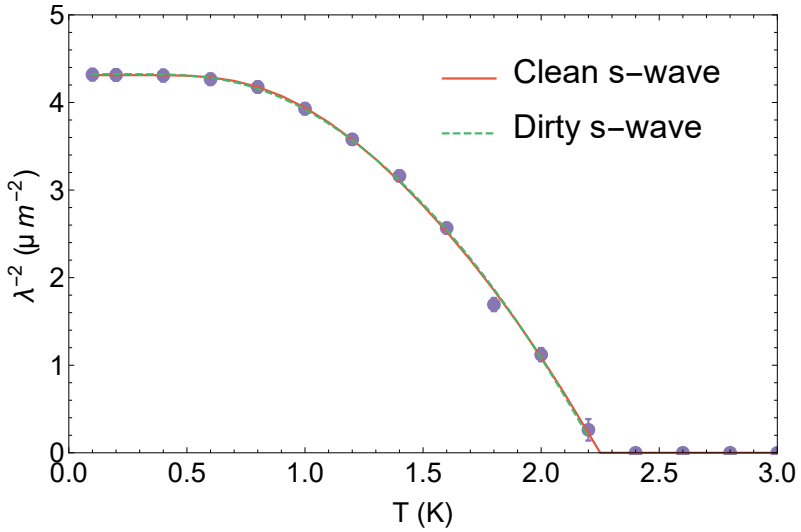

Fig. 4.9 Extracted temperature dependence of the inverse magnetic penetration depth squared. The results of fitting isotropic *s*-wave models for the gap in the clean and dirty limits are displayed as solid and dashed lines, respectively. These correspond to Eqs. (2.70) and (2.71), respectively.

Table 4.4 Results of fitting the inverse squared penetration depth to clean (Eq. (2.70)) and dirty (Eq. (2.71)) models.

Property	Unit	Clean	Dirty
$\lambda^{-2}(0)$	μm^{-2}	4.31(3)	4.32(3)
T_c	K	2.25(2)	2.24(2)
Δ_0	meV	0.370(6)	0.305(9)
$\alpha_\mu \equiv \Delta_0/k_B T_c$		1.90(3)	1.57(5)
$\lambda(0)$	nm	482(2)	482(2)

T_c has been verified with the MuSR instrument in both longitudinal and transverse geometries, which requires a physical rotation of the zero-field coils by 90°. There is no hint of an oscillatory component in the spectra, which would otherwise suggest the presence of an ordered magnetic structure. In the absence of atomic moments, the depolarization of the muon ensemble is due to the presence of static, randomly oriented nuclear moments. This behaviour is modelled by the Gaussian Kubo-Toyabe equation [49]

$$G_{KT}(t) = \frac{1}{3} + \frac{2}{3}(1 - \sigma_{ZF}^2 t^2) \exp\left(-\frac{\sigma_{ZF}^2 t^2}{2}\right) \tag{4.4}$$

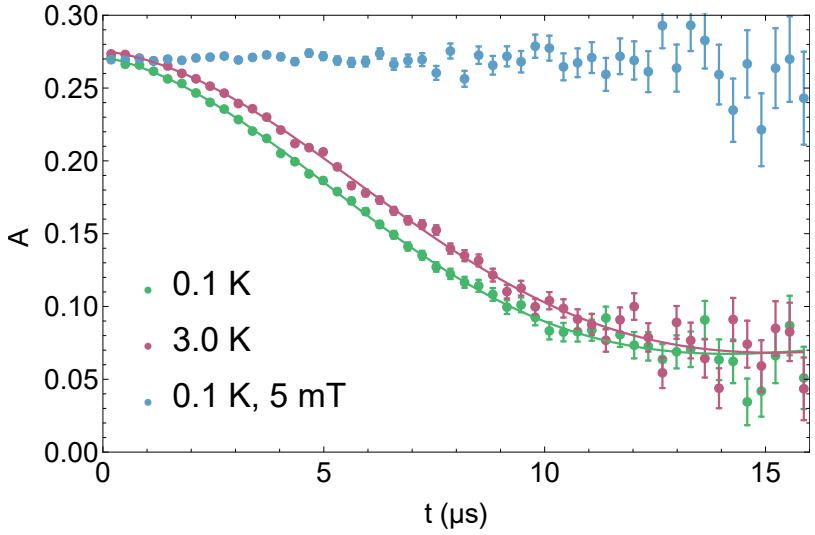

Fig. 4.10 ZF and LF-μSR spectra collected above and below T_c, with least-squares fits using the model of Eq. (4.5) (solid lines). The effect of applying a small LF field of 5 mT is also shown.

where σ_{ZF} measures the width of the nuclear dipolar field experienced by the muons. The spectra are well described by the function

$$G(t) = A_0 G_{KT}(t) \exp(-\Lambda t) + A_{bg}, \tag{4.5}$$

where A_0 and A_{bg} are the sample and background asymmetries, respectively, and Λ measures the electronic relaxation rate.

The parameters A_0 and A_{bg} are found to be approximately temperature independent. The nuclear depolarization rate σ_{ZF} remains approximately flat, except as $T \to 0$ K where a slight increase is observed. The electronic relaxation rate Λ shows a systematic increase below the superconducting transition temperature (see Fig. 4.11). An exponential relaxation process is generally attributed to the field distribution arising from fast fluctuating electronic spins, which cause motional narrowing of the muons depolarization rate. However, a weak magnetic field of only 5 mT is enough to fully decouple the muon from this exponential relaxation channel. This implies that the relaxation mechanism is actually static or quasi-static with respect to the muon lifetime. Furthermore, spin fluctuations associated with the proximity to a quantum critical point would be expected to exhibit a Curie-Weiss-like temperature dependence, as opposed to the onset at T_c observed [65].

Thus, it is likely that the source of the ZF signals observed below T_c is unique to the La_7Ir_3, and corresponds to the onset of a superconducting channel that breaks time-reversal symmetry. Aoki *et al.* have discussed the probable sources of the

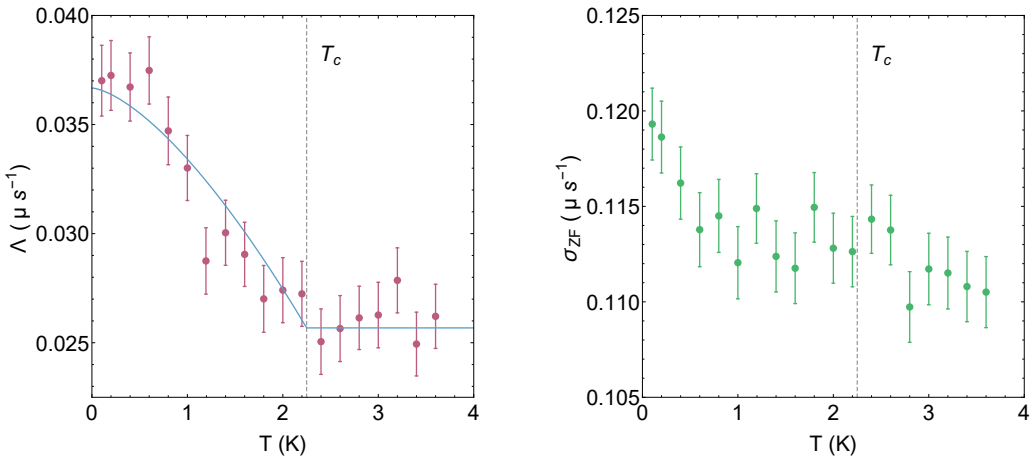

Fig. 4.11 Temperature dependence of (a) the electronic relaxation rate Λ and (b) the Gaussian relaxation rate σ_{ZF}. A clear increase at T_{c} is observed in Λ, whereas σ_{ZF} remains relatively constant throughout T_{C}.

spontaneous field in superconductors with TRSB [11]. In systems where the Cooper pairs have non-zero spin and orbital moments, regions in the sample where the order parameter becomes spatially inhomogeneous, such as grain boundaries, surfaces, and impurity sites, act as field sources due to the undamped supercurrents that arise there [66]. Alternatively, if the Cooper pairs have only non-zero spin moments, a hyperfine field may be generated at the interstitial μ^+ sites.

The TRSB signals are observed in the Λ relaxation channel, akin to the NCS $LaNiC_2$ and Sr_2RuO_4 [10]. This implies that the sources of field are dilute, producing a Lorentzian field distribution that is randomly sampled by the muons. If the field sources are caused by inhomogeneities in the order parameter, one would expect the Cooper pairs to possess a non-zero orbital momentum. However, the temperature dependence of the magnetic penetration depth is well described by an isotropic *s*-wave model. A further complication for NCS is that the ground state may be an admixture of spin-singlet and spin-triplet superconductivity. If the Cooper pairs do indeed have an orbital momentum, it is likely that the effect of polycrystalline averaging, coupled with a large relative strength of the singlet to triplet channels, have made its detection difficult given the sensitivity of the current experiment.

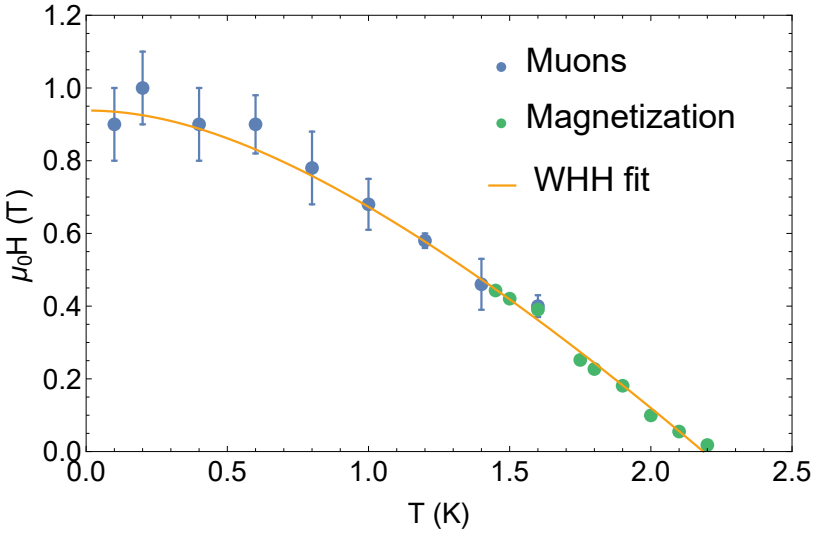

Fig. 4.12 Determination of the upper critical field via magnetization and μSR measurements. The solid line is the result of fitting the WHH model to the data.

4.7 Discussion

4.7.1 Critical fields

The T-dependence of the upper critical field has been determined from magnetization and μSR measurements. The field dependence of the magnetization yielded data above $T = 1.45\,\mathrm{K}$, and fitting the field dependence of the muon spin depolarization rate σ yielded the low temperature data points. The full dataset is presented in Fig. 4.12. In order to fit the data, we used the WHH (Werthamer, Helfrand and Hohenberg) theory, which takes into account the effect of Pauli limiting and spin-orbit scattering of quasiparticles on H_{c2} [67]. The result of the fit is shown as the solid line in Fig. 4.12, and yields a value for the Maki parameter of $\alpha_M = 0.311(7)$. The upper critical field at $T = 0\,\mathrm{K}$ is also found to be $\mu_0 H_{c2}(0) = 0.97(3)\,\mathrm{T}$. The validity of using the WHH theory for this sample is shown by evaluating Eq. (2.60). A linear fit to the upper critical field in the vicinity of T_c yields $dH_{c2}/dT = -0.6\,\mathrm{T\,K^{-1}}$, which results in the WHH estimate of $\alpha_M = 0.32$. As this is close to the value of the fitted parameter, the WHH theory is valid.

The Maki parameter measures the relative contributions of the orbital and Pauli-limiting de-pairing mechanisms on the measured upper critical field. Using Eqs. (2.56) and (2.57), the Pauli limiting field is found to be $H_P(0) = 4.53(6)\,\mathrm{T}$, with the orbital limit $H_{c2}^{Orb}(0) = 1.00(3)\,\mathrm{T}$. To within error, the experimental upper

critical field is equal to the orbital limit. Therefore we can conclude that Pauli limiting effects are not important in the superconductivity of La_7Ir_3.

An estimate for the thermodynamic critical field can be made using the α-model equation [32]

$$H_c(0) = \alpha T_C \left(\frac{6\gamma_{nV}}{\pi}\right)^{1/2}, \tag{4.6}$$

where γ_{nV} is the Sommerfeld coefficient per unit volume, and is calculated from the molar volume in units of erg cm^{-3} K^{-2}. For La_7Ir_3, $\gamma_{nV} = 2660(60)$ erg cm^{-3} K^{-2}, leading to $\mu_0 H_C(0) = 30.6(5)$ mT. The low temperature value of κ can then be calculated using the equation (*c.f.* Eq. (2.15))

$$\kappa = \frac{H_{c2}}{\sqrt{2}H_c}. \tag{4.7}$$

Using $H_{c2}(0) = 0.97(3)$ T and $\mu_0 H_C(0) = 30.6(5)$ mT yields $\kappa = 22.4(6)$, confirming type-II superconductivity in La_7Ir_3. This is in good agreement with the estimates of κ made in Sec. 4.4. The $T = 0$ value of the lower critical field H_{C1} is estimated from κ and H_C using the equation

$$H_{C1} = H_C \frac{\ln \kappa_{GL}}{\sqrt{2}\kappa_{GL}}, \tag{4.8}$$

which using the above values is $H_{C1} = 3.00(8)$ mT. This value, as well as the two values determined from magnetization measurements, are plotted in Fig. 4.13. The lower critical field can be modelled with the equation

$$H_{C1}(T) = H_{C1}(0)\left[1 - \left(\frac{T}{T_c}\right)^{\delta}\right], \tag{4.9}$$

where the power, δ, is equal to 2 in the conventional case. The observed H_{c1} values are consistent with $\delta = 1.6$, as plotted in Fig. 4.13. Also, the effective penetration depth may be estimated from $H_{c1}(0)$ and $H_c(0)$ by the equation (*c.f.* Eq. (2.13))

$$\lambda^2(0) = \frac{\Phi_0 H_{c2}(0)}{4\pi H_c^2(0)}, \tag{4.10}$$

which yields $\lambda(0) = 500(20)$ nm. Within error, this is in agreement with the μSR value of $\lambda(0) = 482(2)$ nm. This shows that the results from the μSR study are consistent with the calculations based on the magnetization and heat capacity experiments.

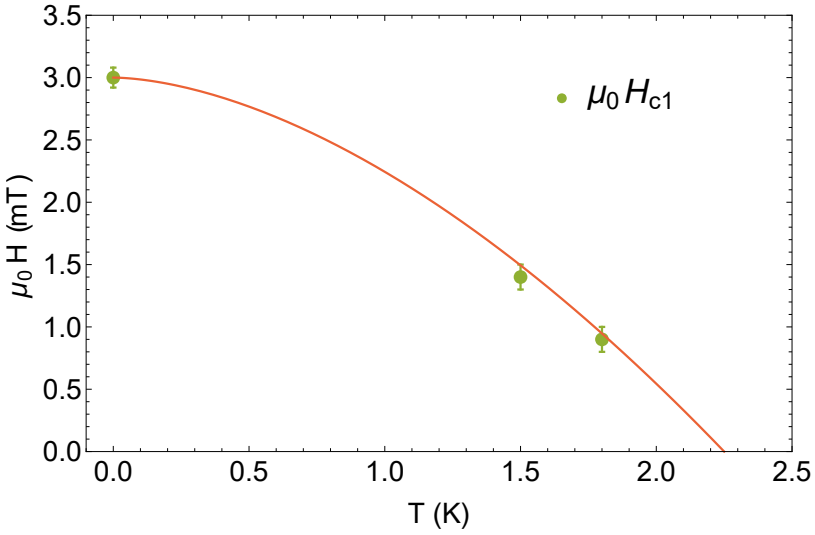

Fig. 4.13 Temperature dependence of H_{c1}, estimated from magnetization measurements. The zero temperature value was calculated using Eq. (4.8) as described in the text. The solid line is a plot of Eq. (4.9), with the power $\delta = 2.5$.

4.7.2 Electronic properties

In order to find a self-consistent description of the microscopic properties of La_7Ir_3, the results of the heat capacity, magnetization, and μSR measurements can be combined. The Sommerfeld constant, γ, determined from low temperature heat capacity, is related to the electronic properties of the system by the equation

$$\gamma = \left(\frac{\pi}{3}\right)^{2/3} \frac{k_B^2 m^* n^{1/3}}{\hbar^2}, \tag{4.11}$$

where m^* is the effective mass of quasiparticles, and n is the quasiparticle number density per unit volume. A closely related property is the London penetration depth, which is defined by the normal state properties:

$$\lambda_L = \left(\frac{m^*}{\mu_0 n e^2}\right)^{1/2}. \tag{4.12}$$

In the clean limit, it is possible to use measured values of λ and γ from μSR and heat capacity measurements to simultaneously solve these equations to find m^* and n. However, in dirty limit superconductors, this ratio is larger than unity, and therefore the scattering of electrons in Cooper pairs is expected to interfere with the superconducting ground state. One consequence is that the penetration depth is expected to be longer than the (ideal) London penetration depth, where the effective

Table 4.5 Electronic properties of La_7Ir_3.

Property	Unit	Clean ($\Delta_0 = 0.370\,\mathrm{meV}$)	Dirty ($\Delta_0 = 0.305\,\mathrm{meV}$)
m^*/m_e		13.3	13.0
n	$10^{27}\,\mathrm{m}^{-3}$	1.89	2.04
ξ_0	nm	18.8	24.0
l_e	nm	116	84.2
ξ_0/l_e		0.163	0.285
λ_L	nm	447	425
v_F	$\mathrm{m\,s}^{-1}$	33 200	34 881

penetration depth at $T = 0$ is given by

$$\lambda(0) = \lambda_L \left(1 + \frac{\xi_0}{l_e}\right)^{1/2}. \tag{4.13}$$

The GL coherence length is also affected by this dirty limit correction. The relationship between the BCS coherence length, the mean free path, and the Ginzburg-Landau coherence length at $T = 0$, $\xi(0)$, is given by [33]

$$\frac{\xi(0)}{\xi_0} = \frac{\pi}{2\sqrt{3}} \left(1 + \frac{\xi_0}{l_e}\right)^{1/2}. \tag{4.14}$$

Equations (4.11)-(4.14), together with Eqs. (2.30) and (2.31), form a system of equations that can be solved simultaneously to find estimates of the parameters m^*, n, l_e, and ξ_0. This was carried out using the Solve routine in the Mathematica software, where the measured values $\gamma = 47\,\mathrm{mJ\,mol}^{-1}\,\mathrm{K}^{-2}$, $\lambda(0) = 482\,\mathrm{nm}$ and $\xi(0) = 18.4\,\mathrm{nm}$. The calculation also requires that a value for Δ_0 is fixed. The effect of using the values discerned from the μSR penetration depth measurement in the clean and dirty limits has been compared in Tab. 4.5.

The BCS coherence length calculated in this manner is smaller than the electronic mean free path, for both the clean and dirty limit values of the superconducting gap energy. Both values of the ratio ξ_0/l_e are intermediate between the dirty limit, where $\xi_0/l_e \gg 1$, and the clean limit, where $\xi_0/l_e \ll 1$. This implies that La_7Ir_3 is in the intermediate regime, and may explain why the WHH calculations are applicable to the upper critical field data.

The values of m^* and n_s can be used to calculate an effective Fermi temperature for the superconductivity using the equation $k_B T_F = (\hbar^2/2)(3\pi^2 n_s)^{2/3}/m^*$. This yields $T_F = 522\,\mathrm{K}$, with the ratio $T_C/T_F = 0.0043$. Uemura *et al.* have described a method of classifying superconductors based on the ratio of the critical temperature

T_c to the effective Fermi temperature, T_F. It has been observed that the heavy fermion, high-T_C, organic, fullerene, as well as many other unconventional superconductors all lie in the range where $0.01 \leq T_C \leq 0.1$ [68–70]. La_7Ir_3 is located outside of this 'band of unconventionality', even though the observation of TRSB is highly unconventional (the position of this material on the Uemura plot is presented in Sec. 8.2, Fig. 8.1).

4.8 Summary & Conclusions

In conclusion, TF- and ZF-μSR measurements have been carried out on the non-centrosymmetric superconductor La_7Ir_3. A spontaneous magnetization is clearly observed at the superconducting transition temperature, confirming that time-reversal symmetry is broken in the superconducting state. However, the superconducting order parameter is described well by an isotropic gap with *s*-wave pairing symmetry and enhanced electron-phonon coupling. The results imply that La_7Ir_3 has a superconducting ground-state that features a dominant *s*-wave component, with the exact nature of the triplet component undetermined. In order to determine if the superconductivity is non-unitary, further experimental work on high quality single crystals is vital, coupled with group theory calculations to determine the allowed pairing symmetries. This work paves the way for further studies of the large number of superconductors in the Th_7Fe_3 family, in the hunt for unconventional behaviour.

Table 4.6 Properties of the normal and superconducting states in La_7Ir_3. In order: superconducting transition temperature; electron-phonon coupling constant under the McMillan formalism; superconducting energy gap; alpha parameter; Sommerfeld constant; Debye temperature; Einstein temperature; relative weight of Debye and Einstein heat capacities; upper critical field; Maki parameter; Pauli limiting field; orbital limiting field; thermodynamic critical field; lower critical field; GL coherence length; magnetic penetration depth; London penetration depth; GL parameter; quasiparticle effective mass; superconducting carrier density; BCS coherence length; electronic mean free path; dirty limit correction; Fermi velocity; Uemura parameter.

Property	Unit	Value
T_c	K	2.25(2)
λ_{ep}		0.61(3)
Δ_0	meV	0.370(6)
$\Delta_0/k_B T_c$		1.91(2)
γ	$mJ\,mol^{-1}\,K^{-2}$	47(1)
Θ_D	K	158.8(8)
Θ_E	K	46.9(5)
N_D/N_E		13.4(6)
$\mu_0 H_{c2}(0)$	T	0.97(2)
α_M		0.311(9)
$\mu_0 H_P(0)$	T	4.53(6)
$\mu_0 H_{c2}^{Orb}(0)$	T	1.00(3)
$\mu_0 H_c(0)$	mT	30.6(5)
$\mu_0 H_{c1}(0)$	mT	3.00(8)
$\xi(0)$	nm	18.4(2)
λ	nm	482(2)
λ_L	nm	447
κ_{GL}		22.4(6)
m^*	m_e	13.3
n	$10^{27}\,m^{-3}$	1.89
ξ_0	nm	18.8
l_e	nm	116
ξ_0/l_e		0.163
v_F	$m\,s^{-1}$	33 200
T_c/T_F		0.0043

Chapter 5

Probing noncentrosymmetric Re_3Ta

5.1 Introduction

Recent work has focused on the superconductivity in the transition metal solid solutions containing Re, which solidify in the α-Mn NCS crystal structure. A strong spin-singlet and triplet admixture has been reported in Re_6Zr [71], yet a similar study on Re_3W found a weakly coupled spin-singlet superconducting state [72]. Continuing the line of this investigation, we have conducted a detailed study of the superconductivity in Re_3Ta using bulk measurements of the magnetization, heat capacity, resistivity, and muon spectroscopy. Superconductivity in this material was first reported by Blaugher and Hulm [53], however no mention was made of the significance of the non-centrosymmetric structure. To supplement the laboratory based measurements, we have performed muon spin relaxation and rotation (μSR) measurements. Spin-triplet Cooper pairs have a non-zero total angular moment, which allows for the possibility of generating spontaneous fields in the sample upon transitioning into the superconducting state. Zero-field μSR is sensitive to fields as low as 0.1 G, and can be used to detect the field distribution setup upon the formation of spin-triplet superconductivity. It is thus an unambiguous method of detecting time-reversal symmetry breaking, and is a clear signal of unconventional superconductivity. In transverse-field μSR, the muons randomly sample the field distribution setup by the flux line lattice in the mixed state, and provide a direct measurement of the magnetic penetration depth λ. Tracking the temperature dependence of λ establishes whether the superconducting order parameter is fully gapped, or whether there exist point or line-nodes on the Fermi surface.

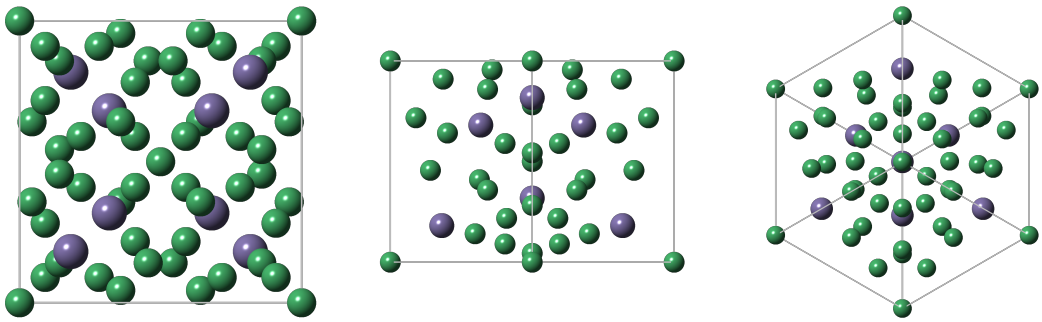

(a) (b) (c)

Fig. 5.1 Crystal structure of Re_3Ta, viewed along (a) the [100] direction, (b) the [110] direction, and (c) the [111] direction.

5.2 Sample synthesis

Stoichiometric quantities of Re (99.99%) and Ta (99.999%) were melted together in a tri-arc furnace under a high-purity Ar atmosphere. A Ti getter was utilized in order to reduce the effect of gaseous impurities. The as-cast ingot was flipped and remelted to ensure thorough mixing of the constituent elements. The sample was sealed inside an evacuated quartz tube and annealed at 800 °C for 1 week in order to stabilise the α-Mn structure and improve sample homogeneity. The final material was very brittle, and crushed easily to form powders for XRD and μSR experiments.

5.3 Crystallography

Powder X-ray diffraction measurements were performed using a Panalytical X-Pert Pro diffractometer, with the resulting data presented in Fig. 5.2. The crystal structure was Rietveld refined using the TOPAS software [63], and is described well by a model with only a single phase of the expected α-Mn non-centrosymmetric structure. The refined lattice parameter is $a = 9.69067(3)$ Å, with the full results given in Tab. 5.1. This is in good agreement with published literature [73, 74]. No impurity phases were detected in the sample to within the sensitivity of the measurement. The refined structure is not stoichiometric, indicating that there is some uncertainty in the occupancy of the atomic positions, similar to Re_3W [75].

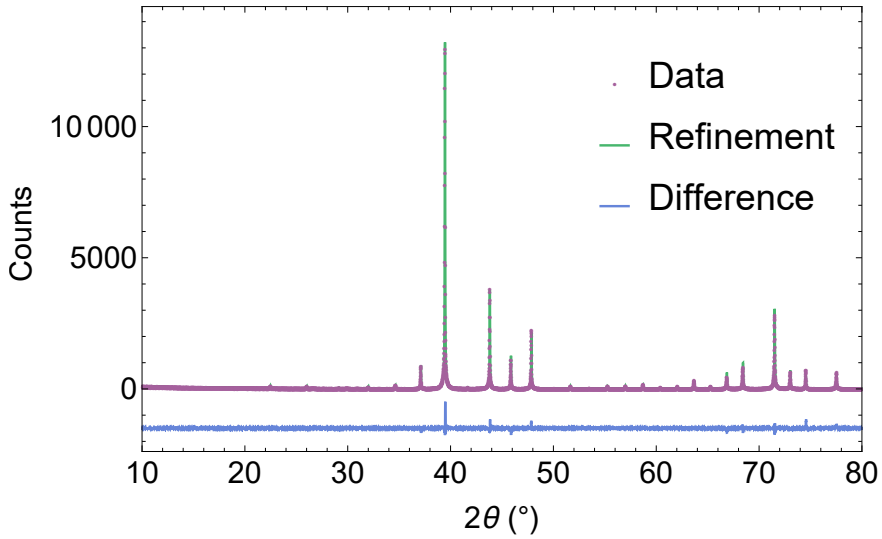

Fig. 5.2 Powder-XRD data for the Re_3Ta sample, with a refinement to a single phase with the non-centrosymmetric α-Mn structure.

Table 5.1 Crystallographic parameters obtained from the structural Rietveld refinement of the room-temperature powder XRD data of Re_3Ta. The goodness of fit is 1.314.

Structure		α-Mn noncentrosymmetric		
Space-group		$I\,\bar{4}\,3\,m$ (No. 217)		
Lattice parameters				
	a (Å)	9.69067(3)		
	V_{cell} (Å^3)	910.042(8)		
Atom	Wyckoff Position	x	y	z
Re1	2a	0	0	0
Re2	24g	0.3583(2)	0.3583(2)	0.0440(2)
Re3	24g	0.0901(2)	0.0901(2)	0.2823(2)
Ta1	8c	0.3185(3)	0.3185(3)	0.3185(3)
Ta2	24g	0.3583(2)	0.3583(2)	0.0440(2)

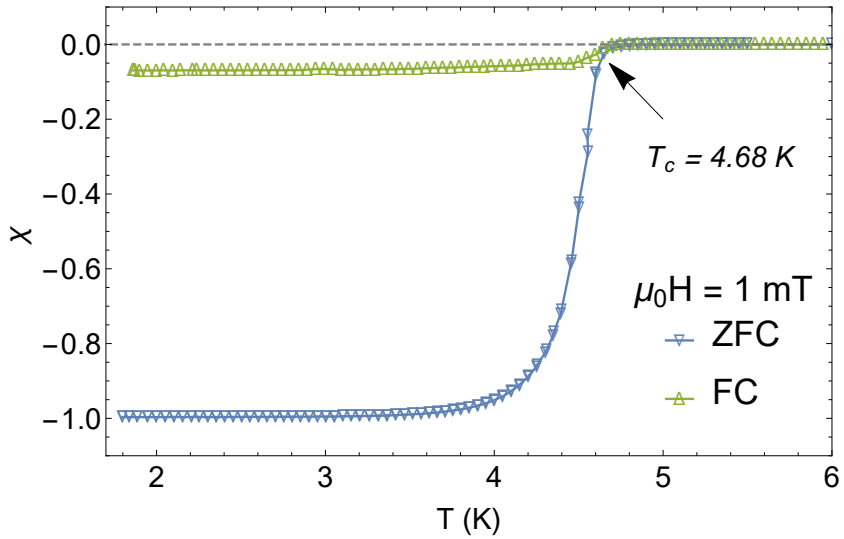

Fig. 5.3 Temperature dependence of the magnetic susceptibility, collected via zero-field cooled (ZFC) and field cooled (FC) methods under an applied field of 1 mT.

5.4 Magnetization

A Quantum Design 5 T MPMS was used to measure the low temperature magnetic susceptibility. Figure 5.3 shows the recorded $\chi(T)$ data measured under an applied field of 1 mT. Both zero-field cooled and field-cooled regimes exhibit a clear diamagnetic signal at $T_c = 4.68$ K. The data have been corrected for the demagnetizing effect of the sample geometry, and are consistent with a 100% Meissner volume fraction. The field-cooled data do not return to perfect diamagnetism, indicating that a portion of magnetic flux is pinned within the body of the superconductor.

The field dependent magnetization was measured using an Oxford Instruments Vibrating Sample Magnetometer. Figure 5.4(a) displays low-induction magnetization against field data after correcting for demagnetization. Below H_{c1}, the sample is a perfect diamagnet, and the magnetic response is linear with gradient $M/H = -1$. Above H_{c1}, flux begins to penetrate the sample, and the magnetization response begins to deviate from linearity. In order to more accurately determine this point, the deviation from linearity ΔM was calculated. H_{c1} was taken as the point at which ΔM crossed a threshold value of $2\,\mathrm{A\,m^{-1}}$. A power-law model of the form

$$H_{C1}(T) = H_{C1}(0)\left[1 - \left(\frac{T}{T_c}\right)^{\delta}\right] \tag{5.1}$$

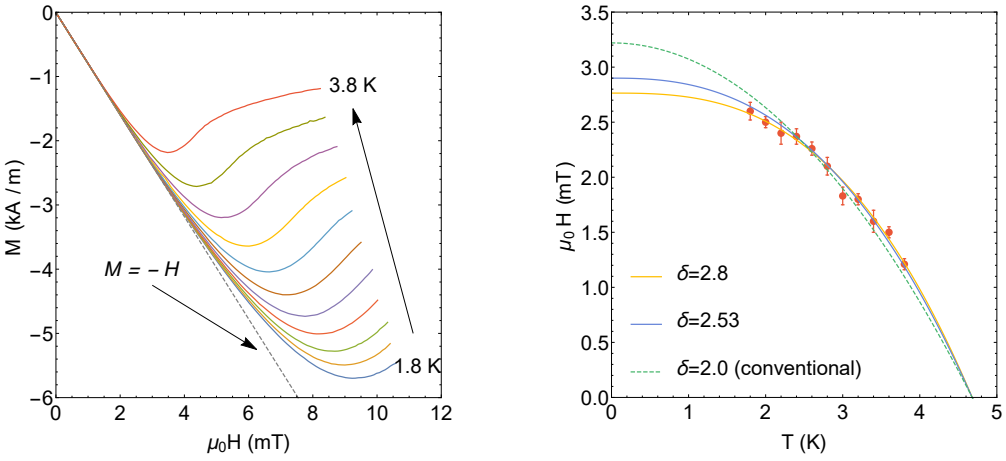

(a) (b)

Fig. 5.4 Determination of H_{c1} from magnetization measurements. (a) Field dependence of the magnetization at a range of temperatures after cooling in zero field. The applied field has been corrected for demagnetization effects. (b) Temperature dependence of the lower critical field H_{c1} determined from low-field magnetic hysteresis measurements. The dashed line shows the conventional power law behaviour, where the solid lines are the results of fitting to Eq. (5.1) as described in the text.

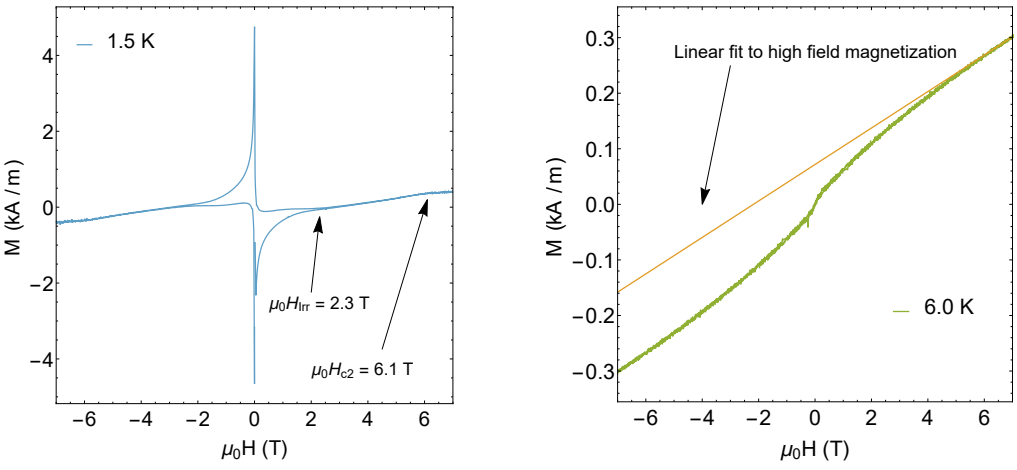

(a) (b)

Fig. 5.5 Field dependence of magnetization collected above and below $T - c$. (a) Field loop at $T = 1.5\,\mathrm{K}$, in the superconducting state. (b) Normal state magnetization at $T = 6\,\mathrm{K}$.

Table 5.2 Summary of the superconducting properties of Re_3Ta determined from magnetization measurements.

T (K)	H_{c1} (mT)	H_{c2} (T)	$\xi(T)$ (nm)	$\lambda(T)$ (nm)	$\kappa(T)$
1.8	2.6(3)	5.8(1)	7.48(6)	510(30)	68(4)
2.2	2.4(3)	5.0(1)	8.05(4)	530(30)	66(4)
2.6	2.3(2)	4.5(2)	8.5(1)	550(30)	64(4)
3.0	1.8(2)	3.8(1)	9.2(1)	610(30)	66(4)
3.4	1.6(2)	5.1(1)	10.2(2)	650(30)	64(4)
3.8	1.2(1)	2.32(8)	11.8(2)	750(40)	63(3)

was used to provide an estimate for the lower critical field of $\mu_0 H_{c1}(0) = 2.76(5)$ mT, with the power $\delta = 2.8(1)$ (see Fig. 5.4(b)). This is larger than the conventional value of $\delta = 2.0$. The data are also well described by Eq. (5.1) with α fixed to the conventional value, and this yields a higher value of $\mu_0 H_{C1}(0) = 3.22(6)$ mT, however the fit is better with the parameter left free. Therefore our estimation for the lower critical field is $\mu_0 H_{C1}(0) = 2.76(5)$ mT.

Figure 5.5 presents high-induction magnetization hysteresis loops, collected at temperatures of 1.5 K and 6.0 K. The magnetic behaviour becomes irreversible below $\mu_0 H_{Irr} = 2.3$ T, above which point the applied field becomes strong enough to de-pin vortices. The transition to the normal state is apparent as a subtle change of gradient at a much higher field of $\mu_0 H_{C2} = 6.1$ T. Solving Eqs. (2.12) and (2.13) simultaneously allows estimates for the penetration depth and coherence length to be made for the temperatures studied. The results of this are presented in Tab. 5.2. The average value of the Ginzburg-Landau parameter is $\kappa = 65(4)$, and so we can classify Re_3Ta as a strongly type-II superconductor. This is typical of other members of this family of superconductors, for example, in noncentrosymmetric Re_3W $\kappa = 50(1)$ [72].

The data collected in the normal state just above T_C have been fitted to the model:

$$M(H) = N\mu \tanh\left(\frac{\mu H}{k_B T}\right) + \chi H, \tag{5.2}$$

where the first term is the Langevin paramagnetic equation for a two level spin system, and the second term provides the intrinsic volume magnetic susceptibility χ. The assumption of a two spin system is justified by the observation of a Schottky anomaly in the heat capacity at high applied magnetic fields. Fitting the data in this manner yields $N = 31.4(7)$ f.u.$^{-1}$ with an associated magnetic mo-

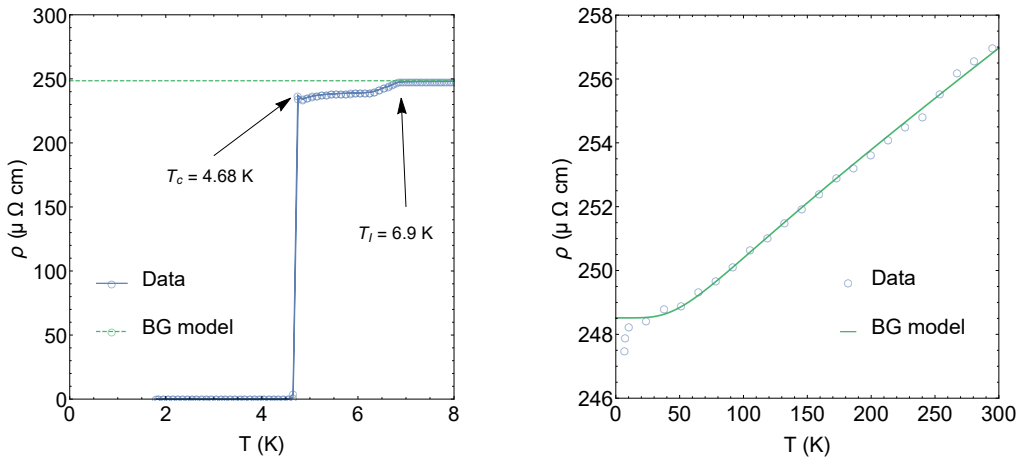

Fig. 5.6 Temperature dependence of the resistivity in zero field. (a) Superconducting transition at $T_C = 4.7$ K. The dashed line is the extrapolated Bloch-Grüneisen model showing the residual resistivity. A small superconducting impurity is apparent at $T_I = 6.9$ K, the significance of which is discussed in the text. (b) The normal state resistivity, which indicates that Re_3Ta is a poor metal. The solid line is the result of the fit to the Bloch-Grüneisen model.

ment $\mu = 8.7(1) \times 10^{-6}\ \mu_B$, and the dimensionless intrinsic volume susceptibility $\chi^{SI} = 4.75(1) \times 10^{-5}$.

5.5 Electrical Resistivity

Electrical properties were measured using a Quantum Design 7 T PPMS, using an AC transport option as described in Sec. 3.3. The resistivity of Re_3Ta as a function of temperature for $1.8\,K \leq T \leq 300\,K$ in zero applied field is shown in Fig. 5.6. A sharp superconducting transition is observed at $T_c = 4.7$ K, with a width $\Delta T_C \leq 0.1$ K. There is a small dip in the resistivity at $T_I = 6.9$ K, which is most likely due to the presence of a small amount of superconducting impurity with a higher transition temperature than the bulk material. No sign of this fraction has been observed in magnetization, heat capacity, or our μSR results, and there was no sign of a secondary phase in the powder XRD spectrum. We therefore conclude that the results presented here are indicative of the majority α-Mn phase of Re_3Ta, and that the impurity content is negligible. The effect on T_c of applying a magnetic field is shown in Fig. 5.7. T_C is suppressed and the width of the superconducting transition increases as the magnitude of the applied field is increased.

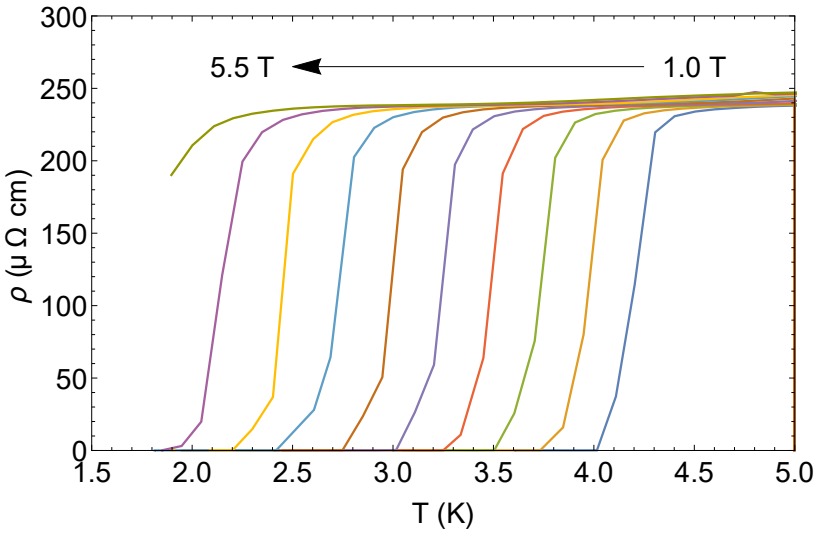

Fig. 5.7 Effect of applying magnetic fields of varying strengths on T_c. The fields were applied in the range 1 T to 5.5 T, in steps of 0.5 T.

It is noteworthy that the value of $T_I = 6.9\,K$ is extremely close to the value of $T_c = 6.78\,K$ reported for this material in the original paper by Blaugher and Hulm. [53] As there is no temperature dependent data presented in the original work, it is likely that a similar impurity content produced a misleading value for the bulk transition temperature. A similar issue occurred in the study of Re_3W, [75] in which the Blaugher paper reports a value of 9 K for the superconducting transition temperature of the noncentrosymmetric phase. In fact, this is closer to the value of 9.4 K reported in the phase-pure centrosymmetric Re_3W compound, with the noncentrosymmetric structure becoming superconducting at the lower temperature of 7.8 K. If a similar mechanism is at play in this system, then it suggests that T_I corresponds to the superconducting transition temperature of a centrosymmetric form of Re_3Ta, which exists as a small impurity phase in our sample.

In the normal state, Re_3Ta is a poor metal, with a shallow negative gradient for ρ observed upon cooling from room temperature - see Fig. 5.6(b). At 300 K, the resistivity is $257(1)\,\mu\Omega\,cm$, flattens off to a residual value of $\rho_0 = 248.5(30)\,\mu\Omega\,cm$ by 10 K. These values yield a residual resistivity ratio (RRR) of 1.04(1). This low value for the RRR coupled with the high residual resistivity is similar to the NCS Re_3W. It is likely that a combination of strong electronic scattering, with a large temperature independent resistivity due to the intrinsic disorder in the Re and Ta occupancies is responsible for the poor conductivity. The $\rho(T)$ data above T_C are well described by the Bloch-Grüneisen (BG) model of resistivity (discussed in Sec. 2.7.3) where acoustic lattice vibrations scatter conduction electrons. [38]

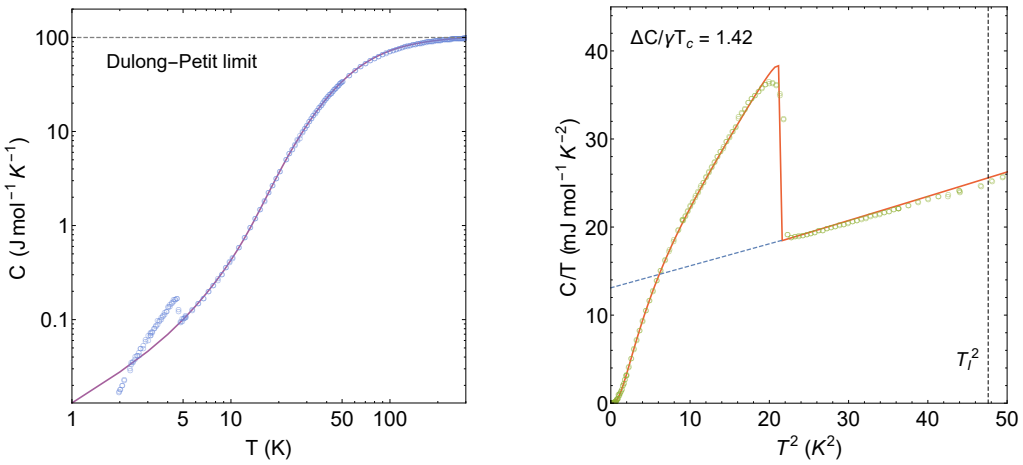

(a) (b)

Fig. 5.8 (a) Temperature dependence of the heat capacity in zero-field plotted on a log-log scale, with a fit to Eq. (2.61). (b) Detail of the superconducting discontinuity, presented as C/T against T^2. The solid line is the result of the fit to a single-gap isotropic BCS model. The dashed line is the extrapolation to $T = 0$, where the intercept gives $\gamma = 13.1$. The position of T_I^2 is also marked.

The data have been fitted using Eqs. (2.72) and (2.73), yielding the fit parameters $\rho_0 = 248.52(2)\,\mu\Omega\,\text{cm}$, $\Theta_R = 300(4)\,\text{K}$, and $r = 8.9(1)\,\mu\Omega\,\text{cm}$. Θ_R is an estimate of the Debye temperature from the resistivity data, and r is a material dependent constant.

5.6 Heat Capacity

Zero-field heat capacity, C, data collected in the temperature range $0.3\,\text{K} \leq T \leq 300\,\text{K}$ are displayed in Fig. 5.8(a). The heat capacity in the normal state has been calculated over the full temperature range using Eqs. (2.61)-(2.64), with the fit parameters presented in Tab. 5.3. The Debye temperature calculated in this way is in reasonable agreement with the estimate of $\Theta_R = 300(4)$ from the BG model applied to the resistivity data. At high temperatures, the total heat capacity approaches the Dulong-Petit limit of $3pR = 99.8\,\text{J mol}^{-1}\,\text{K}^{-1}$, where R is the gas constant and $p = 4$ is the number of atoms per formula unit [34].

Figure 5.8(b) displays a close-up of the superconducting heat capacity discontinuity in zero-field. There is a sharp transition at $T_c = 4.68\,\text{K}$, indicating the bulk nature of the superconductivity. No discontinuity is apparent at $T_I = 6.9\,\text{K}$, which supports the view that the superconducting impurity observed in the electrical resistivity is

Table 5.3 Summary of the superconducting and normal state properties of Re_3Ta determined from heat capacity measurements. Reported values for Re_3W from Ref. [75] are also presented for comparison.

Property	Re_3Ta (present work)	Re_3W [75]
Normal state		
γ (mJ mol^{-1} K^{-2})	13.1(2)	15.9(6)
Θ_D (K)	284.2(2)	228(6)
Θ_E (K)	123.4(3)	292(15)
N_D/N_E	6.84(5)	-
Superconducting state		
T_c (K)	4.68(2)	7.80(5)
α_{HC}	1.83(2)	1.85(2)
λ_{ep}	0.64(3)	0.83(4)

negligibly small, and as such the results presented here are representative of the majority α-Mn Re_3Ta phase. The peak of the transition is slightly rounded below T_C. An estimation of the magnitude of the change in heat capacity immediately before and after becoming superconducting is $\Delta C/\gamma T_C = 1.49 \pm 0.05$, taking into account the uncertainty in the exact position of the peak. This is slightly larger than the BCS expectation of 1.426 for superconductivity in the weak coupling limit.

The low temperature heat capacity data were modelled using Eqs. (2.66)-(2.68), with the result represented by the solid line in the figure. Under the alpha model, this yields a value of the parameter $\alpha_{HC} = 1.83(1)$, which is larger than the BCS value of $\alpha_{BCS} = 1.764$. This is also consistent with the value estimated from the magnitude of the discontinuity using Eq. (2.69), which yields $\alpha_{HC} = 1.80(2)$ using the values of γ and ΔC given in the preceding paragraphs. Thus the shape of the temperature dependence and the magnitude of the discontinuity are well described by a BCS model for a single-gap, isotropic superconductor.

Figure 5.9(a) shows the effect of applying a field on the superconducting transition in heat capacity. The general shape of the transition stays the same, and T_c is suppressed further from the zero-field value as the field is increased. Also apparent is the increase of the intercept at $T = 0$ as the applied field strength is increased. A plot of the field variation of the intercept, $\gamma(H)$, is presented in Fig. 5.9(b), where the data have been estimated from linearly extrapolating the measured heat capacity. It can be seen that $\gamma(H)$ varies approximately linearly with increasing field, which is expected for nodeless superconductors [76]. In the presence of nodes the density of

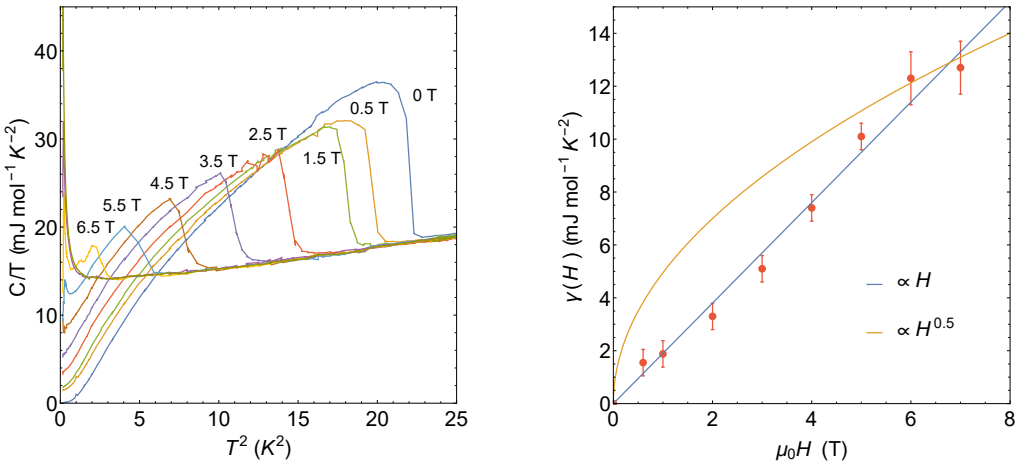

(a) (b)

Fig. 5.9 (a) Field dependence of the heat capacity at the superconducting transition, showing the suppression of T_C with increasing field. (b) Field dependence of γ, extracted from linear extrapolation of low temperature heat capacity.

states, and therefore γ, is expected to vary as the square root of the applied field [77]. This suggests that Re_3Ta is a conventional *s*-wave superconductor.

At high magnetic fields ($\mu_0 H > 6\,\mathrm{T}$) there is a evidence of a Schottky anomaly, which arises due to spin states in paramagnetic systems becoming frozen out at low temperatures (see Fig. 5.10). The Schottky contribution to the heat capacity may be modelled by the addition of a term [78]

$$C_{\mathrm{Sch}} = n\left(\frac{E_g(H)}{k_B T}\right)^2 \frac{\exp(E_g(H)/k_B T)}{(1+\exp(E_g(H)/k_B T))^2}. \tag{5.3}$$

Here n is the concentration of paramagnetic centres, and

$$E_g(H) = g\mu_B\sqrt{H^2+H_0^2} \tag{5.4}$$

is the Zeeman energy of the two energy levels, with g the Landé factor, and H and H_0 the magnitudes of the applied and crystal fields, respectively. Fitting the low temperature heat capacity collected at 7 T and 9 T, we find estimates for the energy gap of $E_g(7T) = 25.6\,\mu\mathrm{eV}$ and $E_g(9T) = 29.9\,\mu\mathrm{eV}$. Solving Eq. (5.4) simultaneously for these two values then yields estimates of $g = 0.05$ and $H_0 = 6.4\,\mathrm{T}$. In order to obtain better estimates of these parameters, it would be necessary to measure the heat capacity at much higher fields, as only a portion of the Schottky peak is observed at 9 T.

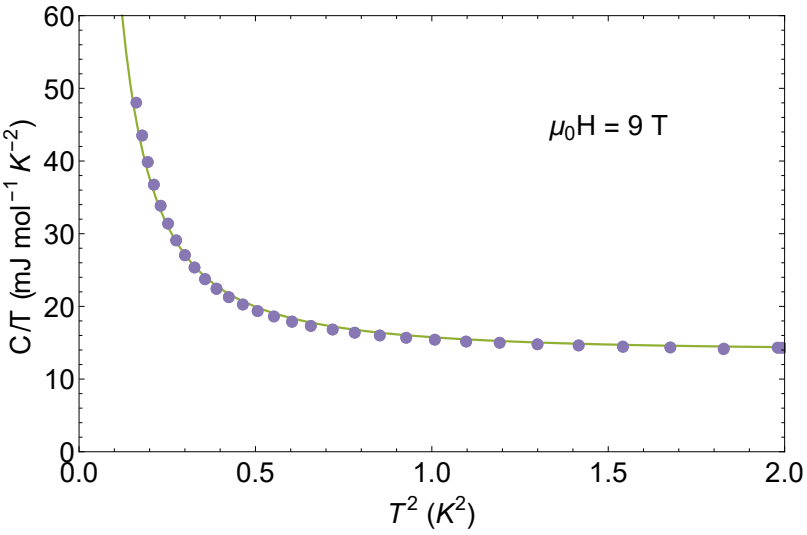

Fig. 5.10 Detail of the low temperature heat capacity in an applied field of 9 T. The superconductivity is completely suppressed, and there is evidence of a Schottky anomaly. The solid line is a fit assuming the anomaly is caused by paramagnetic centres with two energy levels given by Zeeman splitting.

5.7 Muon-spin Rotation & Relaxation

5.7.1 Zero-field

Muon spin rotation and relaxation experiments have also been carried out in order to further understand the superconducting nature of this material. Muon spin relaxation measurements in zero-field can be used to detect the tiny spontaneous magnetization associated with broken time-reversal symmetry in the superconducting state. The ZF-μSR spectra collected above and below T_c presented in Fig. 5.11 do not exhibit a noticeable difference when the sample is superconducting, indicating that time-reversal symmetry is preserved in Re_3Ta. Depolarization of the initially 100% spin-polarized muon ensemble occurs because of the randomly oriented array of nuclear dipole moments, as well as electronic spin fluctuations. The nuclear relaxation component is modelled by the Gaussian Kubo-Toyabe equation [49]

$$G_{\mathrm{KT}}(t) = \frac{1}{3} + \frac{2}{3}(1-\sigma_{\mathrm{ZF}}^2 t^2)\exp\left(-\frac{\sigma_{\mathrm{ZF}}^2 t^2}{2}\right), \tag{5.5}$$

where σ_{ZF} measures the width of the nuclear dipolar field experienced by the muons. The asymmetry spectra are well described by the function

$$A(t) = A_1 G_{\mathrm{KT}}(t)\exp(-\Lambda t) + A_{\mathrm{BG}}, \tag{5.6}$$

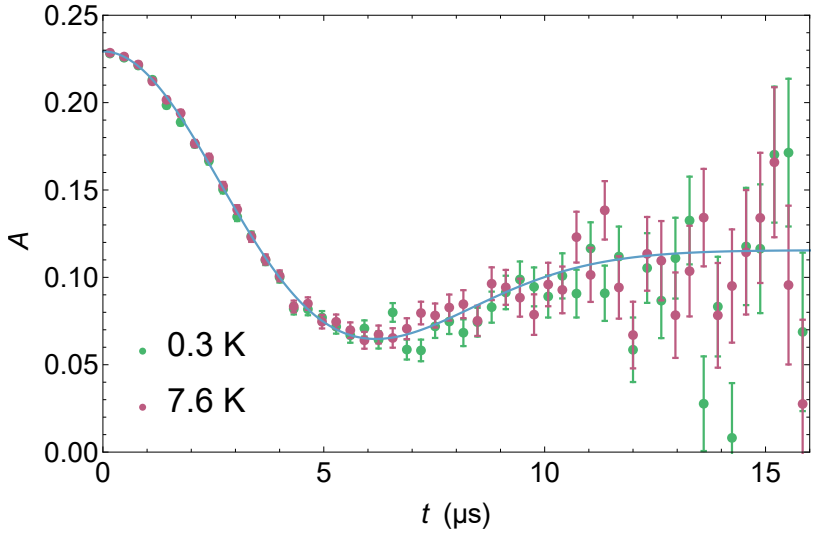

Fig. 5.11 Muon spin relaxation spectra collected in zero-field above and below the superconducting transition temperature. The solid line is the result of a fit to Eq. (5.6). The data bin sizes have been increased by a factor of 10 in order to improve the clarity of the figure.

where A_1 is the sample asymmetry, A_{BG} is the time independent background contribution from muons stopped in the silver sample holder, and Λ measures the electronic relaxation rate that is usually attributed to 'fast-fluctuation' effects that occur on a timescale much shorter than the muon lifetime. Both high and low temperature datasets are found to be well described by Eq. (5.6) with the fit parameters $A_1 = 0.1706(4)$, $A_{\mathrm{BG}} = 0.0600(8)$, $\sigma_{\mathrm{ZF}} = 0.278(2)\,\mu\mathrm{s}^{-1}$ and $\Lambda = 0.010(3)\,\mu\mathrm{s}^{-1}$ (solid line in Fig. 5.11).

5.7.2 Transverse field

TF-μSR was performed in the field range $10\,\mathrm{mT} \leq \mu_0 H \leq 50\,\mathrm{mT}$. Typical asymmetry spectra collected above and below T_c in a field of 30 mT is displayed in Fig. 5.12. The enhanced depolarization rate below T_c is due to the field distribution, $P(B)$, formed by the flux line lattice in the mixed state of the superconductor. Measuring the width of this field distribution allows the magnetic penetration depth, λ, to be calculated, as discussed in Sec. 2.2.1. The TF spectra are modelled as a sum of n sinusoidal oscillations, each within a Gaussian relaxation envelope:

$$G_x(t) = \sum_{i=1}^{n} A_i \exp\left(-\frac{\sigma_i^2 t^2}{2}\right) \cos(\gamma_\mu B_i t + \phi), \tag{5.7}$$

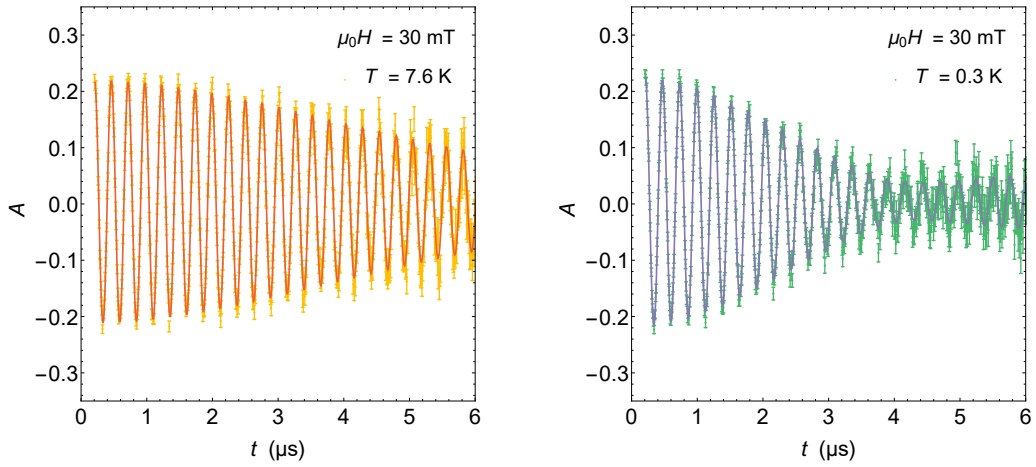

(a) (b)

Fig. 5.12 Representative TF-μSR signals collected (a) above and (b) below T_c in Re_3Ta under an applied magnetic field of 30 mT. The solid lines are fits using Eq. (5.7).

where A_i is the initial asymmetry, σ_i is the Gaussian relaxation rate, and B_i is the first moment of the i'th component in the field distribution. There is a phase offset ϕ, which is shared by each oscillating component, and $\gamma_\mu/2\pi = 135.5\,\mathrm{MHz\,T^{-1}}$ defines the muon gyromagnetic ratio. Our sample was modelled well with $n = 2$, where the depolarization rate of the second component σ_2 was fixed to 0 during the fitting process to account for the non-depolarizing muons that stop in the silver sample holder. In this case, the second moment of the sample is completely determined by $\sigma_1 = \sigma$. Figure 5.13 displays the extracted temperature dependence of the fit parameters σ and $B_{1,2}$.

In order to isolate the depolarization due to the flux line lattice, the broadening due to nuclear dipolar fields, σ_N, must be subtracted in quadrature from the measured depolarization rate, σ:

$$\sigma_{FLL}^2 = \sigma^2 - \sigma_N^2. \tag{5.8}$$

σ_N is assumed to be temperature independent, and is determined by measurements made in the normal state just above T_c. Because $\kappa \gg 5$ and $H/H_{c2} \ll 1$ in this material, no field dependence of the depolarization rate is expected. In this regime, a simple numerical pre-factor relates the second moment of the vortex lattice field distribution and the inverse squared magnetic penetration depth, i.e. $\sigma_{FLL} \propto \lambda^{-2}$. Therefore, σ_{FLL} is directly related to the superfluid density by the equation

$$\frac{\sigma_{FLL}(T)}{\sigma_{FLL}(0)} = \frac{\lambda^{-2}(T)}{\lambda^{-2}(0)}. \tag{5.9}$$

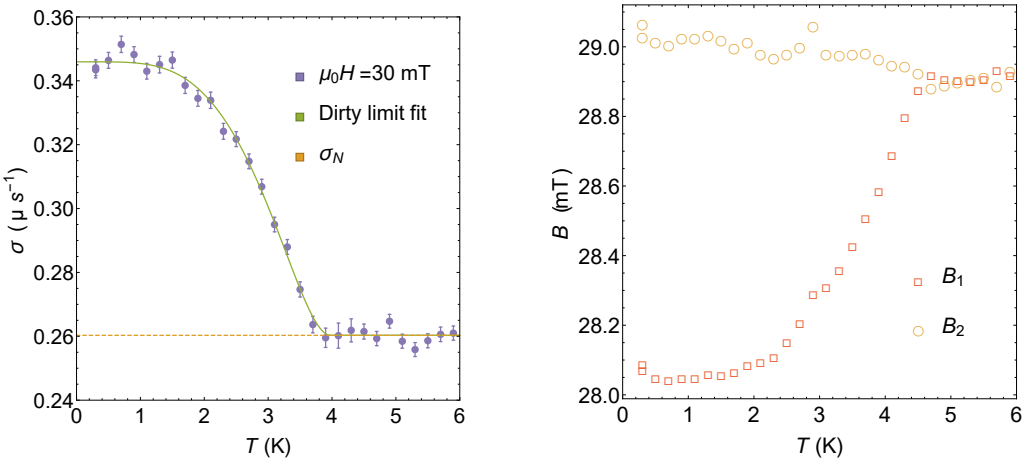

Fig. 5.13 (a) Temperature dependence of the muon spin depolarization rate, collected after field cooling in an applied field of 30 mT. (b) Temperature dependence of the associated field parameters, $B_{1,2}$.

Combining these equations with the expression for the superfluid density in the dirty limit (Eq. (2.71)) provides a model for the temperature dependence of the measured depolarization rate below T_c:

$$\sigma(T) = \sqrt{\sigma_{\mathrm{FLL}}^2(0)\frac{\Delta^2(T)}{\Delta^2(0)}\tanh^2\left[\frac{\Delta(T)}{2k_BT}\right] + \sigma_N^2}. \tag{5.10}$$

The four adjustable parameters are $\sigma_{\mathrm{FLL}}(0)$, Δ_0, T_c and σ_N. The results of applying this model to the data of Fig. 5.13(a) are presented in Tab. 5.4.

The magnitude of the superconducting energy gap leads to a value of $\alpha_\mu = 2.1(2)$ This is much larger than the BCS value of 1.724, and is also larger than the estimate from the heat capacity, $\alpha_{\mathrm{HC}} = 1.83(2)$. The zero-temperature value of λ can be estimated directly from the value of $\sigma_{\mathrm{FLL}}(0)$ using the relation (*c.f.* Eq. 2.17):

$$\frac{\sigma_{\mathrm{FLL}}^2(0)}{\gamma_\mu^2} = 0.00371\frac{\Phi_0^2}{\lambda^4(0)} \tag{5.11}$$

to give $\lambda = 686(3)$ nm. This is much larger than the value that seems to be suggested by the magnetization calculations presented in Tab. 5.2. This discrepancy is discussed further in Sec. 5.8.3.

A puzzling feature of the fit results is the suppressed value of $T_c = 3.97(7)$ K. Figures 5.14 (a)-(e) show the measured temperature dependences of σ in applied fields of 10 mT to 50 mT. Upon inspection, it can be seen that σ_1 is approximately field independent above 10 mT, which is to be expected for high-κ superconductors

Table 5.4 Results of fitting the depolarization rate collected in 30 mT to the model of Eq. (5.10).

Property	Value
$\sigma_{\mathrm{FLL}}(0)$ ($\mu\mathrm{s}^{-1}$)	0.228(2)
T_{c} (K)	3.97(7)
Δ_0 (meV)	0.83(7)
$\alpha_\mu \equiv \Delta_0/k_{\mathrm{B}}T_{\mathrm{c}}$	2.1(2)
σ_{N} ($\mu\mathrm{s}^{-1}$)	0.2603(7)

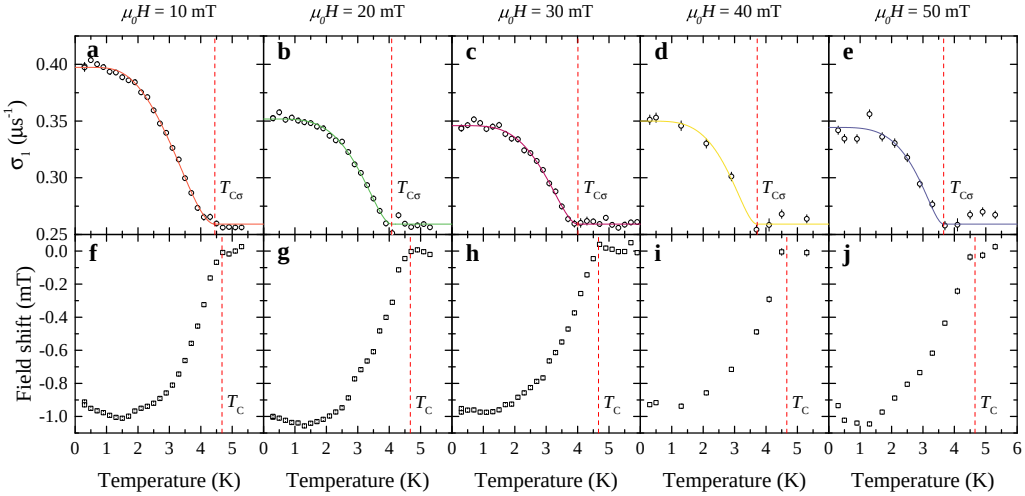

Fig. 5.14 (a)-(e) Temperature dependence of σ_1 over the range of fields studied. (f)-(j) Temperature dependence of the internal field shift due to flux expulsion inside the superconductor.

in the low-field limit. Close to $H_{\mathrm{c1}} = 2.90(7)$ mT the depolarization rate is expected to increase in value. It is clear from the figure that the onset temperature $T_{\mathrm{c}\sigma}$ at each field does not appear to coincide with $T_{\mathrm{c}} = 4.68$ K. This cannot be accounted for by the suppression of T_{c} with field, as H_{c2} is several orders of magnitude larger than the applied field. Evidence that the sample does indeed enter the superconducting state at the correct temperature is evidenced from the field shift $\Delta B = B_1 - B_2$, which is displayed in Fig. 5.14(f)-(j). A clear diamagnetic shift occurs at $T_{\mathrm{c}} \approx 4.68$ K for all fields measured. Therefore, the apparent onset temperature in the depolarization data does not necessarily correspond to the superconducting transition temperature. This is discussed further in Sec. 5.8.3.

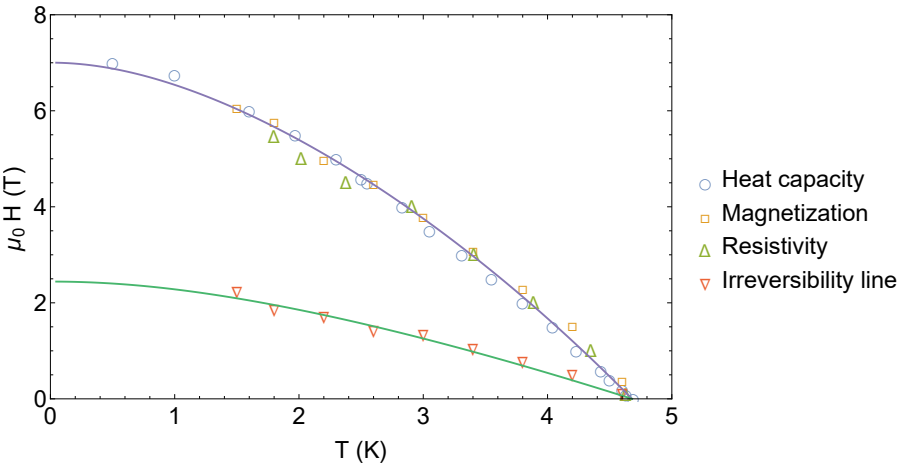

Fig. 5.15 Determination of the upper critical field via resistivity, magnetization and heat capacity measurements. Also shown is the irreversibility line, below which the magnetization hysteresis becomes irreversible. The solid lines are WHH fits as described in the text.

5.8 Discussion

5.8.1 Critical field calculations

The T-dependence of the upper critical field as determined from measurements of $M(H)$, C, and ρ, is shown in Fig. 5.15. The data were modelled under the WHH theory, which takes into account the effect of Pauli limiting and spin-orbit scattering of quasiparticles on H_{c2}. The result of the fit is shown as the solid line in Fig. 5.15, and yields a value for the Maki parameter of $\alpha_M = 1.31(4)$, with $\lambda_{SO} = 1.3(4)$. The upper critical field at $T = 0\,\mathrm{K}$ is thus found to be $\mu_0 H_{c2}(0) = 7.0(2)\,\mathrm{T}$. The spin-orbit scattering time τ_{SO} can be calculated from the fitted spin-orbit scattering parameter $\lambda_{SO} = \hbar/(3\pi k_B T_C \tau_{SO})$ which produces $\tau_{SO} = 0.13(3)\,\mathrm{ps}$. $0.97(3)\,\mathrm{T}$. The validity of using the WHH theory for this sample is shown by evaluating Eq. (2.60). A linear fit to the upper critical field in the vicinity of T_c yields $dH_{c2}/dT = -2.3\,\mathrm{T\,K^{-1}}$, which results in the WHH estimate of $\alpha_M = 1.2$. As this is close to the value of the fitted parameter, the WHH theory is valid, and we can infer that the superconductivity in La_7Ir_3 is in the dirty limit. This is backed up by the large residual resistivity, and small RRR in this sample. The extent of the dirty limit is quantified in a later section.

The Maki parameter measures the relative contributions of the orbital and Pauli-limiting de-pairing mechanisms on the measured upper critical field. Using Eqs. (2.56) and (2.57), the Pauli limiting field in the dirty limit is found to be $\mu_0 H_P(0) = 9.03\,\mathrm{T}$, with the orbital limit $\mu_0 H_{c2}^{Orb}(0) = 8.4\,\mathrm{T}$. The observed upper

critical field, $\mu_0 H_{c2}(0) = 7.0(2)$ T, is evidently smaller than both of these fields. The maximum field is also suppressed due to spin-orbit scattering.

An estimate for the thermodynamic critical field can now be made using the α model relation [32]

$$\frac{H_C(0)}{\sqrt{\gamma_{NV} T_C^2}} = \sqrt{\frac{6}{\pi}}\alpha. \tag{5.12}$$

where γ_{NV} is the Sommerfeld coefficient per unit volume, and is calculated from the molar volume in units of erg cm^{-3} K^{-2}. For Re_3Ta, $\gamma_{NV} = (3470(50))$ erg cm^{-3} K^{-2}, leading to $\mu_0 H_C(0) = 69.7(9)$ mT.

The Ginzburg-Landau parameter κ_{GL} is related to H_C and H_{C2} by the relation

$$\kappa_{GL} = \frac{H_{C2}}{\sqrt{2} H_C}, \tag{5.13}$$

which using $H_{C2}(0) = 7.0(2)$ T and $H_C(0) = 69.7(9)$ mT yields $\kappa_{GL} = 71(2)$. This classifies Re_3Ta as a strong type-II superconductor, as this is many times greater than the threshold value of $\kappa_{GL} = 1/\sqrt{2}$. The lower critical field H_{C1} is obtained from κ_{GL} and H_C using the equation

$$H_{C1} = H_C \frac{\ln \kappa_{GL}}{\sqrt{2}\kappa_{GL}}, \tag{5.14}$$

and using the above values we find $H_{C1} = 2.95(8)$ mT. This is in excellent agreement with the values previously estimated from magnetization measurements, and in fact, fixing the value of $H_{C1}(0)$ in Eq. (5.1) to this calculated value and refitting the data yields the best description of the data, with the power $\delta = 2.53(5)$ (*c.f.* Fig. 5.4 in Section 5.4). The characteristic Ginzburg-Landau coherence length at $T = 0$ K, $\xi(0)$, is obtained from

$$H_{C2}(0) = \frac{\Phi_0}{2\pi\xi^2(0)} \tag{5.15}$$

where $\Phi_0 = 2.068 \times 10^{-15}$ Wb m^{-2} is the magnetic flux quantum. For $H_{c2} = 7.0(2)$ T, $\xi(0) = 6.86(10)$ nm. The effective penetration depth at $T = 0$, $\lambda(0)$, can be estimated from the calculation of $H_c(0)$ and the measured $H_{C2}(0)$ by

$$\lambda^2 = \frac{\Phi_0 H_{C2}(0)}{4\pi H_C^2(0)}, \tag{5.16}$$

which gives the value $\lambda = 487(9)$ nm. This calculation is consistent with the values for λ derived from the measured upper and lower critical fields presented in Tab. 5.2.

Table 5.5 Properties of the critical fields in Re_3Ta.

Property	Unit	Value
$\mu_0 H_{c2}(0)$	T	7.0(2)
α_M		1.31(4)
λ_{SO}		1.3(4)
$\mu_0 H_P(0)$	T	9.0
$\mu_0 H_{c2}^{Orb}(0)$	T	8.4
$\mu_0 H_c(0)$	mT	69.7(9)
$\mu_0 H_{c1}(0)$	mT	2.95(8)
$\xi(0)$	nm	6.86(10)
λ	nm	487(9)

However, it is much smaller than the value estimated from the μSR experiments, where $\lambda = 686(3)$ nm. Possible explanations for this are discussed in Sec. 5.8.3.

5.8.2 Microscopic properties of the superconducting state

In order to find a self-consistent description of the microscopic properties of Re_3Ta, the results of resistivity, heat capacity, and magnetization measurements can be combined. The Sommerfeld constant, γ, determined from low temperature heat capacity, is related to the electronic properties of the system by the equation

$$\gamma = \left(\frac{\pi}{3}\right)^{2/3} \frac{k_B^2 m^* n^{1/3}}{\hbar^2}, \tag{5.17}$$

where m^* is the effective mass of quasiparticles, and n is the quasiparticle number density per unit volume. A closely related property is the London penetration depth, which is defined by the normal state properties:

$$\lambda_L = \left(\frac{m^*}{\mu_0 n e^2}\right)^{1/2}. \tag{5.18}$$

In the clean limit, it is possible to use measured values of λ and γ from μSR and heat capacity measurements to simultaneously solve these equations to find m^* and n.

In Re_3Ta, we suspect that we are in the dirty limit. The evidence for this primarily comes from the resistivity measurements; however the suppression of H_{c2} due to scattering from the orbital limit is further evidence of dirty limit superconductivity. As discussed in Sec. 2.5, the ratio of the BCS coherence length to the electronic mean

Table 5.6 Electronic properties of Re_3Ta.

Property	Unit	Value
m^*/m_e		12.6
n	$10^{27}\,m^{-3}$	5.04
ξ_0	nm	4.13
l_e	nm	1.75
ξ_0/l_e		2.36
λ_L	nm	266
v_F	$m\,s^{-1}$	48 600

free path, ξ_0/l_e, has important ramifications on the superconductivity. In dirty limit superconductors, this ratio is larger than unity, and therefore scattering of electrons in Cooper pairs is expected to interfere with the superconducting ground state. One consequence is that the penetration depth is expected to be longer than the (ideal) London penetration depth, where the effective penetration depth at $T = 0$ is given by

$$\lambda(0) = \lambda_L \left(1 + \frac{\xi_0}{l_e}\right)^{1/2}. \tag{5.19}$$

The electrical mean free path can be estimated from the residual resistivity, ρ_0, by the equation

$$l_e = \frac{3\pi^2\hbar^3}{e^2\rho_0 m^{*2} v_F^2}, \tag{5.20}$$

where the Fermi velocity is related to the effective mass and the carrier density by

$$n = \frac{1}{3\pi^2}\left(\frac{m^* v_F}{\hbar}\right)^3. \tag{5.21}$$

Finally, a relationship between the BCS coherence length, the mean free path, and the Ginzburg-Landau coherence length at $T = 0$, $\xi(0)$, is given by [33]

$$\frac{\xi(0)}{\xi_0} = \frac{\pi}{2\sqrt{3}}\left(1 + \frac{\xi_0}{l_e}\right)^{1/2}. \tag{5.22}$$

Equations (5.17)-(5.22) form a system of four equations, which can be simultaneously solved for the parameters m^*, n, l_e, and ξ_0. This was carried out using the Solve routine in the Mathematica software, where the measured values $\gamma = 13.1\,mJ\,mol^{-1}\,K^{-2}$, $\lambda(0) = 487\,nm$, $\xi(0) = 6.86\,nm$, and $\rho_0 = 248.5\,\mu\Omega\,cm$ have been used. The results are presented in Tab. 5.6.

The BCS coherence length calculated in this manner is larger than the electronic mean free path, with $\xi_0/l_e = 2.36$. This justifies our previous suspicion that superconductivity in Re_3Ta occurs in the dirty limit, and thus should be modelled with the appropriate equations. The low value for the mean free path reflects the intrinsic disorder in the structure of this material, and accounts for the low RRR and ρ_0 that have been measured. The effective mass is rather large, and using $\lambda_{el-ph} = 0.64$ yields a value for the bare band-structure effective mass of $m^*_{band} = 10.2\ m_e$. We can calculate the value of the London penetration depth from our values for m^* and n_s by using Eq. (5.18), which yields $\lambda_L = 266\,nm$.

The values of m^* and n_s can be used to calculate an effective Fermi temperature for the superconductivity using the equation $k_B T_F = (\hbar^2/2)(3\pi^2 n_s)^{2/3}/m^*$. This yields $T_F = 990\,K$, with the ratio $T_C/T_F = 0.0047$. Uemura *et al.* have described a method of classifying superconductors based on the ratio of the critical temperature T_c to the effective Fermi temperature T_F. It has been observed that the heavy fermion, high-T_C, organic, fullerene, as well as many other unconventional superconductors all lie in the range where $0.01 \leq T_C \leq 0.1$ [68–70]. Re_3Ta is located outside of this 'band of unconventionality', supporting the view that the superconducting mechanism is primarily conventional (the position of this material on the Uemura plot is presented in Sec. 8.2, Fig. 8.1).

5.8.3 Discrepancies between muons & bulk measurements

Penetration depth

The estimate of the penetration depth determined from the μSR measurements is much larger than the estimates one would expect from the critical fields. One estimates $\lambda(0) = 677(6)$ nm from the muon calculations, however this is inconsistent with the measurements of the critical fields, from which $\lambda(0) = 487(8)$ nm is calculated. To try and understand this discrepancy, the ideal field distribution from the flux line lattice for these two penetration depth values has been modelled in Fig. 5.16(a). It can be seen that the main difference is in the tails of the distribution - the maximum cut-off field is much larger when $\lambda = 487\,nm$. The measured field distribution can be extracted from the μSR time spectra using a maximum entropy method - the result of doing this is displayed in Fig. 5.16(b), with the simulations overlaid. Evidently the broadening is the dominant component in what we measure. There is also a peak at 29 mT, which corresponds to the background signal from muons stopping in the silver sample holder. Many different sources may be causing

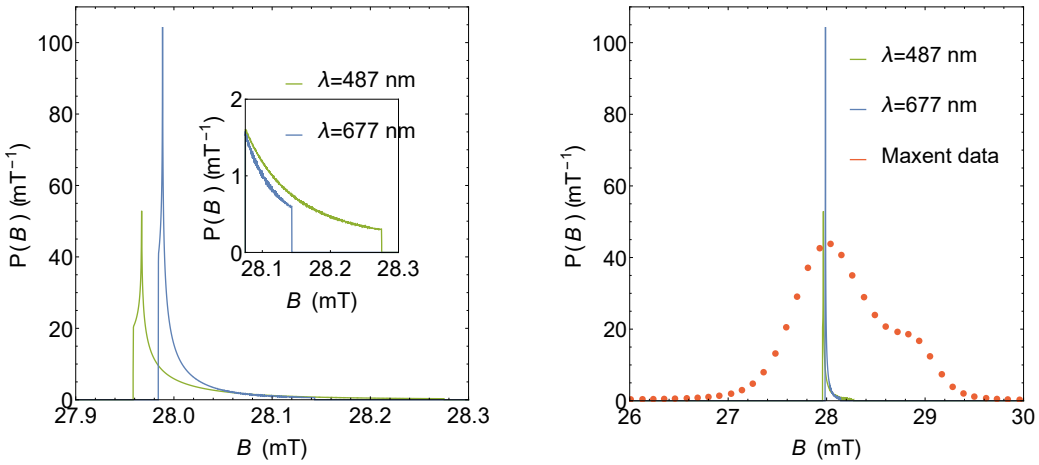

(a) (b)

Fig. 5.16 (a) Ideal field distribution for a vortex lattice with $\lambda = 487$ nm and 677 nm. The other simulation parameters are $\xi = 6.85$ nm and $\langle B \rangle = 28$ mT, which have been kept the same between the two plots. Inset is a detail of the tails of the distribution. (b) The (un-normalized) maximum entropy spectrum extracted from the μSR time spectra collected at $T = 0.3$ K, under an applied field of 30 mT. Overlaid are the (normalized) simulations of $P(B)$ from part (a).

this broadening, including the nuclear dipolar field, vortex disorder, polycrystalline averaging, as well as the intrinsic response function of the instrument.

In order to construct a model for this, the ideal field distribution has been convolved with a Gaussian. The nuclear depolarization rate has been measured to have the field independent value of $0.2603\,\mu s^{-1}$. In general, a Gaussian relaxation rate in the time domain is directly related to the second moment of a Gaussian peak in the field (frequency) domain, by the equation

$$\langle \Delta B^2 \rangle = \frac{\sigma^2}{\gamma_\mu^2}. \tag{5.23}$$

For the nuclear dipolar field, we find $\langle \Delta B_{\rm N}^2 \rangle^{1/2} = 0.306$ mT. At the very minimum, this is the smallest broadening to which the ideal flux line lattice is subjected to. To this convoluted distribution, a Dirac-delta function is added at the position of the background. This sharp peak corresponds to the muons stopping in silver, which do not depolarize. The relative weight of the background peak to the sample response peak is calculated from the relative asymmetries, A_1/A_2, and is found to be split in the ratio 5.2 : 1, sample to background. The entire mixture distribution is then convolved with another Gaussian of width $\langle \Delta B_{\rm g}^2 \rangle^{1/2}$, which models the instrument

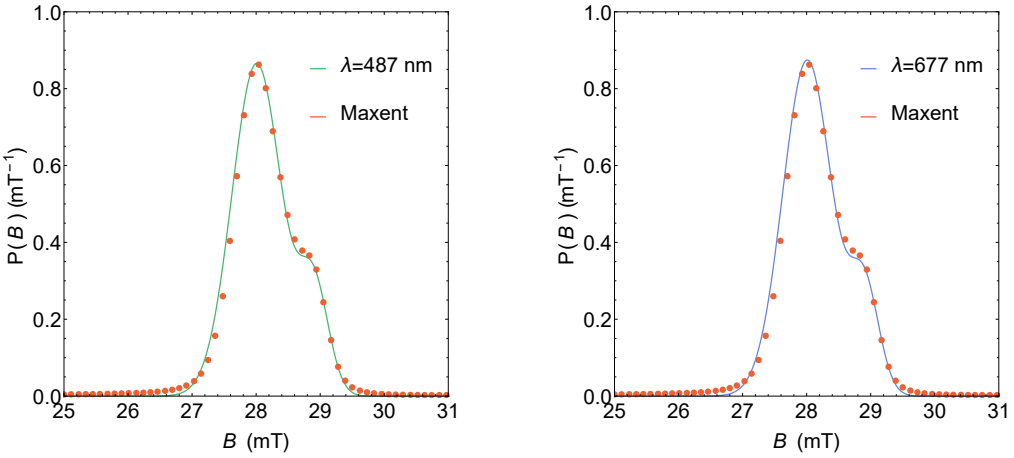

Fig. 5.17 Comparing models for the observed field distribution, $P(B)$, in Re_3Ta. The left figure has $\lambda = 487$ nm, as determined by magnetization measurements. The right figure has $\lambda = 677$ nm, as calculated from μSR measurements. All other simulation parameters are as described in the text.

response broadening. Using $\langle \Delta B_g^2 \rangle^{1/2} = 0.23$ mT, and the same simulation values as before, yields the two figures presented in Fig. 5.17. The two models are extremely similar, and the effect of the long tails in the ideal field distribution is lost due to the broadening effects.

This problem is typical for high-κ superconductors in the low field limit [79], in which the field distributions tend to feature sharp peaks, with very long tails that are easily lost due to noise in a real measurement. This can lead to over estimations of λ, and care needs to be taken when one is measuring these strongly type-II superconductors with μSR. In this case, it is likely that the value of $\lambda = 686$ nm calculated using Eq. (5.11) is overestimated. The laboratory measurements suggest a much lower value of $\lambda = 487$ nm, and it has been shown that the μSR data is not in conflict with this if broadening effects are taken into account.

Suppression of the critical temperature

Another puzzling feature of the μSR data is the clear suppression of T_c in the temperature dependence of the depolarization rate, observed in Fig. 5.18. Extrapolating the data to $T = 0$ suggests that the depolarization will be completely suppressed by fields of less than 100 mT. This is not explainable as a thermometry calibration error, as the internal field experienced by the muons exhibits clear flux expulsion at the expected transition temperature. The explanation may lie in the details of the vortex dynamics in the vicinity of T_c. Thermal motion of flux lines can lead to

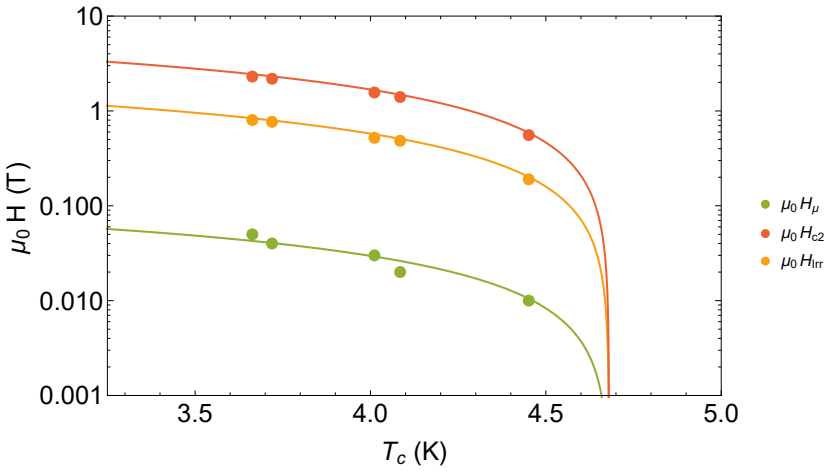

Fig. 5.18 Log plot of the apparent superconducting transition temperature, T_c, as determined by the muon spin depolarization rate collected in a variety of fields, $\mu_0 H_\mu$. For comparison, the corresponding values of the upper critical field (calculated using the WHH model) and the irreversibility line are presented. The lines are guides to the eye.

motional narrowing of the field distribution experienced by the muons. In the high-T_c superconductor, BSSCO, a shoulder in the muon depolarization rate corresponds to the onset of thermal motion of vortices, and a subsequent narrowing of the field distribution [80]. Motion of the vortex lattice requires that thermal fluctuations are sufficiently energetic that vortices can be de-pinned from the lattice. However, this effect is usually observed experimentally in the high temperature superconductors, as typically the energy of thermal fluctuations at the temperatures required for superconductivity in conventional superconductors are far lower than the energy required to de-pin vortices.

It has been observed that the magnetization is not reversible throughout the entire $H-T$ phase diagram, with the de-pinning line shown in Fig. 5.15. The exact shape of the de-pinning line is actually dependent on the sample geometry, and thus cannot be treated as an intrinsic property of the superconductor [81]. The de-pinning line does *not* represent any form of phase transition, however, its existence does inform us that the pinning strength is weak in Re_3Ta. Thermal and quantum fluctuations are mechanisms by which de-pinning may occur. The strength of thermal fluctuations is quantified by the Ginzburg number [82]:

$$G_i = \frac{1}{2}\left(\frac{\mu_0 k_B T_c}{\varepsilon B_c^2(0)\xi^3(0)}\right)^2, \tag{5.24}$$

which measures the ratio of the critical temperature and the condensation energy in a coherence volume. The parameter ε measures the anisotropy, which we assume to be approximately equal to unity for cubic Re_3Ta. Using $T_c = 4.68\,K$, $\xi = 6.85\,nm$, and $B_c(0) = 69.7\,mT$ gives a value of $G_i = 8.5 \times 10^{-6}$. Finally, the quantum resistance can be calculated from the residual resistivity by the equation

$$Qu = \frac{e^2 \rho_0}{\hbar \varepsilon \xi(0)}, \tag{5.25}$$

where this accounts for the effect of macroscopic quantum fluctuations that can lead to de-pinning of vortices. Performing the calculation for $\rho_0 = 243\,\mu\Omega\,cm$ yields $Qu = 8.6 \times 10^{-2}$.

Reference [82] summarises the differences between conventional low temperature superconductors and the high temperature superconductors in terms of G_i and Qu, and the pinning strength in the material. Conventional superconductors tend to exhibit strong pinning, with very weak thermal and quantum fluctuations - characterized by values of $G_i \sim 10^{-8}$ and $Qu \sim 10^{-3}$. On the contrary, high temperature superconductors have very weak pinning, primarily due to the extremely small coherence lengths in these materials. However, the higher transition temperatures and poor resistivity of the parent materials leads to much larger typical values of $G_i \sim 10^{-2}$ and $Qu \sim 10^{-1}$. We find that the values of $G_i = 8.5 \times 10^{-6}$ and $Qu = 8.6 \times 10^{-2}$ calculated for Re_3Ta lie in the intermediate region between the expectation for conventional low temperature superconductors and the high temperature superconductors. Pairing this with the observation of weak pinning in this material, it seems reasonable to suggest that the apparent narrowing of the field distribution observed in the μSR experiment at $T_{c\sigma}$ may be caused by novel low temperature vortex dynamics.

5.9 Summary & Conclusions

A thorough investigation of the superconducting and normal state properties of the noncentrosymmetric superconductor Re_3Ta has been conducted, using detailed magnetization, electrical resistivity, heat capacity, and μSR measurements. The material is well described by the conventional BCS theory, and has been characterized as a strongly type-II superconductor with a nodeless, isotropic superconducting gap. No evidence for time-reversal symmetry breaking has been detected in the μSR experiments. The results of all of the experimental techniques have been combined

to self consistently calculate the electronic properties of the system, from which it has been shown that superconductivity in Re_3Ta is in the dirty limit. The measured and derived superconducting properties of Re_3Ta are summarized in Tab. 5.7.

μSR measurements have revealed the possible existence of unconventional low temperature vortex dynamics. This conclusion has been reached based on the observation of a narrowing of the measured field distribution below T_c, as well as analysis of the pinning, thermal fluctuations, and the quantum resistance. Future experiments at a continuous muon source could investigate the full $H-T$ phase diagram of this material. Also, the morphology of the vortex lattice in single crystals could be studied directly using small angle neutron scattering or STM techniques. The current results add to the body of work surrounding non-magnetic noncentrosymmetric superconductors with strong spin-orbit coupling. Further studies in neighbouring systems will aim to elucidate the connection between anti-symmetric spin-orbit coupling and the relative strengths of the singlet and triplet superconducting channels.

Table 5.7 Properties of the normal and superconducting states in Re_3Ta. In order: superconducting transition temperature; electron-phonon coupling constant under the McMillan formalism; superconducting energy gap; alpha parameter; Sommerfeld constant; Debye temperature; Einstein temperature; relative weight of Debye and Einstein heat capacities; Bloch-Grüneisen estimate of Debye temperature; residual resistivity ratio; residual resistivity; upper critical field; Maki parameter; spin orbit scattering parameter; Pauli limiting field; orbital limiting field; thermodynamic critical field; lower critical field; GL coherence length; magnetic penetration depth; London penetration depth; GL parameter; quasiparticle effective mass; superconducting carrier density; BCS coherence length; electronic mean free path; dirty limit correction; Fermi velocity; Uemura parameter.

Property	Unit	Value
T_c	K	4.68(2)
λ_{ep}		0.64(3)
Δ_0	meV	0.74(1)
$\Delta_0/k_B T_c$		1.83(3)
γ	$mJ\,mol^{-1}\,K^{-2}$	13.1(2)
Θ_D	K	284.2(2)
Θ_E	K	123.4(3)
N_D/N_E		6.84(5)
Θ_R	K	300(5)
RRR		1.04(1)
ρ_0	$\mu\Omega\,cm$	248.5(30)
$\mu_0 H_{c2}(0)$	T	7.0(2)
α_M		1.31(4)
λ_{SO}		1.3(4)
$\mu_0 H_P(0)$	T	9.0
$\mu_0 H_{c2}^{Orb}(0)$	T	8.4
$\mu_0 H_c(0)$	mT	69.7(9)
$\mu_0 H_{c1}(0)$	mT	2.95(8)
$\xi(0)$	nm	6.86(10)
λ	nm	487(9)
λ_L	nm	266
κ_{GL}		71(2)
m^*/m_e		12.6
n	$10^{27}\,m^{-3}$	5.04
ξ_0	nm	4.13
l_e	nm	1.75
ξ_0/l_e		2.36
v_F	$m\,s^{-1}$	48 600
T_c/T_F		0.0047

Chapter 6

Superconductivity of the ternary borides (Lu/Y)RuB_2

6.1 Introduction

Rare-earth ternary boride superconductors are a class of materials which have been observed to exhibit relatively large values of the superconducting transition temperature, T_c. The transition-metal borides with atomic formula RT_4B_4 (where R is the rare-earth atom and T is a transition metal) can crystallize in a number of polytypes, including primitive tetragonal [83], body-centred tetragonal [84], or orthorhombic crystal structures [85]. In all these polytypes, the boron atoms are found to have dimerized into non-interacting B_2 units. The highest values of T_c have been found in the tetragonal polytypes, where the transition metal atoms cluster into isolated tetrahedra and form linear or zigzag chains. In the orthorhombic structure, the T atoms form an extended three-dimensional cluster that interpenetrates. The superconducting transition temperatures are systematically lower in the orthorhombic polytype than the tetragonal compounds across the whole range of rare-earth elements, implying that the dimensionality of the T clusters plays an important role in the superconductivity [86].

A new structural phase in the transition-metal ternary boride family was reported in 1980, after anomalous superconducting transitions were observed with T_c's that did not match known structures [87]. The stoichiometrically distinct RTB_2 phase crystallizes into an orthorhombic structure with the *Pnma* space group. The key feature in this material are zig-zag chains of rare-earth atoms, with dimerized boron. The boron dimers weakly interact, forming straight chains that run in parallel to the direction of the main $R-R$ zig-zag chain, and are perpendicular to planes of R

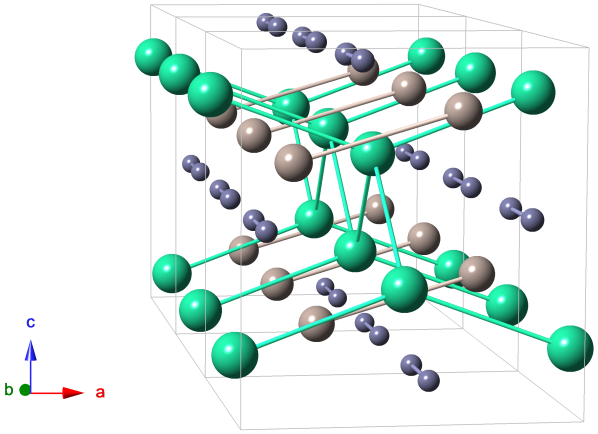

Fig. 6.1 Crystal structure of the RRuB$_2$ ternary borides. The R atoms (large spheres) form zig-zag chains that run parallel to the b crystallographic axis. The B atoms (small spheres) form weakly interacting dimers, with the Ru atoms (medium spheres) isolated.

and T atoms (see Fig. 6.1). Only compounds with non-magnetic R atoms exhibit superconductivity, whereas the inclusion of magnetic atoms is accompanied by magnetic ordering with critical temperatures up to 46 K [88].

Two materials in this family, LuRuB$_2$ and YRuB$_2$, are important as reference materials for studying the entire family tree - the $4f$ electron shell is full in the Lu compound, and empty in the Y compound. Superconductivity has been reported in the Lu compound at temperatures of 9.7 K - 10.1 K, and in the Y compound at temperatures of 7.2 K - 7.8 K, with large values for the upper critical field $\mu_0 H_{C2}$ of 5.7 T and 4.8 T, respectively [88, 89]. These large values indicate that the superconductivity might be expected to be strongly coupled, with a high superconducting carrier density. However, NMR measurements have identified that these materials appear to lie in the weak-coupling limit of the conventional BCS theory [90, 2]. In this chapter, we report the results of a muon-spin rotation and relaxation (μSR) study of the superconducting properties in this pair of materials. We combine the results with previously reported findings in order to further characterize the electronic properties of the superconducting state.

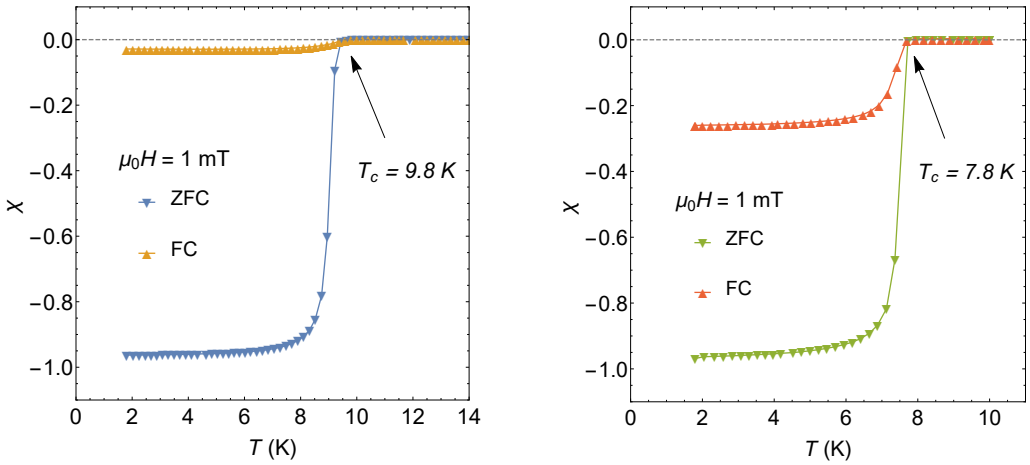

Fig. 6.2 Temperature dependence of the magnetic susceptibility in (a) $LuRuB_2$ and (b) $YRuB_2$, collected in zero-field cooled and field cooled regimes under an applied field of 1 mT.

6.2 Sample synthesis

Polycrystalline samples of $LuRuB_2$ and $YRuB_2$ were prepared by arc-melting stoichiometric quantities of high-purity Y/Lu, Ru, and B in a tri-arc furnace under an Ar (5N) atmosphere on a water cooled copper hearth. Each sample was flipped and remelted several times in order to improve the homogeneity of the as-cast ingot. The samples were subsequently sealed in evacuated quartz tubes, and annealed at 1050 °C for one week.

6.3 Magnetization

The superconducting transition temperature, T_c, for each sample was checked via dc magnetic susceptibility measurements using a 5 T Quantum Design Magnetic Property Measurement System. The temperature dependence of the magnetic susceptibility in an applied field of 1 mT is displayed in Fig. 6.2. The observed transition temperatures for the Lu and Y compounds are approximately 9.8 K and 7.8 K, in agreement with previous reports [88, 89]. After correcting for demagnetization, a full superconducting volume fraction is found in both samples. The Meissner fraction, χ_{FCC}/χ_{ZFCW}, in the Y compound is 11 times larger than in the Lu compound, indicating that flux pinning is much weaker in $YRuB_2$. The dc susceptibility data highlights no irregularities or anomalies that may be due to impurities in the sample ordering magnetically or become superconducting.

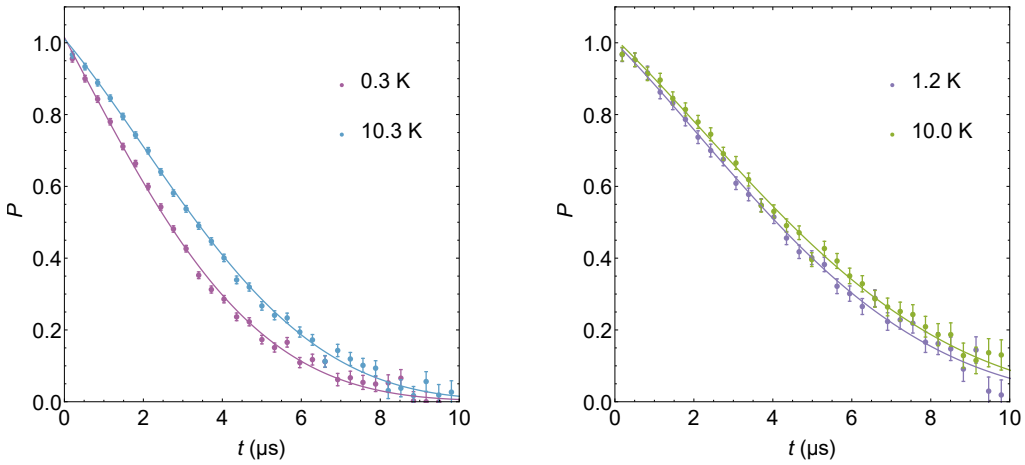

(a) (b)

Fig. 6.3 Time evolution of the spin polarization of muons implanted under zero-field conditions in (a) $LuRuB_2$ and (b) $YRuB_2$ at temperatures above and below T_c. The time independent background due to muons stopping in silver has been subtracted, and the data normalized to the initial asymmetry - the muons are 100 % spin-polarized at $t = 0$ s. The solid lines are the results of fitting the data to Eq. (6.2).

6.4 Muon Spectroscopy

Muon-spin relaxation measurements in zero-field (ZF) and muon-spin rotation experiments in transverse-field (TF) were carried out on the MuSR spectrometer at the ISIS pulsed neutron and muon source. Powdered samples were mounted on silver sample plates using GE varnish. In ZF, silver produces a time-independent background, whilst in TF it contributes a non-decaying oscillation; both cases are easy to account for during data analysis. Both samples were mounted in a ^{3}He sorption cryostat with a temperature range of 0.3 to 50 K. For the ZF measurements, samples were cooled in zero applied field, and data points were collected in increments upon warming. Stray fields at the sample position are actively cancelled to within 1 μT by a flux gate magnetometer and an active compensation system controlling three pairs of correction coils. The TF experiments were conducted in a field of 30 mT. The samples were field cooled to base temperature in order to promote the formation of a well-ordered flux line lattice, and data points were collected upon incremental warming.

6.4.1 Zero & longitudinal-field muon-spin relaxation

Results from the ZF-μSR relaxation experiments are presented first. Figure 6.3 shows the time evolution of the muon-spin polarization in both samples collected above and below T_c. There is a clear change in the relaxation behaviour on either side of the transition in both compounds, although the difference is much subtler in the Y compound. There is no evidence for an oscillatory component, which indicates that there is no coherent field associated with magnetic ordering. In the absence of atomic moments, the depolarization of the muon ensemble is due to the presence of static, randomly oriented nuclear moments. This behaviour is modelled by the Gaussian Kubo-Toyabe equation [49]

$$G_{\mathrm{KT}}(t) = \frac{1}{3} + \frac{2}{3}(1-\sigma_{\mathrm{ZF}}^2 t^2)\exp\left(-\frac{\sigma_{\mathrm{ZF}}^2 t^2}{2}\right), \tag{6.1}$$

where σ_{ZF} measures the width of the nuclear dipolar field experienced by the muons. The spectra are well described by the function

$$G_z(t) = G_{\mathrm{KT}}(t)\exp(-\Lambda t), \tag{6.2}$$

where Λ measures the electronic relaxation rate, and is usually attributed to 'fast-fluctuation' effects that occur on a timescale much shorter than the muon lifetime.

The nuclear term σ_{ZF} is found to remain temperature independent in both compounds. As the temperature is increased from base, there is an exponential decrease in Λ in both materials (see Fig. 6.4). This is reminiscent of the 'critical slowing down' behaviour of spin-fluctuations in the vicinity of phase transitions to magnetically ordered states [91, 92]. In both materials a small longitudinal field of 10 mT is sufficient to completely decouple the Gaussian component of the relaxation. There is no clear anomaly at T_c in either material, indicating that the process responsible for these fluctuations is independent of the superconductivity. We conclude that we do not see any evidence for broken time-reversal symmetry.

6.4.2 Transverse-field muon-spin rotation

In order to characterize the flux-line lattice, TF-μSR was performed in a field of 30 mT in both materials. A selection of typical polarization spectra collected above and below T_c is displayed in Fig. 6.5. The enhanced depolarization rate below T_c is due to the field distribution $P(B)$ formed by the flux line lattice in the mixed state of the superconductor. Measuring the second moment $\langle \Delta B^2 \rangle$ of this field

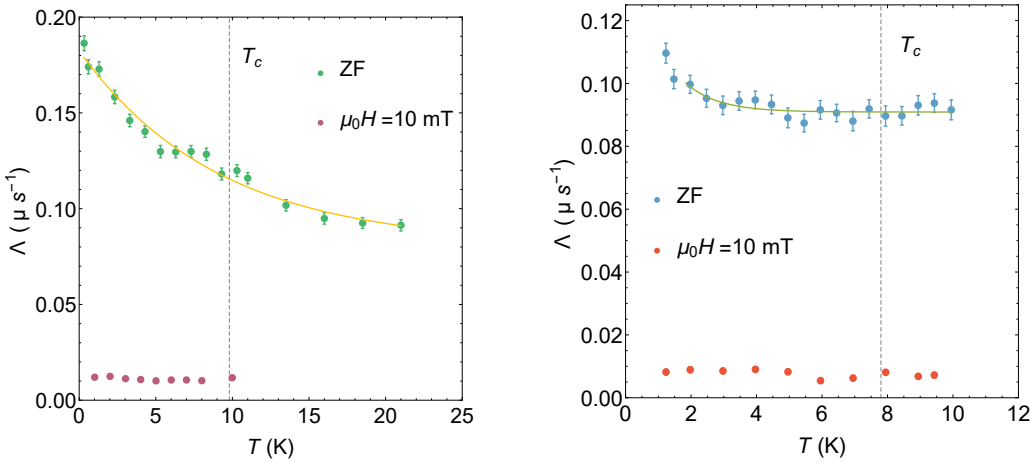

Fig. 6.4 Temperature dependence of the electronic relaxation rate in $LuRuB_2$ (a) and $YRuB_2$ (b), collected in ZF and in an applied longitudinal field of 10 mT. The solid lines are guides to the eye, indicating the exponential decay of Λ in ZF as T is increased.

distribution allows the magnetic penetration depth, λ, to be calculated to a high degree of accuracy. In order to determine $\langle \Delta B^2 \rangle$, the TF spectra are modelled as a sum of n sinusoidal oscillations, each within a Gaussian relaxation envelope:

$$G_x(t) = \sum_{i=1}^{n} A_i \exp\left(-\frac{\sigma_i^2 t^2}{2}\right) \cos(\gamma_\mu B_i t + \phi), \tag{6.3}$$

where A_i is the initial asymmetry, σ_i is the Gaussian relaxation rate, and B_i is the first moment of the i'th component in the field distribution. There is a phase offset ϕ, which is shared by each oscillating component, and $\gamma_\mu/2\pi = 135.5\,\mathrm{MHz\,T^{-1}}$ defines the muon gyromagnetic ratio. The number of components required is generally in the range $1 \leq n \leq 5$, with the requirement determined by the superconducting characteristics of the material. Strongly type-II superconductors with large penetration depths are often modelled well by a single oscillation, whereas low-κ materials, in which the coherence length plays a more important role in the structure of $P(B)$, may require up to 5 separate oscillating components [23]. Treating the data in this way is equivalent to modelling the internal field distribution in the superconductor $P(B)$ as a sum of n individual Gaussian distributions, [93]

$$P(B) = \gamma_\mu \sum_{i=1}^{n} \frac{A_i}{\sigma_i} \exp\left(-\frac{\gamma_\mu^2 (B - B_i)^2}{2\sigma_i^2}\right). \tag{6.4}$$

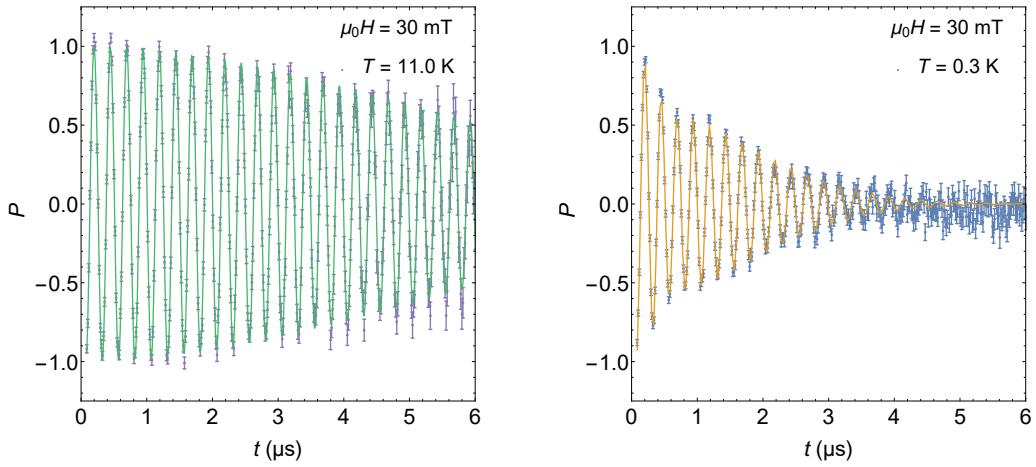

(a) (b)

Fig. 6.5 Representative TF-μSR polarization signals collected (a) above and (b) below T_c in $LuRuB_2$ under an applied field of 30 mT. A non-decaying background oscillation due to muons stopping in the silver has been subtracted, and the data normalised to the initial asymmetry. The solid lines are fits using Eq. (6.3).

The second moment of this field distribution is thus

$$\langle \Delta B^2 \rangle = \frac{\sigma_{\text{eff}}^2}{\gamma_\mu^2} = \sum_{i=1}^{n} \frac{A_i}{A_{\text{tot}}} \left[\frac{\sigma_i^2}{\gamma_\mu^2} + (B_i - \langle B \rangle)^2 \right], \tag{6.5}$$

where $A_{\text{tot}} = \sum_{i=1}^{n} A_i$ and $\langle B \rangle = A_{\text{tot}}^{-1} \sum_{i=1}^{n} A_i B_i$ is the first moment of $P(B)$. Finally, the extra broadening from the nuclear moments σ_N must be subtracted in quadrature from the total effective depolarization rate σ_{eff} to yield the contribution of the flux-line lattice $\sigma_{\text{FLL}}^2 = \sigma_{\text{eff}}^2 - \sigma_N^2$. σ_N is assumed to be temperature independent, and is determined by measurements made in the normal state just above T_c.

Two oscillating components were required to adequately describe the $LuRuB_2$ spectra, whereas three were required for the $YRuB_2$ - a non-decaying background oscillation due to muons stopping in the silver sample holder has been subtracted from the spectra presented in Fig. 6.5. Above T_c a single oscillation suffices in both materials to describe the depolarization. The temperature dependences of the muon spin depolarization rate are presented in Fig .6.6 ($LuRuB_2$) and Fig. 6.7 ($YRuB_2$). The total effective depolarization rate, σ_{eff}, for each compound has been calculated using Eq. (6.5).

In superconductors with large critical fields and hexagonal flux line lattices, there exists a simple relationship between the Gaussian depolarization rate σ_{FLL} and the magnetic penetration depth, as long as the average field is a very small fraction of

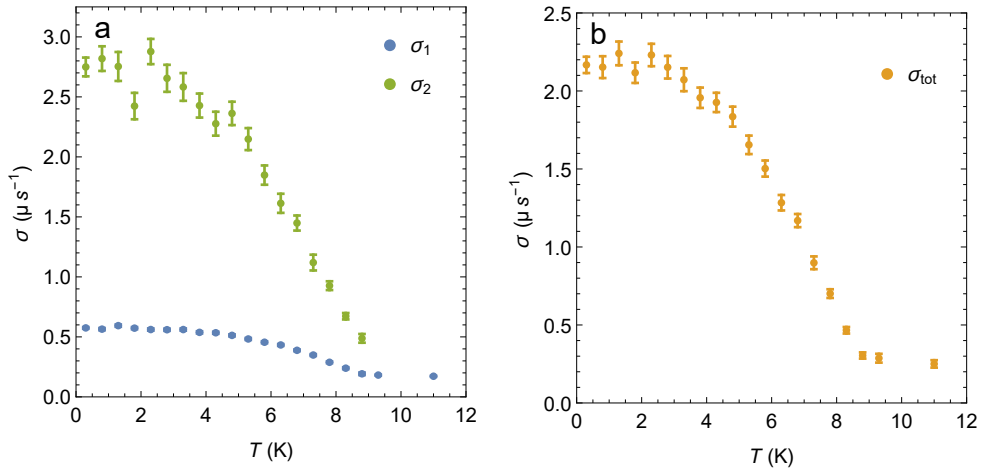

Fig. 6.6 TF-μSR muon depolarization rates in $LuRuB_2$. (a) Depolarization rates of the two fitted oscillation components extracted directly from the time-series asymmetry. (b) Effective depolarization rate, calculated using the data in (a) and Eq. (6.5).

the upper critical field $\mu_0 H_{C2}$. For both compounds $B/\mu_0 H_{C2} \approx 0.005$ and so we can use the expression [24]

$$\frac{\sigma_{\mathrm{FLL}}^2(T)}{\gamma_\mu^2} = 0.00371 \frac{\Phi_0^2}{\lambda^4(T)}, \tag{6.6}$$

where Φ_0 is the magnetic flux quantum. The magnetic penetration depths at $T = 0\,\mathrm{K}$ are thus found to be $\lambda_{\mathrm{Lu}}(0) = 221(2)\,\mathrm{nm}$ and $\lambda_{\mathrm{Y}}(0) = 190(1)\,\mathrm{nm}$ for the $LuRuB_2$ and $YRuB_2$ materials, respectively.

6.5 Results & Discussion

Assuming London local electrodynamics, the temperature dependence of λ can be calculated for an isotropic s-wave superconductor in the clean limit using the following equation:

$$\frac{\lambda^{-2}(T)}{\lambda^{-2}(0)} = 1 + 2\int_{\Delta(T)}^{\infty} \left(\frac{\partial f}{\partial E}\right) \frac{E\,\mathrm{d}E}{\sqrt{E^2 - \Delta^2(T)}}, \tag{6.7}$$

where $f = [1 + \exp(E/k_{\mathrm{B}}T)]^{-1}$ is the Fermi function and

$$\Delta(T) = \Delta(0) \tanh\{1.82[1.018(T_c/T - 1)]^{0.51}\}$$

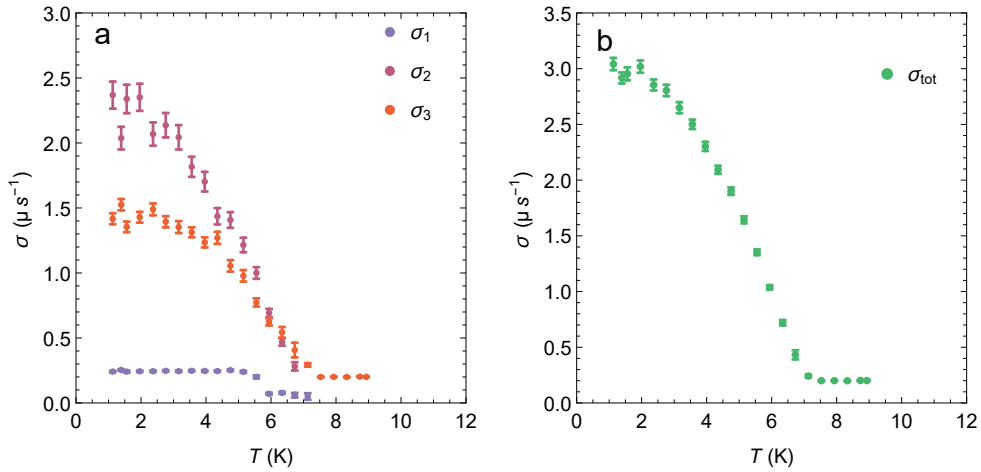

Fig. 6.7 TF-μSR muon depolarization rates in $YRuB_2$. (a) Depolarization rates of the three fitted oscillation components extracted directly from the time-series asymmetry. (b) Effective depolarization rate, calculated using the data in (a) and Eq. (6.5).

is the BCS approximation for the temperature dependence of the energy gap. The inverse-squared penetration depth is presented in Fig. 6.8 for both materials, with fits to the data using this model. The resultant values for the energy gaps are $\Delta_{Lu}(0) = 1.36(3)$ meV and $\Delta_{Y}(0) = 1.10(1)$ meV. The BCS theory proposes a universal proportionality between the energy gap and the superconducting transition temperature. This is conventionally encoded in the BCS parameter, $2\Delta(0)/k_B T_c$, which has the theoretical value of 3.52 in the weak coupling limit. For the Lu and Y compounds, the BCS parameters are found to be 3.3(2) and 3.4(1), respectively. This seems to classify the (Lu/Y)RuB_2 ternary borides as conventional, weakly coupled BCS type-II superconductors, in agreement with the NMR results [90].

The magnetic penetration depth is directly related to the electronic properties of the superconducting state by the expression

$$\lambda(0) = \left[\frac{m^*/m_e}{4\pi n_s r_e}\left(1+\frac{\xi}{l}\right)\right]^{\frac{1}{2}}, \tag{6.8}$$

where m^* is the effective mass of charge carrying electrons, n_s is the superconducting charge carrier density, and r_e and m_e are the classical radius [94] and rest mass of the electron, respectively. The ratio of superconducting coherence length to the mean free path, ξ/l, encodes the dirty limit correction, which for the Lu and Y compounds has been found to take on small values of 3.9 and 0.85, respectively [89]. Equation (6.8) can be coupled with the expression for the Sommerfeld constant γ,

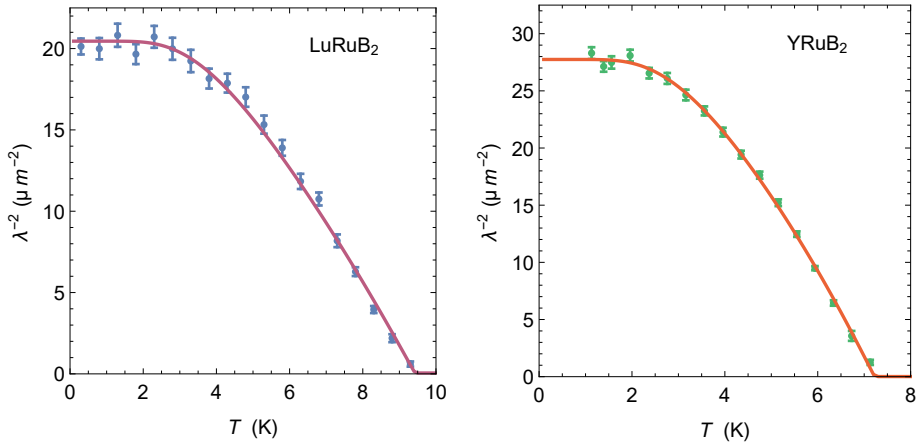

Fig. 6.8 Temperature dependence of the inverse squared penetration depth, λ^{-2}, for $LuRuB_2$ (left) and $YRuB_2$ (right). The solid lines are the results of fitting Eq. (6.7) to the data.

Table 6.1 Superconducting properties of the ternary borides determined from the μSR experiments.

Property	Unit	$LuRuB_2$	$YRuB_2$
λ	nm	221(2)	190(1)
Δ_0	meV	1.36(3)	1.10(1)
Δ_0/k_BT_c	3.3(2)	3.4(1)	
m^*/m_e		9.83	15.0
n	$10^{28}\,m^{-3}$	2.73	2.17
ξ_0/l_e		3.9	0.85
λ_L	nm	10.5	14.6
T_F	K	3910	2190
T_c/T_F		0.002	0.003

which is also related to the electronic properties of the system: [95]

$$\gamma = \left(\frac{\pi}{3}\right)^{\frac{2}{3}} \frac{k_B^2 m^* n_e^{\frac{1}{3}}}{\hbar^2}, \tag{6.9}$$

where n_e is the electronic carrier density and k_B is Boltzmann's constant. By assuming that n_e at T_c is equivalent to n_s as $T \to 0\,K$, Eqs. (6.8) and (6.9) can be solved simultaneously to find values for m^* and n_s. Consequently an effective Fermi temperature can be calculated using the relation $k_BT_F = (\hbar^2/2)(3\pi^2 n_s)^{2/3}/m^*$. The results of following this procedure are displayed in Table 6.1.

Uemura *et al.* have described a method of classifying superconductors based on the ratio of the critical temperature T_c to the effective Fermi temperature T_F, which

is found to be $1/414$ and $1/304$ for the Lu and Y compounds, respectively [68–70]. This places the ternary borides in the vicinity of the 'band of unconventionality' described by Uemura (the position of these materials on the Uemura plot is presented in Sec. 8.2, Fig. 8.1). This is the first indication that the superconductivity in these compounds may not be entirely conventional. In fact, both compounds find themselves occupying the same region in the Uemura diagram as the borocarbide superconductors, and the rare-earth hexaborides [95]. High transition temperatures are a common theme in these families of materials, as well as the intriguing interplay between the superconductivity and the complex magnetic order associated with the rare-earth $4f$ electrons.

6.6 Conclusions

In conclusion, TF and ZF-μSR measurements have been carried out on the rare-earth ternary borides (Lu/Y)RuB_2. Both superconductors are well described by the conventional BCS theory of superconductivity in the weakly coupled limit, with fully gapped *s*-wave order parameters and preserved time-reversal symmetry in the superconducting state. The ZF-μSR measurements have revealed the presence of spin fluctuations, coexistent with the superconducting phase. Calculations of the electronic properties of the superconducting state reveal that the rare-earth ternary borides share similarities with the hexaboride and borocarbide superconducting families.

Chapter 7

Multiband superconductivity in $Lu_3Os_4Ge_{13}$

7.1 Introduction

The superconducting and physical properties of the ternary intermetallic compound $Lu_3Os_4Ge_{13}$ has recently been the focus of a number of studies due to several unusual features. This material crystallizes in a cubic structure, with the centrosymmetric spacegroup $Pm\bar{3}n$, and exhibits superconductivity at 3.1 K [96]. The structure is analogous to that of the Skutterudites where the $RuGe_6$ trigonal prisms create cages containing a single Ge atom - three views of the structure are presented in Fig. 7.1. Heat capacity measurements performed on $Lu_3Os_4Ge_{13}$ single crystals have suggested that the superconductivity may feature multiple gaps, or is at least anisotropic in nature (see Fig. 7.2) [97]. Another interesting feature of these data is the observed field dependence of the Sommerfeld constant, γ, in the superconducting state. For nodeless superconductors, this relationship is expected to be linear, as we observed in Re_3Ta in Fig. 5.9. This interpretation arises because the Sommerfeld constant is directly related to the density of states [77]. In superconductors with nodes or anisotropy in the gap, a power law is expected for γ as a function of field, and this is indeed what has been observed in Fig. 7.3.

A further noteworthy property of this material is that the upper critical field extracted from a WHH fit is very close to the calculated Pauli limiting field [98]. If $Lu_3Os_4Ge_{13}$ is indeed a multi band superconductor, then it could be expected to exceed the Pauli limiting field due to upwards curvature of H_{c2}. Finally, magnetization measurements show that this material exhibits Pauli paramagnetism. It has

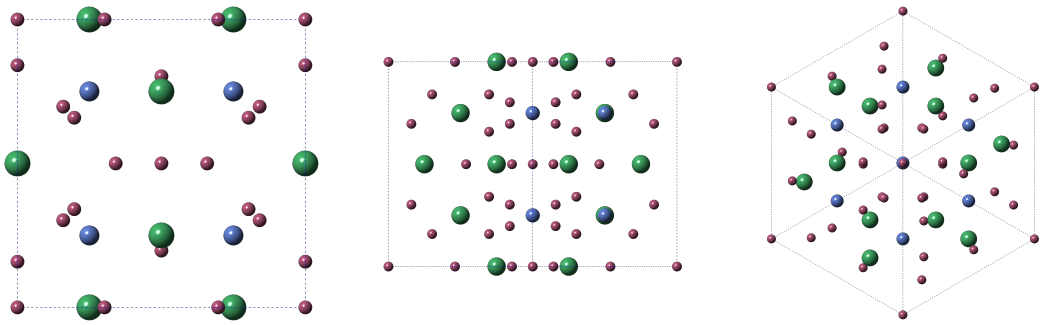

(a) (b) (c)

Fig. 7.1 Crystal structure of $Lu_3Os_4Ge_{13}$, viewed along (a) the [100] direction, (b) the [110] direction, and (c) the [111] direction.

been reported that in systems with spin-triplet superconductivity, paramagnetism can greatly enhance the possibility of a non-unitary spin-triplet ground state [12].

With these considerations in mind, a μSR study has been carried out to try and determine the pairing symmetry of the superconducting electrons. We have also searched for evidence of broken time-reversal symmetry in zero-field.

7.2 Sample synthesis

The sample used in the μSR experiment was produced using the Czochralski method in a tetra-arc furnace. Stoichiometric quantities of the constituent elements were first melted together in a tri-arc furnace, in order to make 10 g boules. These were then melted in the tetra-arc furnace, and single crystals were pulled from the melt using a tungsten seed rod, withdrawn at a rate of $10\,\mathrm{mm\,h^{-1}}$. The sample used in this study was crushed into a powder for the μSR experiments, and was produced in the same batch as the sample studied in Refs. [98, 97, 96].

7.3 Magnetization

Magnetization measurements were performed using a 5 T QD MPMS and a 12 T Oxford Instruments VSM in order to compare the quality of our sample with the published results. Figure 7.4(a) presents low temperature magnetization data, showing the onset of the superconducting transition at $T_c = 3.1$ K. The transition is rather broad, and a full superconducting volume fraction is not realized in the temperature regime studied. This is in agreement with the results published in Ref. [97], where the superconducting transition also appears to be broad. Magnetization against field

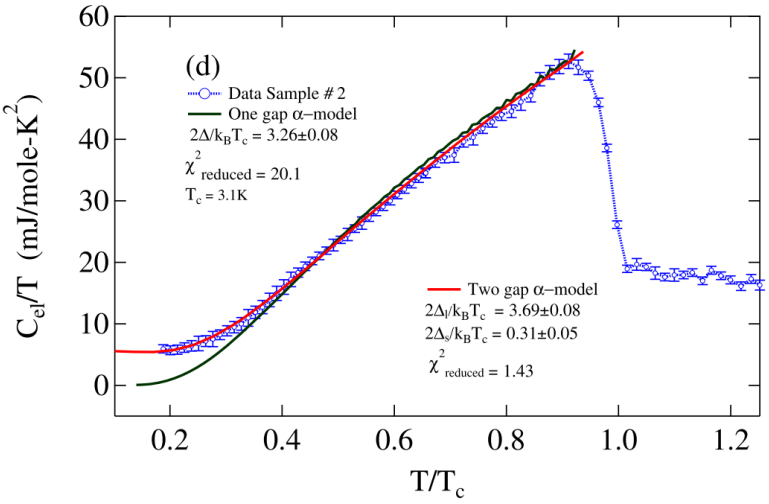

Fig. 7.2 The heat capacity of this material appears to be well described by a two-gap model. X-ray diffraction shows that the sample investigated is phase pure, such that any impurity that could explain the data would also be visible in the X-ray spectrum. Figures and data are reproduced from Ref. [97].

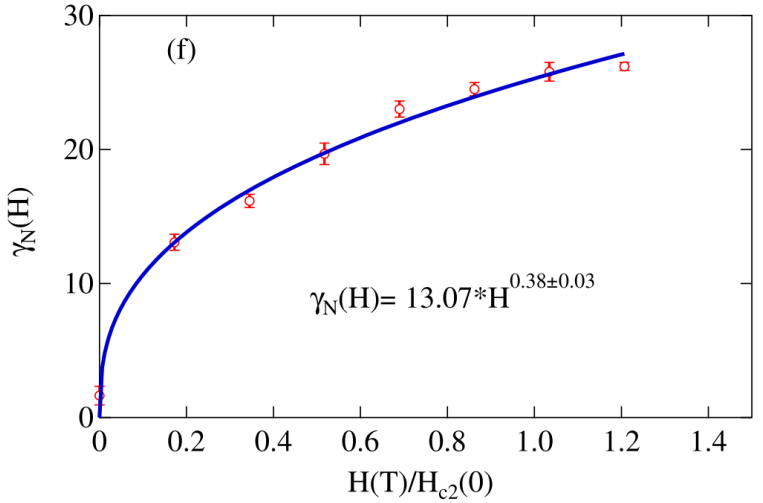

Fig. 7.3 Field dependence of the Sommerfeld constant, where a power law of the form $\propto H^{0.38}$ has been fitted. This can be an indicator of nodeless superconductivity, and suggests that the superconducting ground state is unconventional [77]. Figures and data are reproduced from Ref. [97].

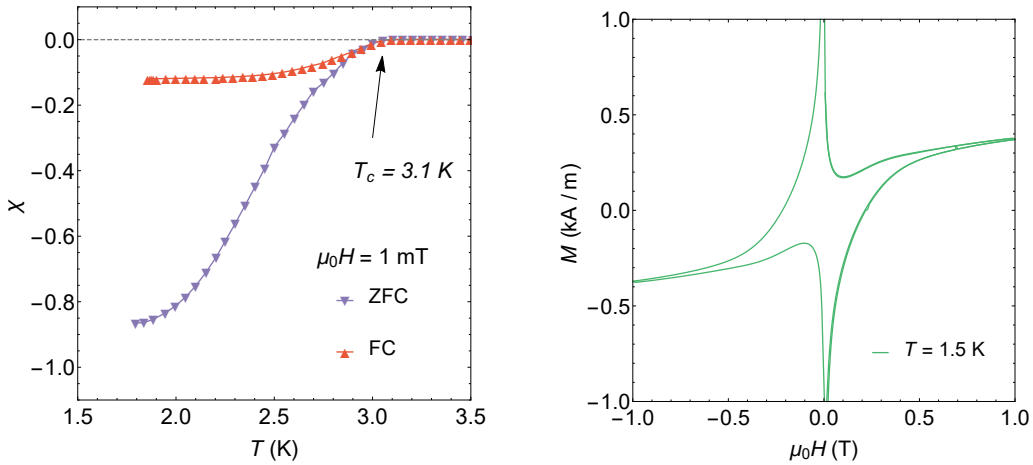

(a) (b)

Fig. 7.4 Magnetic susceptibility measurements performed on the polycrystalline sample of $Lu_3Os_4Ge_{13}$. (a) Temperature dependence of the magnetic susceptibility, collected in ZFC and FC regimes in an applied field of 1 mT. (b) Field dependence of the magnetization collected at $T = 1.5$ K.

loops collected at a temperature of 1.5 K is displayed in Fig. 7.4(b). The loop follows the characteristic hysteretic behaviour associated with pinning of vortices in type-II superconductors, and it is also clear that the material is paramagnetic.

7.4 Muon spin rotation and relaxation

7.4.1 Transverse-field

Transverse-field μSR experiments were performed on the MuSR spectrometer at ISIS, in an attempt to measure the temperature dependence of the superfluid density. A powdered sample of $Lu_3Os_4Ge_{13}$ was mounted on a silver sample holder and placed in a dilution refrigerator operating between 60 mK and 4 K. Measurements were made in the field range ($5 \leq \mu_0 H \leq 60$) mT, and a full temperature dependence was carried out for $\mu_0 H = 40$ mT. Representative μSR signals collected above and below T_c are presented in Fig. 7.5. The broadening due to the vortex lattice was modelled by a Gaussian damped oscillation of the form:

$$G_x(t) = \sum_{i=1}^{n} A_i \exp\left(-\frac{\sigma_i^2 t^2}{2}\right) \cos(\gamma_\mu B_i t + \phi), \tag{7.1}$$

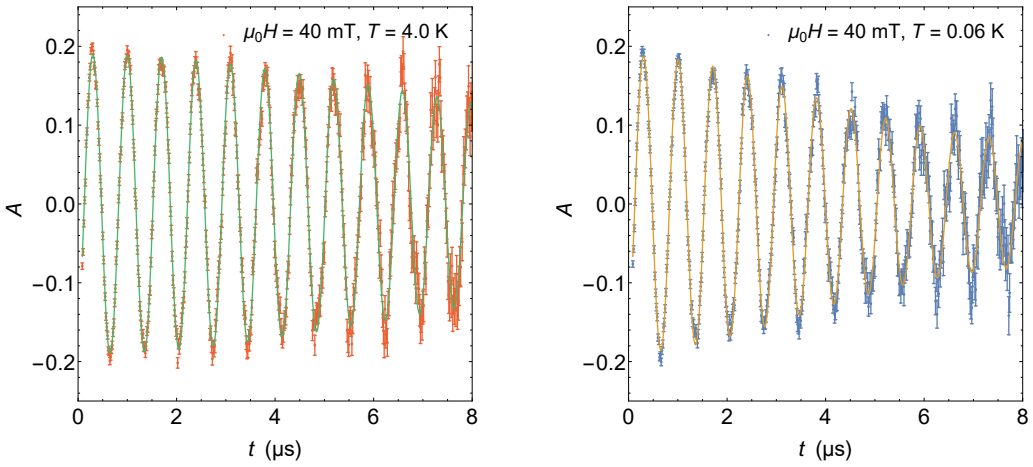

(a) (b)

Fig. 7.5 Representative TF-μSR signals collected (a) above and (b) below T_c in an applied magnetic field of 40 mT. The data have been transformed into a rotating reference frame with a frequency of 4 MHz, as described in Ref. [99].

where A_i is the initial asymmetry, σ_i is the Gaussian relaxation rate, and B_i is the first moment of the i'th component in the field distribution. There is a phase offset ϕ, which is shared by each oscillating component, and $\gamma_\mu/2\pi = 135.5\,\mathrm{MHz\,T^{-1}}$ defines the muon gyromagnetic ratio. For this sample, $n = 2$ modelled the distribution adequately, with σ_2 fixed to zero in order to account for the non-depolarizing background signal. The extracted temperature dependence of the depolarization rate, σ, attributed to the sample is presented in Fig. 7.6. The laboratory measurements have determined that the upper critical field is large ($\mu_0 H_{c2} = 5.4\,\mathrm{T}$), which means that the reduced field, H/H_{c2} for these experiments is ~ 0.01. Also, κ has been estimated to have a large value of ~ 61 [97, 96]. We therefore expect the depolarization rate to be field independent in this regime, and this has been confirmed in the inset of Fig. 7.6. We are also in the regime described by Brandt, in which the depolarization rate is related to the superfluid density by a simple numerical pre-factor (see Sec. 2.2.1).

The temperature dependence of σ exhibits a number of unusual properties. Qualitatively, the apparent onset temperature of the increased depolarization rate due to the vortex lattice is much lower than the bulk measurements of $T_c = 3.1\,\mathrm{K}$. The transition also appears to be very broad, and looks approximately linear down to very low temperatures, at which point a small plateau can be seen. As discussed in Sec. 2.7.2, the low temperature behaviour of the superfluid density can indicate the presence of nodes or anisotropy in the superconducting gap, as it implies quasiparticle

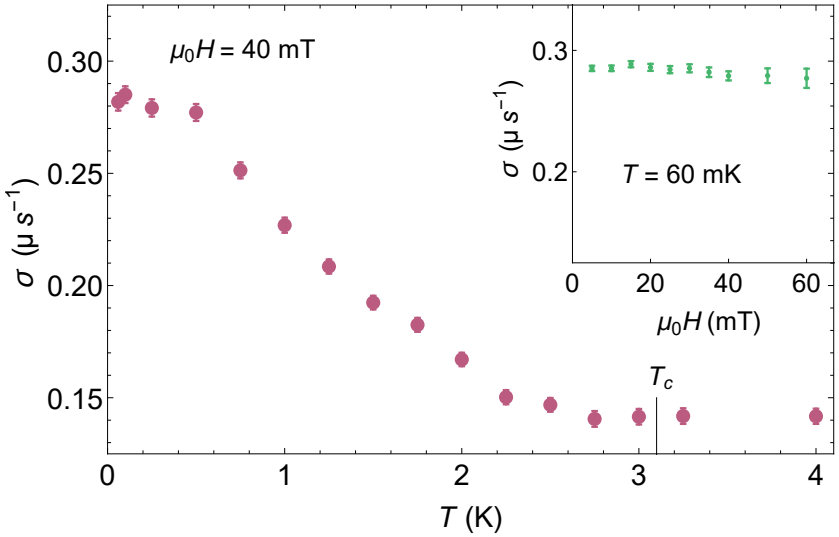

Fig. 7.6 Temperature dependence of the TF depolarization rate, collected in an applied field of 40 mT. Inset: the depolarization rate at $T = 60$ mK collected under applied fields between 5 mT and 60 mT, showing it's approximate field independence in this range.

Table 7.1 Results of fitting the depolarization using different models for the angular dependence of the pairing symmetry.

Model	$\sigma(0)$ (μs^{-1})	σ_N (μs^{-1})	Δ_0 (meV)	χ^2_{red}
Single-gap s-wave	0.239(4)	0.144(2)	0.264(9)	2.81
Double-gap s-wave ($w = 0.5(1)$)	0.246(2)	0.140(2)	0.44(9) 0.18(3)	0.86
Anisotropic s-wave ($a = 0.57(5)$)	0.246(3)	0.140(2)	0.46(3)	0.92
d-wave	0.259(4)	0.140(2)	0.44(2)	2.12

excitations are occurring at much lower temperatures than would be expected by a fully gapped superconductor.

The currently available experimental data suggest that the superconductivity in $Lu_3Os_4Ge_{13}$ exhibits either two-gap superconductivity, or has an anisotropic gap. The field dependence of γ presented in Fig. 7.3 could also be supportive of a superconducting gap that exhibits nodes [77]. To investigate the possible nature of the gap, four models have been fitted to the measured depolarization rate: (a) s-wave, (b) s+s-wave, (c) anisotropic s-wave, and (d) d-wave [23].

Over a spherical Fermi surface, Eq. 2.70 for the superfluid density becomes [100]:

$$\rho_s = 1 + \frac{1}{\pi}\int_0^{2\pi} d\phi \int_\Delta^\infty dE \left(\frac{\partial f}{\partial E}\right) \frac{E}{\sqrt{E^2 - \Delta^2(T,\phi)}}. \tag{7.2}$$

The gap function now has the form $\Delta(T,\phi) = \Delta(T)F(\phi)$, where $\Delta(T)$ is the approximation for the BCS temperature dependence of the gap (Eq. 2.32), and $F(\phi)$ encodes the angular dependence of the gap around the Fermi surface at an angle, ϕ. For *s*-wave superconductors, the gap is isotropic, and therefore we have $F^{\mathrm{s}}(\phi) = 1$. For the *d*-wave gap, $F^{\mathrm{d}}(\phi) = |\cos(2\phi)|$, which leads to the formation of line nodes around the Fermi surface with four-fold symmetry. An anisotropic *s*-wave gap is given by $F^{\mathrm{s_A}}(\phi) = (1 + a\cos 4\phi)/(1+a)$, where the parameter a measures the anisotropy. Varying a from 0 to 1 interpolates smoothly from an isotropic gap, to a gap featuring line nodes. Finally, for a two-gap, $s+s$-wave model, one assumes that the total superfluid density is the sum of two components [100, 101]:

$$\rho_{\mathrm{s}} = w\frac{\lambda^{-2}(T,\Delta_{0,1})}{\lambda^{-2}(0,\Delta_{0,1})} + (1-w)\frac{\lambda^{-2}(T,\Delta_{0,2})}{\lambda^{-2}(0,\Delta_{0,2})}. \tag{7.3}$$

The results of fitting these models to the depolarization rate are presented in Figs. 7.7 (a)-(d), with the numerical values reported in Tab. 7.1. Also plotted as an inset for each figure is the corresponding angular dependence of the superconducting gap. The transition temperature, T_{c}, was fixed to the experimentally observed bulk value of 3.1 K for all fitting routines.

To compare the models, the reduced χ^2 has been calculated for each fit, and is displayed in the final column of Tab. 7.1. Evidently, the isotropic *s*-wave model provides a very poor fit to the data, as is confirmed by visual inspection. This is also true of the *d*-wave model. The calculated χ^2_{red} values for the $s+s$-wave model and the anisotropic *s*-wave models are 0.86 and 0.92, respectively. Thus, these both provide reasonable fits to the data, however, the fact that both values are less than one implies that the model is too restrictive. If the uncertainties on the data have been overestimated, then this could account for the small values of χ^2_{red} in both cases. However, we can conclude that the superconducting gap is most likely nodeless, with either two gaps or a single anisotropic gap based on this analysis, as opposed to having an isotropic gap or exhibiting line-nodes.

The gap to T_{c} ratio for the anisotropic model is equal to $1.7(1)$. The corresponding value given by an anisotropic fit to the heat capacity data presented in Fig. 7.2 is $1.62(1)$. These are seemingly in good agreement, however, visual inspection of Fig. 7.2 reveals that this model describes the heat capacity data very poorly. A much better fit to the heat capacity data is provided by a two-gap model, where the authors of Ref. [97] calculate $\Delta_{0,1}/k_{\mathrm{B}}T_{\mathrm{c}} = 1.84(2)$ and $\Delta_{0,2}/k_{\mathrm{B}}T_{\mathrm{c}} = 0.17(1)$. Comparing this to the μSR results, the results of our modelling suggest values of

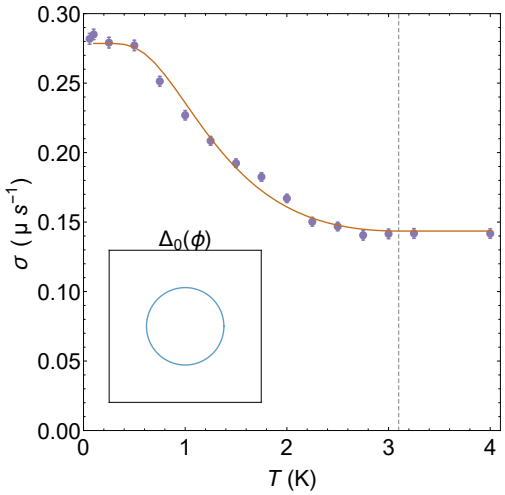

(a) Single-gap *s*-wave model.

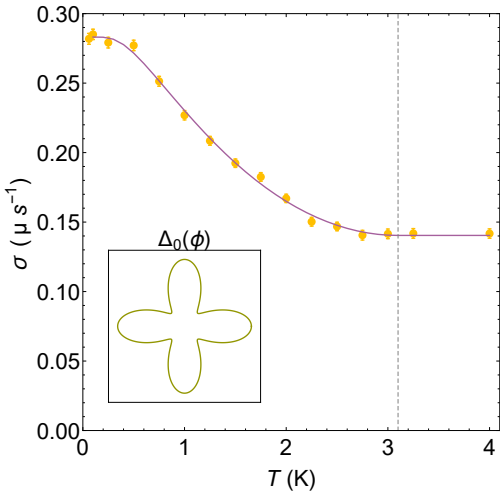

(c) Anisotropic *s*-wave model.

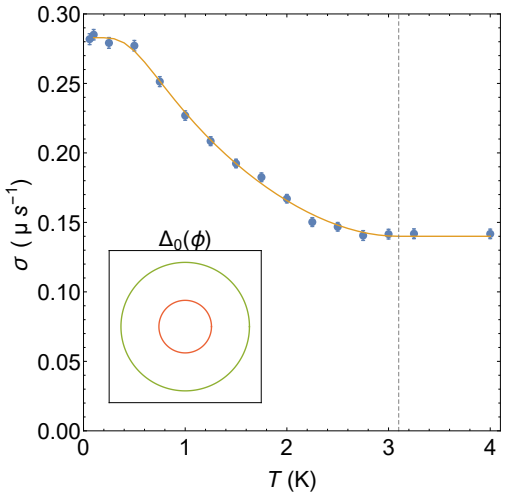

(b) Two-gap *s*-wave model.

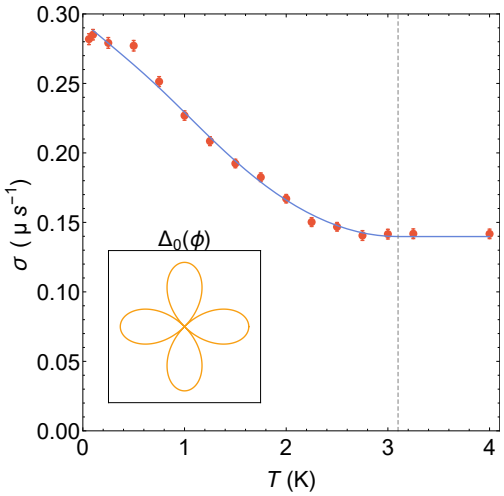

(d) Single-gap *d*-wave model.

Fig. 7.7 Results of fitting four different models for the structure of the gap to the depolarization data. The dashed line depicts the position of the bulk superconducting transition temperature, $T_c = 3.1$ K. Inset: angular dependence of the gap corresponding to the fitted parameters for each model.

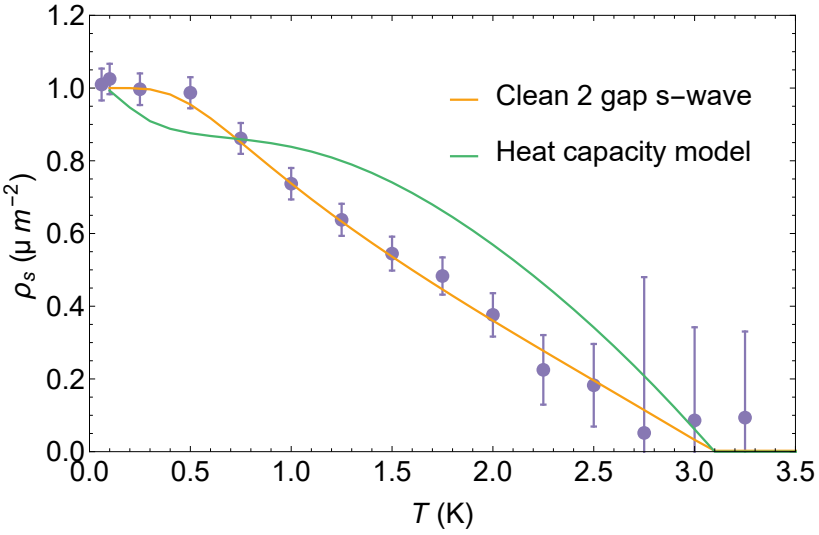

Fig. 7.8 Temperature dependence of the superfluid density, ρ_s. A model with 2 isotropic isotropic s-wave gaps has been fitted to the data. Also plotted is the 2-gap model from Ref. [97].

$\Delta_{0,1}/k_{\rm B}T_{\rm c} = 1.6(3)$ and $\Delta_{0,2}/k_{\rm B}T_{\rm c} = 0.7(1)$. To within uncertainty, the value of the larger gap is in agreement. However, the estimates for the smaller gap are not in agreement. To compare the two models directly, the superfluid density has been calculated from the depolarization rate using Eq. (5.11), after first subtracting off the nuclear dipole broadening in quadrature. The superfluid density is plotted in Fig. 7.8, with plots of the two-gap models obtained from the heat capacity measurements and the μSR results.

The zero temperature value of the penetration depth is $\lambda(0) = 728(5)$ nm. This is rather large, and is very likely an overestimation, based on the arguments made in Sec. 5.8.3. A separate estimate of $\lambda = 474$ nm has been made in Ref. [97], the implication of which will be discussed in Sec. 7.5. For now, we turn to the results of the zero-field μSR study.

7.4.2 Zero and longitudinal-field

Figure 4.10 shows the relaxation spectra collected above and below the superconducting transition temperature in zero-field. There is a large change in the relaxation behaviour on either side of the transition. The increased relaxation below $T_{\rm c}$ has been verified with the MuSR instrument in both longitudinal and transverse geometries, which requires a physical rotation of the zero-field coils by 90°. There is no hint of an oscillatory component in the spectra, which would otherwise suggest the presence of an ordered magnetic structure. The spectra collected in ZF are well described by an

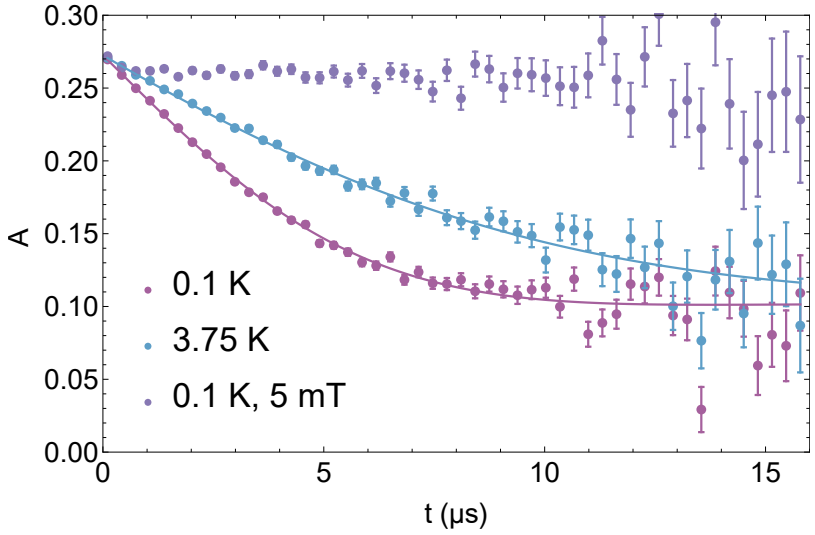

Fig. 7.9 ZF and LF-μSR spectra collected above and below T_c, with least-squares fits using the model of Eq. (4.5) (solid lines). The effect of applying a small LF field of 5 mT is also shown.

exponentially damped Gaussian Kubo-Toyabe function of the form Eq. (4.5), where σ_{ZF} measures the width of a Gaussian field distribution, assumed to originate from the nuclear dipolar field, A_0 and A_{bg} are the sample and background asymmetries, respectively, and Λ measures the electronic relaxation rate.

The sample and background asymmetries, A_0 and A_{bg}, are found to be temperature independent. Both the Gaussian depolarization rate, σ_{ZF}, and the electronic relaxation rate, Λ, exhibit a systematic increase below the superconducting transition temperature, as displayed in Fig. 7.10. However, there is no obvious correlation with the onset temperatures observed in these parameters and the superconducting transition temperature. The Gaussian relaxation rate is flat until a temperature of 1 K, at which point it sharply increases and levels off. The electronic relaxation rate is also level above a temperature of ~ 2 K, at which point it increases in value before levelling off at low temperature. The shape of this transition is reminiscent of the shape of the depolarization rate collected in the TF experiments. If the source of this signal is the superconductivity, then it would fit into the overall picture of this material, as both the superfluid density and the magnetization exhibit very broad transitions at T_c.

An exponential relaxation process is generally attributed to the field distribution arising from electronic spins, where the fluctuations occur on a fast timescale that leads to motional narrowing of the muon depolarization rate. However, a weak magnetic field of only 5 mT is enough to fully decouple the muon from this exponential

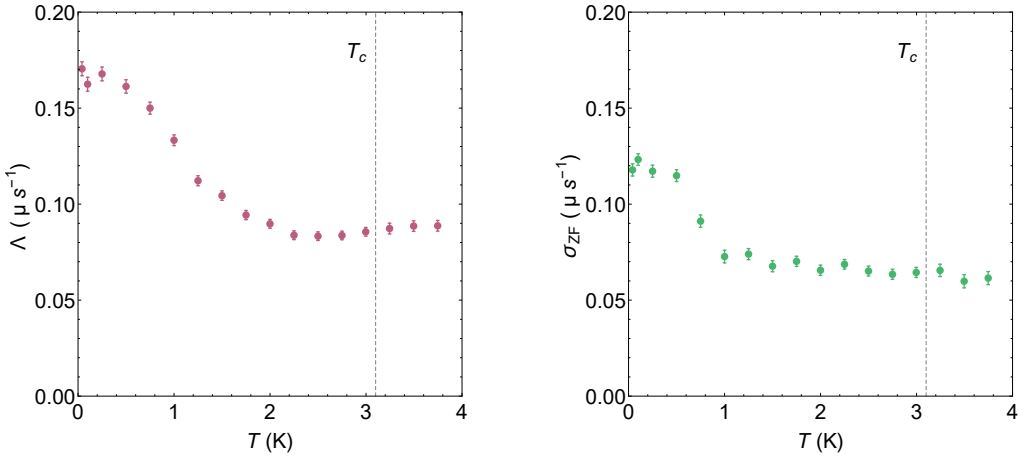

Fig. 7.10 Temperature dependence of (a) the electronic relaxation rate, Λ, and (b) the Gaussian relaxation rate, σ_{ZF}, in $Lu_3Os_4Ge_{13}$.

relaxation channel. This implies that the relaxation mechanism is actually static or quasi-static with respect to the muon lifetime. Furthermore, spin fluctuations associated with proximity to a quantum critical point would be expected to exhibit a Curie-Weiss-like temperature dependence [65]. This is not the case here, as both parameters level off at low temperatures. Some possible interpretations of these signals are discussed in the next section.

7.5 Discussion

Applying the same methodology as in Sec. 5.8.2, the microscopic properties have been calculated using reported values from Ref. [97] and the penetration depth measurement from this study. The result of using the estimate from the laboratory measurements has also been compared, with the full results presented in Tab. 7.2. The biggest change is in the interpretation of the dirty limit correction. Using the longer value of $\lambda = 728\,\mathrm{nm}$ results in $\xi_0/l_\mathrm{e} = 0.163$, which would place $Lu_3Os_4Ge_{13}$ in the clean limit. Performing the same calculations with $\lambda = 474\,\mathrm{nm}$ yields $\xi_0/l_\mathrm{e} = 4.38$, which is classified as lying in the dirty limit. However, some useful bounds are placed on the values of the quasiparticle mass, and the carrier density, in the framework of the superconductivity.

The source of the signal observed in the ZF experiment needs to be carefully considered before one can claim to have observed TRSB. The main problem is the lack of alignment with the superconducting onset temperature. Another potential

Table 7.2 Electronic properties of $Lu_3Os_4Ge_{13}$.

Property	Unit	$\lambda = 728\,\text{nm}$	$\lambda = 474\,\text{nm}$
m^*	m_e	6.61	4.90
n	$10^{27}\,\text{m}^{-3}$	1.36	3.32
ξ_0	nm	4.38	3.71
l_e	nm	1.54	0.85
ξ_0/l_e		0.163	4.38
λ_L	nm	371	204
v_F	$\text{m}\,\text{s}^{-1}$	60 000	109 000
T_F	K	785	1921

problem is that the size of the signal is very large, an order of magnitude higher than the signal see in La_7Ir_3, as well as other superconductors that have been shown to break time reversal symmetry [71, 11, 102, 12].

The TF data seem to corroborate the heat capacity observations of multiband superconductivity in this material. Band structure calculations have shown that three bands cross the Fermi surface, giving rise to a complex structure [96]. A gap could open at each of these crossing points, requiring a description of superconductivity arising from more than two bands. The recent interest in the Fe based high-T_c superconductors has prompted theoretical investigations of superconductors in which superconductivity arises from multiple bands on complex Fermi surfaces. It has been shown that in systems where there exists repulsive inter-band interactions, frustration between the bands can lead to phase transitions between TRSB and conventional BCS states below the superconducting transition temperature [103, 104]. The solutions of these equations for three superconducting bands can give rise to kinks in the gap functions of each band - see Fig. 7.11 for an example reproduced from Ref. [103]. Whether or not this could explain the experimental observations of $Lu_3Os_4Ge_{13}$ requires theoretical work, however, there are currently no experimental observations of this phenomenon. The prospect of observing this highly unusual phenomenon in this system is an exciting one.

7.6 Summary & Conclusions

The superconducting properties of the semi-metal superconductor $Lu_3Os_4Ge_{13}$ have been investigated using μSR. Strong evidence for the existence of a two-gap or anisotropic ground state has been observed. The observations in zero-field have revealed the presence of a strong signal in both the electronic and the Gaussian

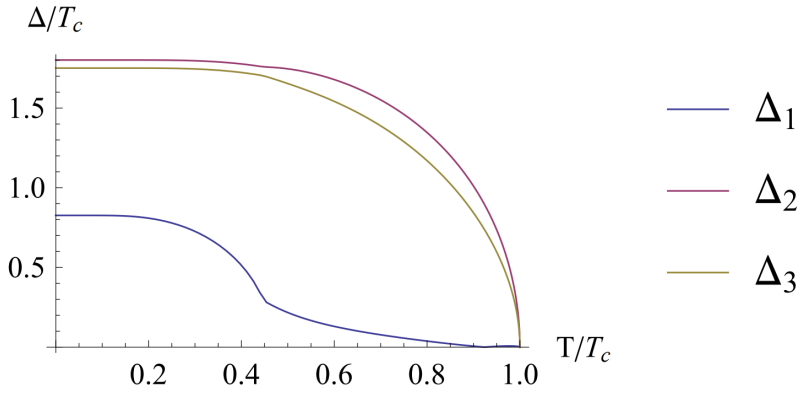

Fig. 7.11 Numerical solution to three-band BCS equations, exhibiting a kink at $T/T_c \approx 0.45$. The superconductivity breaks TRSB below this point, and is conventional above. Figure reproduced from Ref. [103].

relaxation channels, however, we hesitate to claim that this is time-reversal symmetry breaking at this point. Rather, it is necessary to investigate the multi-gap nature of this material in more depth, especially with regards to the three bands that cross the Fermi surface, in order to determine if the superconductivity is unconventional.

Chapter 8

Conclusions & further work

The field of superconductivity provides one of the richest and most diverse playgrounds for experimentalists and theoreticians alike. The discovery of the high-temperature superconductors catalysed a new era of research, characterized by the search for the unconventional superconductor, and reignited the quest for room temperature superconductivity. Such unexpected discoveries and advances have occurred throughout the history of this field, beginning with the very first unexpected observation by Onnes in 1911. Researching these materials for the sake of pure knowledge is a worthy goal, as it is only by pursuing these interests that the next ground-breaking discovery will be made.

This thesis has presented a selection of the experiments undertaken by the author over the past four years. The over arching theme is the application of muon spin spectroscopy to studies of the superconducting state, with the aim to understand how best to use this experimental tool in conjunction with laboratory based techniques. Also of interest is the application of experimental results to the calculation of microscopic properties, while ensuring that the description is as self consistent as possible. A number of new insights as well as challenges have been encountered during the analysis of these materials, as will be summarized in this final section.

8.1 Chapter summary

In Chapter 4, a study of the intermetallic compound La_7Ir_3 has been presented. This material has a noncentrosymmetric crystal structure, which means that its superconducting ground state is expected to exist as an admixture of spin-singlet and spin-triplet superconductivity. La_7Ir_3 is a type-II superconductor, which becomes superconducting at $T_c = 2.25\,\mathrm{K}$, and has an upper critical field of $0.97\,\mathrm{T}$. This

material has no strong magnetic correlations, which makes it desirable for studying spin-triplet superconductivity without these theoretical complications. Zero-field μSR measurements have observed a spontaneous magnetization appearing below T_c, the source of which is interpreted as the formation of spin-triplet Cooper pairs. This is the first observation of TRSB in this family of materials, and opens a new direction for theoretical and experimental research efforts. Transverse-field measurements of the superfluid density suggest that the superconductivity is fully gapped, and appears to be isotropic *s*-wave. Theoretical analysis of the space group of the crystal structure now needs to be performed in order to determine whether the observation of TRSB allows the existence of a spin-triplet component in the superconductivity.

One particular point of interest relates to the particular relaxation channel in which the TRSB signal is observed. For La_7Ir_3, the signal was primarily observed as an exponential decay component, with some small contributions to the Gaussian relaxation channel at low temperatures. This is not the case for all observations of TRSB. For example, $LaNiC_2$ exhibits TRSB as an exponential decay component [12], however in the Re based α-Mn superconductors the signal is seen strongly in the Gaussian relaxation channel [71]. Further theoretical work to investigate what information, if any, we can infer about the TRSB signal from these observations could prove to be an interesting project.

In Chapter 5, a full investigation of Re_3Ta, another member of the Re based superconductors with noncentrosymmetric α-Mn structure, has been carried out. Re_3Ta has previously been reported to be superconducting, however only recently has this family been subjected to intense research efforts [72, 105]. An attempt has been made to draw together all of the different experimentally observed properties, in order to build up a self-consistent picture of the microscopic properties of this system. There is no evidence for broken time-reversal symmetry in the superconducting state, and the superconductivity appears to be fully gapped with *s*-wave symmetry. Discrepancies between laboratory and μSR measurements for the absolute value of the magnetic penetration depth have led to some insights regarding some of the limitations of the μSR technique in high-κ superconductors.

Re_3Ta has provided some unexpected parallels to the physics of the high-temperature superconductors, by way of its potentially interesting vortex dynamics in the vicinity of T_c. Magnetization measurements have shown that the vortex lattice becomes de-pinned at a field much lower than the upper critical field. Effectively, there exists a large region of the phase diagram where pinning is weak, and vortices are free to move. Also, μSR measurements have shown that the internal field distribution is narrowed as the temperature approaches T_c, where the motional narrowing

is assumed to come from vortex motion. This behaviour is unusual for such a low T_c material, as typically thermal fluctuations are not energetic enough to de-pin vortices at such low temperatures. The calculated Ginzburg number and Quantum resistance of this material lie in the intermediate range between typical values for high-T_c superconductors and conventional low-T_c materials.

The ternary borides $LuRuB_2$ and $YRuB_2$ were investigated in Chapter 6. These materials exhibit superconductivity with relatively high critical temperatures of 9.8 K and 7.8 K, respectively, and have large upper critical fields of 5.7 T and 4.8 T. They are important reference materials, as the $4f$ band is completely filled in the Lu compound, and empty in the Y material. The TF measurements of the superfluid density reveal that both of these materials lie in the weak coupling limit, which is interesting given their high transition temperatures. Zero-field measurements have also revealed the presence of spin fluctuations coexisting with the superconducting state, in both of these materials. These fluctuations are very weak, as they are decoupled with a small longitudinal magnetic field; however, they exhibit a critical slowing down behaviour as the temperature is lowered. This suggests that both of these materials may lie in the vicinity of a quantum critical point. Further research could clarify whether this is the case, for example by investigating the effect of doping on the superconductivity in these materials.

Finally, the semi-metal $Lu_3Os_4Ge_{13}$ has been investigated using μSR in Chapter 7. This low temperature superconductor exhibits a number of unusual features. Its upper critical field is almost as large as the Pauli limiting field, and may be larger if the assumptions of the WHH theory do not hold for this material. This could be the case in a material with multiple superconducting gaps, as WHH theory is a single gap model for the upper critical field. The heat capacity of this compound is well described by an $s+s$-wave, double-gap model, and the field dependence of the Sommerfeld constant, γ, is not linear. Because γ is directly related to the carrier density, this can indicate that the superconducting gap is anisotropic, and possibly contains nodes. The μSR investigation of the superfluid density appears to corroborate this story, as both two-gap and anisotropic s-wave models adequately describe the data. In ZF, a signal was observed in both the exponential and Gaussian relaxation channels, with onset temperature of ~ 2 K and 1 K, respectively. As these do not coincide with the bulk measurement of T_c, we can not immediately ascribe this to being an observation of broken time-reversal symmetry. However, it does provide clues as for how to proceed with the theoretical analysis of this material. Band structure calculations have shown that the Fermi surface is cut by three different bands, leading to a complicated structure. It seems reasonable to

envision superconducting gaps forming at these crossing points, in which case we could have a system with three superconducting gaps. The existence of a repulsive interaction between two of these bands could lead to a novel frustrated state, in which the system can transition to a phase with broken time-reversal symmetry below T_c. Such an experimental observation has never been confirmed, however it has been predicted in multiband superconductors [103].

8.2 Universal correlations: the Uemura plot

The Uemura plot provides a method of classifying superconductors, and is based on an observed correlation between the superconducting transition temperature, T_c, and the Fermi temperature, T_F, in unconventional superconductors [106]. As μSR provides a sensitive method of measuring the magnetic penetration depth directly, this can be coupled with laboratory measurements of heat capacity in order to calculate the electronic properties of the superconductor. This methodology has been utilized in the analysis of the materials studied in this thesis in order to calculate the Fermi temperature for each one. The complete Uemura plot, encompassing the materials studied in this work is thus presented in Fig. 8.1.

It has been found that the high-temperature cuprate, chevrel phase, fullerene, organic, and heavy fermion superconductors all exhibit an approximately linear correlation between T_c and T_F. The region in which $0.01 \leq T_c/T_F \leq 0.1$ has been loosely defined the 'band of unconventionality' on the Uemura plot, as superconductors with unconventional pairing mechanisms tend to be situated within this region. This classification scheme also allows one to visualize how close a particular system is from a Bose-Einstein condensate, in which the Cooper pairs are true bosons. Conversely, it also allows one to classify superconductors in terms of their proximity to the conventional, BCS, weakly-coupled conventional superconductors, which are found in the lower right-hand quadrant of the Uemura plot.

All of the superconductors studied are found to lie just outside of the band of unconventionality. In the case of $Lu_3Os_4Ge_{13}$, a line has been added to the figure to represent the uncertainty in the value of T_F (see Sec. 7.5). They do, however, lie far away from the elemental, conventional superconductors. Interestingly, there is an approximately linear trend between the materials studied, i.e. the materials studied all have a similar value of T_c/T_F. This may hint at some underlying connection between the physics of these different materials. However, stronger conclusions will require further work - for now it is merely an interesting relationship to remark upon.

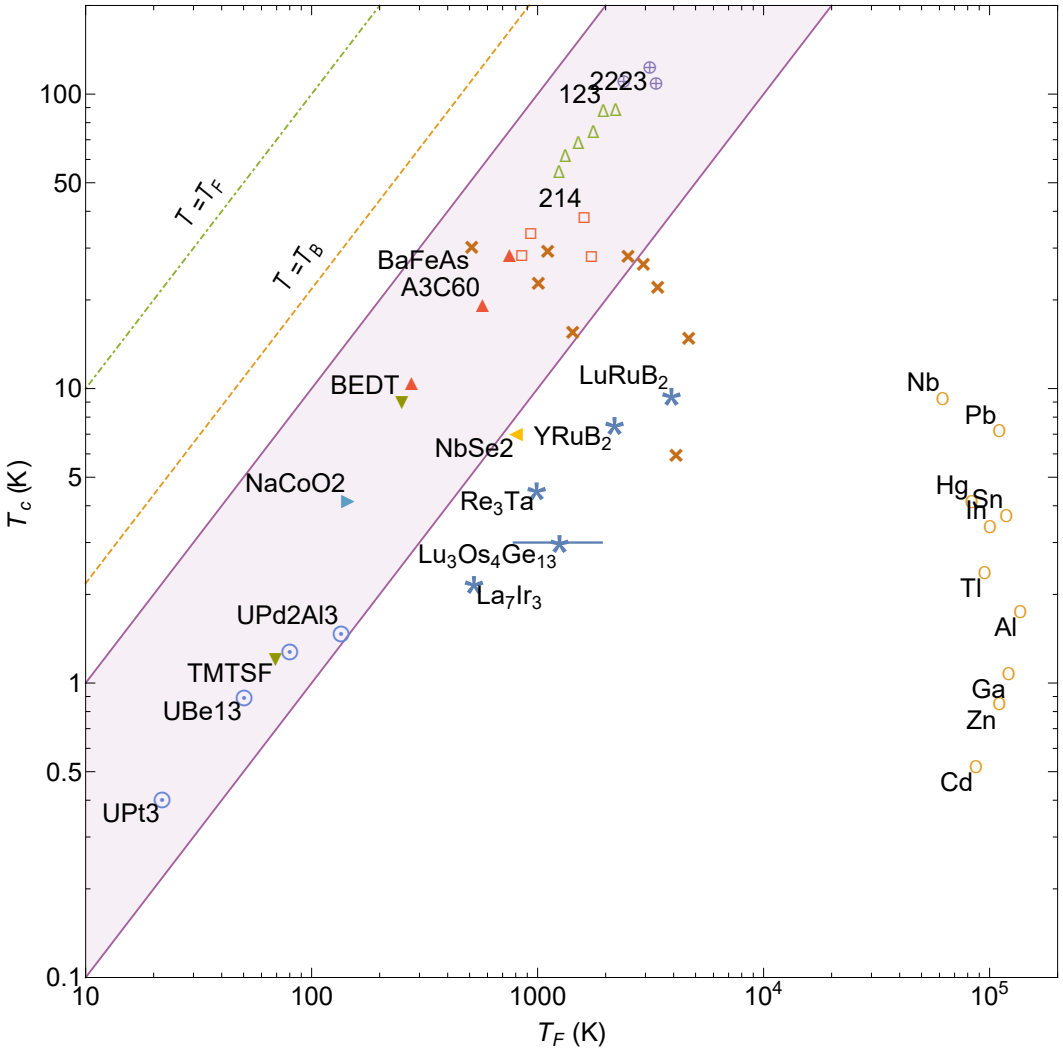

Fig. 8.1 Uemura plot, in which the Fermi temperature forms the x-axis and superconducting transition temperature is the y-axis. Superconductors are then classified according to their position on the diagram. The materials studied in this thesis are the blue stars ($\star$) near the centre of the figure. The elemental superconductors are marked with yellow open circles ($\circ$), and are grouped on the right hand edge of the figure. Finally, a few examples of some important unconventional superconducting systems are presented: the high-temperature cuprates ($\triangle$, $\square$, $\otimes$); organic superconductors ($\blacktriangledown$); fullerenes ($\blacktriangle$); iron-based superconductors ($\times$); heavy fermion superconductors ($\odot$); as well as $NbSe_2$ ($\blacktriangleleft$) and $NaCoO_2$ ($\blacktriangleright$). The shaded region is the 'band of unconventionality' as discussed in the text. Also plotted are the straight lines where the transition temperature is equal to the Fermi temperature and the Bose temperature T_B.

8.3 Conclusion

In conclusion, this thesis has contributed to the overall understanding of superconductivity, by describing the superconducting behaviour of several unusual members of the vast phase space from which there are many compounds to investigate. μSR has proven to be an invaluable experimental technique that allows insights beyond traditional laboratory methods. It is only through persevering with as many of these studies as possible that any headway can be made towards the ultimate goal of a full understanding of this most unusual quirk of nature.

References

[1] M. R. Norman. *arxiv:1302.3176* (2013).

[2] J. Bardeen, L. N. Cooper, and J. R. Schrieffer. *Phys. Rev.*, **108**, 1175 (1957).

[3] M. R. Norman. *Science*, **332** (6026), 196–200 (2011).

[4] P. W. Anderson. *Journal of Physics: Conference Series*, **449** (1), 012001 (2013).

[5] M. Amores *et al. J. Mater. Chem. A*, **4**, 1729–1736 (2016).

[6] M. Gomilšek *et al. Phys. Rev. B*, **93**, 060405 (2016).

[7] A. A. Aczel *et al. Phys. Rev. B*, **93**, 214407 (2016).

[8] A. Hillier, D. Paul, and K. Ishida. *Microchemical Journal*, **125**, 203 – 207 (2016).

[9] S. J. Ray *et al. Phys. Rev. B*, **89**, 094504 (2014).

[10] G. M. Luke *et al. Nature*, **394**, 558 (1998).

[11] Y. Aoki *et al. Phys. Rev. Lett.*, **91**, 067003 (2003).

[12] A. D. Hillier, J. Quintanilla, and R. Cywinski. *Phys. Rev. Lett.*, **102**, 117007 (2009).

[13] J. F. Annett. *Superconductivity, Superfluids, And Condensates*, (Oxford University Press2004).

[14] M. Tinkham. *Introduction to Superconductivity: Second Edition (Dover Books on Physics) (Vol i)*, (Dover Publications2004), second edition edition.

[15] M. Cyrot and D. Pavuna. *Introduction to Superconductivity and High Tc Materials*, (World Scientific, Singapore1992).

[16] J. File and R. G. Mills. *Phys. Rev. Lett.*, **10**, 93–96 (1963).

[17] W. Meissner and R. Ochsenfeld. *Naturwissenschaften*, **21**, 787–788 (1933).

[18] F. London and H. London. *Proceedings of the Royal Society of London Series A*, **149**, 71–88 (1935).

[19] V. L. Ginzburg and L. D. Landau. *Zh. Eksp. Teor. Fiz.*, **20**, 1064 (1950).

[20] M. Cyrot. *Reports on Progress in Physics*, **36** (2), 103 (1973).

[21] L. P. Gor'kov. *Soviet Physics JETP*, **9** (6), 1364 (1959).

[22] A. A. Abrikosov. *Soviet Physics JETP*, **5** (6), 1174–1182 (1957).

[23] R. Khasanov *et al. Phys. Rev. B*, **78**, 220510 (2008).

[24] E. H. Brandt. *Physica B*, **404**, 695–699 (2009).

[25] L. N. Cooper. *Phys. Rev.*, **104**, 1189–1190 (1956).

[26] V. P. Mineev and M. Sigrist. *Basic Theory of Superconductivity in Metals Without Inversion Center*, chapter 4, pages 129–154, (Springer, Berlin, Heidelberg2012).

[27] P. W. Anderson. *J. Phys. Chem. Solids*, **11** (26) (1959).

[28] P. W. Anderson. *Phys. Rev. B*, **30**, 4000 (1984).

[29] L. P. Gorkov and E. I. Rashba. *Phys. Rev. Lett.*, **87**, 037004 (2001).

[30] P. A. Frigeri *et al. Phys. Rev. Lett.*, **92**, 097001 (2004).

[31] W. L. McMillan. *Phys. Rev.*, **167**, 331–344 (1968).

[32] D. C. Johnston. *Superconductor Science and Technology*, **26** (11), 115011 (2013).

[33] V. K. Anand *et al. Journal of Physics: Condensed Matter*, **26** (40), 405702 (2014).

[34] C. Kittel. *Introduction to Solid State Physics*, (John Wiley & Sons, Inc., New York1986), 6th edition.

[35] M. Sigrist. *AIP Conference Proceedings*, **789** (1), 165–243 (2005).

[36] F. Bouquet *et al. EPL (Europhysics Letters)*, **56** (6), 856 (2001).

[37] R. Prozorov and R. W. Giannetta. *Superconductor Science and Technology*, **19** (8), R41 (2006).

[38] F. J. Blatt. *Physics of Electronic Conduction in Solids*, (McGraw-Hill, New York1968).

[39] M. McElfresh. *Quantum Design* (1994).

[40] J. Lashley *et al. Cryogenics*, **43** (6), 369 – 378 (2003).

[41] R. E. Schwall, R. E. Howard, and G. R. Stewart. *Review of Scientific Instruments*, **46** (8), 1054–1059 (1975).

[42] B. H. Toby. *Powder Diffraction*, **21** (1), 67–70 (2006).

[43] G. H. Eaton, C. A. Scott, and W. G. Williams. *Hyperfine Interactions*, **87** (1), 1099–1104 (1994).

[44] S. Giblin *et al. Nuclear Instruments and Methods in Physics Research Section A: Accelerators, Spectrometers, Detectors and Associated Equipment*, **751**, 70 – 78 (2014).

[45] P. King *et al. Physica B*, **326** (1–4), 260 – 264 (2003).

[46] G. Eaton *et al. Nuclear Instruments and Methods in Physics Research Section A: Accelerators, Spectrometers, Detectors and Associated Equipment*, **342** (2), 319 – 331 (1994).

[47] B. D. Rainford. *Aspects of data treatment for transverse μSR*, chapter 16, pages 463–471, (IOP Publishing1999).

[48] Y. J. Uemura. *Muon Science: Muons in Physics, Chemistry, and Materials*, chapter 4, pages 85–114, (IOP Publishing1999).

[49] R. S. Hayano *et al. Phys. Rev. B*, **20**, 850 (1979).

[50] V. K. Anand *et al. Phys. Rev. B*, **83**, 064522 (2011).

[51] T. Takimoto and P. Thalmeier. *J. Phys. Soc. Jpn*, **78**, 103703 (2009).

[52] E. Bauer and M. Sigrist (editors). *Non-centrosymmetric superconductors*, (Springer-Verlag, Berlin Heidelberg2012).

[53] R. D. Blaugher and J. K. Hulm. *J. Phys. Chem. Solids* (1961).

[54] E. Bauer *et al. Phys. Rev. Lett.* (2004).

[55] N. Kimura *et al. Phys. Rev. Lett.* (2005).

[56] I. Sugitani *et al. J. Phys. Soc. Jpn.*, **75** (4), 043703 (2006).

[57] R. Settai *et al. Journal of Magnetism and Magnetic Materials*, **310** (2, Part 1), 844 – 846 (2007). Proceedings of the 17th International Conference on Magnetism The International Conference on Magnetism.

[58] R. P. Singh *et al. Phys. Rev. B*, **90**, 104504 (2014).

[59] M. Smidman *et al. Phys. Rev. B*, **89**, 094509 (2014).

[60] T. H. Geballe *et al. Phys. Rev.*, **137**, A119–A127 (1965).

[61] T. Smith and H. Luo. *Journal of Physics and Chemistry of Solids*, **28** (4), 569 – 576 (1967).

[62] P. Pedrazzini *et al. Physica C: Superconductivity*, **336** (1–2), 10–18 (2000).

[63] A. A. Coelho. *TOPAS-Academic, Version 6*. Bruker-AXS (2016).

[64] L. B. Mendelsohn, F. Biggs, and J. B. Mann. *Phys. Rev. A*, **2**, 1130–1134 (1970).

[65] R. S. Hayano *et al. J. Phys. Soc. Jpn.*, **49** (5), 1773–1783 (1980).

[66] C. H. Choi and P. Muzikar. *Phys. Rev. B*, **39**, 9664–9666 (1989).

[67] N. R. Werthamer, E. Helfand, and P. C. Hohenberg. *Phys. Rev.*, **147** (1), 295–302 (1966).

[68] Y. J. Uemura *et al. Phys. Rev. B*, **38**, 909–912 (1988).

[69] Y. J. Uemura *et al. Phys. Rev. Lett.*, **62**, 2317–2320 (1989).

[70] Y. J. Uemura *et al. Phys. Rev. Lett.*, **66**, 2665–2668 (1991).

[71] R. P. Singh *et al. Phys. Rev. Lett.*, **112**, 107002 (2014).

[72] P. K. Biswas *et al. Phys. Rev. B*, **85**, 134505 (2012).

[73] E. Bucher, F. Heiniger, and J. Müller. *Helv Phys Acta*, **34**, 843–858 (1961).

[74] J. Brophy, P. Schwarzkopf, and J. Wulff. *Trans. Met. Soc. AIME*, **218** (1960).

[75] P. K. Biswas *et al. Phys. Rev. B*, **84**, 184529 (2011).

[76] C. Caroli, P. D. Gennes, and J. Matricon. *Physics Letters*, **9** (4), 307 – 309 (1964).

[77] G. E. Volovik. *Soviet Journal of Experimental and Theoretical Physics Letters*, **58**, 469 (1993).

[78] L. Xie, T. Su, and X. Li. *Physica C: Superconductivity*, **480**, 14 – 18 (2012).

[79] S. Lee. *Muon Science: Muons in Physics, Chemistry, and Materials*, chapter 7, pages 149–164, (IOP Publishing1999).

[80] S. L. Lee *et al. Phys. Rev. Lett.*, **75**, 922–925 (1995).

[81] E. H. Brandt. *Active and passive electronic components*, **15** (3-4), 193–210 (1993).

[82] G. Blatter *et al. Rev. Mod. Phys.*, **66**, 1125–1388 (1994).

[83] B. T. Matthias *et al. Proc. Natl. Acad. Sci. USA*, **74** (4), 1334 (1977).

[84] D. C. Johnston. *Solid State Commun.*, **24**, 699–702 (1977).

[85] K. Yvon and D. C. Johnston. *Acta Crystallog. Sect. B.*, **38** (1), 247–250 (1982).

[86] D. Johnston and H. Braun. In B. Maple and O. Fischer (editors), *Superconductivity in Ternary Compounds II*, volume 34 of *Topics in Current Physics*, pages 11–55, (Springer US1982).

[87] R. Shelton *et al. Mater. Res. Bull.*, **15** (10), 1445 – 1452 (1980).

[88] H. Ku and R. Shelton. *Mater. Res. Bull.*, **15** (10), 1441 – 1444 (1980).

[89] W. Lee, S. Appl, and R. Shelton. *J. Low Temp. Phys.*, **68** (1-2), 147–157 (1987).

[90] Y. Kishimoto *et al. J. Phys. Conf. Ser.*, **176** (1), 012039 (2009).

[91] S. R. Dunsiger *et al. Phys. Rev. B*, **54**, 9019–9022 (1996).

[92] B. D. Rainford. *Muon Science: Muons in Physics, Chemistry, and Materials*, chapter 5, pages 115–136, (IOP Publishing1999).

[93] A. Maisuradze *et al. Phys. Rev. B*, **82**, 024524 (2010).

[94] P. Caldirola. *Il Nuovo Cimento (1955-1965)*, **3** (2), 297–343 (1956).

[95] A. Hillier and R. Cywinski. *Applied Magnetic Resonance*, **13** (1-2), 95–109 (1997).

[96] O. Prakash, A. Thamizhavel, and S. Ramakrishnan. *Journal of Physics: Conference Series*, **592** (1), 012065 (2015).

[97] O. Prakash, A. Thamizhavel, and S. Ramakrishnan. *Superconductor Science and Technology*, **28** (11), 115012 (2015).

[98] O. Prakash, A. Thamizhavel, and S. Ramakrishnan. *Journal of Physics: Conference Series*, **568** (2), 022039 (2014).

[99] T. M. Riseman and J. H. Brewer. *Hyperfine Interactions*, **65** (1), 1107–1111 (1991).

[100] R. Khasanov *et al. Phys. Rev. Lett.*, **98**, 057007 (2007).

[101] A. Carrington and F. Manzano. *Physica C - Superconductivity*, **385** (1–2), 205–214 (2003).

[102] A. Bhattacharyya *et al. Phys. Rev. B*, **91**, 060503 (2015).

[103] B. J. Wilson and M. P. Das. *Journal of Physics: Condensed Matter*, **25** (42), 425702 (2013).

[104] B. J. Wilson and M. P. Das. *Journal of Physics: Condensed Matter*, **26** (32), 325701 (2014).

[105] D. Singh *et al. Phys. Rev. B*, **94**, 054515 (2016).

[106] Y. J. Uemura and R. Cywinski. *Muon Science: Muons in Physics, Chemistry, and Materials*, chapter 8, pages 165–172, (IOP Publishing1999).